Production of 3D Nanostructures via Advanced Surface Chemistry and Nanolithography

By

AUDREY RACHEL SULKANEN
DISSERTATION

Submitted in partial satisfaction of the requirements for the degree of

DOCTOR OF PHILOSOPHY

in

Chemistry

in the

OFFICE OF GRADUATE STUDIES

of the

UNIVERSITY OF CALIFORNIA

DAVIS

Approved:

Prof. Gang-yu Liu, Chair

Prof. Gang Sun

Prof. Xi Chen

Committee in Charge

2021

Acknowledgement

I would like to thank professor Gang-yu Liu for her feedback, support, and encouragement throughout my Ph.D. studies. She has spent countless hours helping me to become both a better scientist and a better scientific communicator, and without her help, I would not be where I am today.

I am also grateful to the current and former Liu group members for all of their support and knowledge:

Dr. Victoria Tran, Dr. Logan A Swartz, Dr. Jiali Zhang, Dr. Jianli Zhao, Dr. Cody Chalker, Dr. Shuo Wang, Dr. Arpad Karsai, Dr. Marshall van Zijll, Dr. Joao Francisco Ventrici de Souza, Dr. Weifeng Lin, Evgeny Ogorodnik, Bradley Harris, Yunbo Zheng, Yuqi Huang, Terell Keel, and Matt Owen.

Sincerest thanks to my thesis committee: Professor Gang Sun and Professor Xi Chen.

Additional thanks to my collaborators: Dr J Nathan Hohman, Dr. Jaeuk Sung, Professor Nancy Sottos, Professor Jeff Moore, Andrey Krayev, Yiwen Zhu, and Hai Qian.

Special thanks to Ms. Susan Stagner for her help.

Thank you to all of the chemistry staff who helped me throughout my graduate career: Brad Wolf, Laura Troutner, DeAnn Ronning, Emily Atkinson, Scott Berg, Rose Smith, Will Angel, Patricia Chuda, Perry Gee, Eric Rosario, Debbie Decker, Minh Hoang, Jessica Potts and Karen Gagnon.

I would also like to thank my parents, Theresa Couture and Steven Sulkanen, for their endless support, love, and encouragement throughout my educational pursuits. Thank you to Theresa Camden as well, who is like a second mother to me, for her endless love and patience.

Thank you to my partner, Chris Shelton. I feel so lucky to have you by my side throughout this long and sometimes difficult journey. I cannot wait to see what the future holds for us.

And finally, thank you to all the friends and amazing people I met in graduate school.

Abstract

The focus of my thesis is the development of an advanced methodology to create 3D nanostructures by design, and to demonstrate the control over geometry and chemical functionalities of the nanostructures produced. The driving motive behind this are the pressing need for 3D nanostructures in biomaterials development, modern nanodevices and biomedical applications. My approach is scanning probe microscopy-based nanolithography in combination with advanced surface chemistry. This thesis clearly demonstrated the concept and feasibility of the approach. While the power of 3D printing has proven to be a powerful tool in additive manufacture, extending the spatial precision to nanometer scale would lay the foundation for the next science and technology revolutions. Specific applications impacted by this work include surface science, catalysis, modern sensors, nanophotonics, and nanoelectronics.

Three significant goalposts are reported in this thesis followed by future prospective research. First focuses on mechanically sensitive molecules known as mechanophores, which have recently attracted much interest due to the need for mechanoresponsive materials. Maleimide−anthracene mechanophores located at the interface between poly- (glycidyl methacrylate) (PGMA) polymer brushes and Si wafer surfaces were activated locally using atomic force microscopy (AFM) probes to deliver mechanical stimulation. Each individual maleimide−anthracene mechanophore exhibits binary behavior: undergoing a retro-[4 + 2] cycloaddition reaction under high load to form a surface-bound anthracene moiety and free PGMA or remaining unchanged if the load falls below the activation threshold. In the context of nanolithography, this behavior allows the high spatial selectivity required for the design and production of complex and hierarchical patterns with nanometer precision. The high spatial

precision and control reported in this work brings us closer to molecular level programming of surface chemistry, with promising applications such as 3D nanoprinting, production of coatings, and composite materials that require nanopatterning or texture control as well as nanodevices and sensors for measuring mechanical stress and damage in situ.

Following our success with creating structures by design using nanolithography and mechanophore chemistry, we set out to fabricate organizational chirality on surfaces, which has been an interest in chemistry and materials science due to the need for enantioselective catalysis, separation, and reactions. Current methods for production of organizational chirality are primarily based upon self-assembly of molecules. While powerful, the chiral structures produced are restricted to those dictated by reaction thermodynamics. This work introduces a method to create organizational chirality by design. Using atomic force microscopy in conjunction with our chosen surface chemistry, various chiral structures were designed and produced with nanometer precision, from simple chiral spirals to arrays of chiral nanofeatures to hierarchical chiral structures. The size, geometry, and organizational chirality faithfully follow the designs with a high degree of spatial control. The concept and methodology reported here provides researchers a new means to carry out organizational chiral chemistry, with the intrinsic advantages of chiral structures by design. The results open new and promising applications including organizational chiral sensors, 3D nanoprinting of chiral structures, enantiomeric separation, and enantiomeric heterogeneous catalysis.

Building upon the theme of controlled fabrication of nanostructures, we utilized controlled assembly to create structures by design. Our prior work has demonstrated the concept of controlled assembly of macromolecules such as star polymers [molecular weight (Mw) ~383 kDa,

hydrodynamic radius R ~ 13.8 nm] in droplets. This work extends this concept to smaller molecules, in this case, poly(ethylene glycol) bis-tetrazine (PEGbisTz, Mw 8.1 kDa, R ~1.5 nm). The key to controlled molecular assembly is to first deliver ultrasmall volumes (sub-fL) of solution containing PEG-bisTz to a substrate. The solvent evaporates rapidly due to the minute volume, thus forcing the assembly of solute, whose overall size and dimension are dictated by the initial liquid geometry and size. Using prepatterned surfaces, this work revealed that the initial liquid shape can be further tuned, and we could control the final assembly of solute such as PEGbisTz molecules. The degree of control was demonstrated by varying the micropatterns and delivery conditions. This work demonstrated the validity of controlled assembly for PEG-bisTz and enables three-dimensional (3D) nanoprinting of functional materials. The technology has promising applications in nanophotonics, nanoelectronics, nanocomposite materials, and tissue engineering.

These investigations into fabrication of a variety of nanostructures demonstrated the success in creating, complex, hierarchical, and chiral structures with nanometer precision. This success lays the foundation for utilization of scanning probe lithography to create functional nanostructures out of new and exciting materials. Future investigations of this technology will focus on incorporating materials such as mithrene, a unique 3D material that possesses 2D properties, and anthraquinone modified cellulose nanocrystals. Combined with the methodology presented here, the development of these structures will be useful in future applications such as modern sensors, nanodevices, nanophotonics, and nanoelectronics.

TABLES OF CONTENTS

ACKNOWLEDGEMENT ..... **II**

ABSTRACT ..... **IV**

TABLES OF CONTENTS ..... **VII**

LIST OF FIGURES ..... **XII**

LIST OF TABLES ..... **XVIII**

CHAPTER 1 ..... **1**

Introduction **1**

1.1 Three Dimensional Nanoprinting via Scanning Probe Microscopy Based Nanolithography. **1**

1.2 Thesis Objective. **2**

1.2.1 Nanofabrication Via Localized Mechanophore Activation. **2**

1.2.2 Nanofabrication of Chirality by Design Using AFM. **3**

1.2.3 Combined Scanning and Probe Microfluidic Delivery for the Creation of Custom Nanostructures. **4**

1.3 Structure of the thesis **5**

1.4 References. **6**

CHAPTER 2 ..... **10**

Experimental **10**

2.1 Atomic Force Microscopy **10**

2.1 Microfluidic Delivery **12**

2.3 References **14**

CHAPTER 3 ..... **17**

Spatially Selective and Density-Controlled Activation of Interfacial Mechanophores **17**

3.1 Introduction. **17**

3.2 Experimental **19**

3.2.1 Materials **19**

3.2.2 Active Fabrication Process. **19**

3.2.3 Surface Functionalization of Silicon Substrate with MA Mechanophore. **20**

3.2.4 Surface Patterning MA Mechanophore Functionalized Silicon Substrate. **21**

3.2.5 Polymer Brush Formation on MA Functionalized Substrate. **21**

3.2.6 Control Specimen Fabrications. **23**

3.2.7 Preparation of Silicon Wafers for Calibration. **24**

3.2.8 AFM Imaging **24**

3.2.9 AFM Activation. **25**

3.2.10 AFM Custom Design **25**

3.2.11 Fluorescence Measurement **26**

3.2.12 ToF-SIMS Imaging **26**

3.3 Results and Discussion **27**

3.3.1 Spatially-selective Activation of Interfacial Mechanophore. **27**

3.3.2 Control Over the Density of Mechanophore Activation. **31**

3.3.3 Production of Complex Patterns by Design **34**

3.3.4 Confirmation of Mechanochemical Activation Using Fluorescence Microscopy, ToF-SIMS, Optical Microscopy, and AFM Topographic Imaging **39**

3.3.5 Attempted Activation of Control Samples **40**

3.3.6 Production of Hierarchical Patterns 41

CHAPTER 4 51

PRODUCING ORGANIZATIONAL CHIRALITY BY DESIGN VIA SCANNING PROBE NANOLITHOGRAPHY 51

4.1 Introduction 51

4.2 Experimental 52

4.2.1 Materials. 52

4.2.2 Preparation of Self-Assembled Monolayers on Surfaces. 52

4.2.3 High-Resolution AFM Imaging and Nanolithography. 53

4.3 Results and Discussion 54

4.3.1 Production of Organizational Chiral Structures by Design Using Nanolithography and Self-assembled Surface Chemistry. 54

4.3.2 Production of Organizational Chiral Structures by Design Using Nanolithography and Mechanochemistry 58

4.3.3 Production of Hierarchical Chiral Features by Design. 63

4.4 Conclusions 67

4.5 References 68

CHAPTER 5 73

Controlled Molecular Assembly of Tetrazine Derivatives on Surfaces 73

5.1 Introduction 73

5.2 Experimental Methods 75

5.2.1 Materials. 75

5.2.2 Synthesis of PEG-*bis*Tz and C12-*bis*TCO 75

5.2.3 Preparation of Surfaces as Support for Material Delivery. 75

5.2.4 Contact Angle Measurement. 76

5.2.5 Integrated Atomic Force Microscopy and Microfluidic Device. 77

5.2.6 AFM Imaging. 77

5. 3 Results and Discussion 78

5.3.1 Controlled Assembly of PEG-bisTz in Individual Ultrasmall Droplets. 78

5.3.2 Controlled Assembly of PEG-*bis*Tz During Continuous Delivery of Solution Along Lines. 82

5.3.3 The Impact of Surface Patterning on The Assembly of PEG-bisTz. 85

5.4 Conclusions 92

5.5 References 93

CHAPTER 6 99

Conclusions, on-Going Work and Future Perspectives 99

6.1 Conclusions 99

6.2 On-Going Work and Future Perspectives 101

6.2.1 Atomic Force Microscopy and Tip Enhanced Raman Spectroscopy Investigation of Mithrene 101

6.2.2 High Resolution Imaging of Mithrene. 102

6.2.3 High Force Shearing of Mithrene via AFM. 103

6.2.4 TERS and Far Field Raman Spectroscopy of Mithrene 105

6.2.5 Conclusions & Future Work 109

6.2.6 Functionalization of Cellulose Nanocrystals with Anthraquinone 110

6.2.7 AFM Characterization of Sulfated, Desulfated and AQ Functionalized CNCs

.....111

6.2.8 Conclusions & Future Work for AQ-CNCs.....114

6.2.9 References.....114

LIST OF FIGURES

Figure 2.1 Schematic diagram of a deflection type AFM.

Figure 2.2 Schematic diagram of the Key parts of the microfluidic AFM (FluidFM)

Figure 3.1. Fabrication steps for patterned PGMA brush-MA mechanophore grafted active specimen on silicon substrate.

Figure 3.2. Representative size exclusion chromatography results of the synthesized PGMA for the 10- and 20-min polymerization times.

Figure 3.3. Fabrication steps for patterned PGMA brush grafted control specimen on silicon substrate.

Figure 3.4. A schematic diagram illustrating activation of MA mechanophores at the interface between a polymer brush and silicon surface using an AFM probe. Each mechanophore activation produces a free maleimide and a surface-bound anthracene group via a retro [4+2] cycloaddition reaction.

Figure 3.5. (A) A 24 x 24 μm AFM topographic image of a PGMA brush acquired in DMSO under 10 nN force. **(B)** The same area as (**A)** after the central 5.46 μm x 4.80 μm region was subjected to high force (450 nN) scans at 12.52 μm/s with 256 lines. **(C)** Schematic diagram illustrates the surface functionalities across the middle of image (**B)**. **(D)** Fluorescence microscopy image of the same region as (**B)** collected from 410 to 430 nm. All scale bars are 5.0 μm.

Figure 3.6. (A) Top: AFM topographic images of a PGMA brush on a Si-wafer, taken at 5 designated locations. The images were acquired in DMSO under an imaging force of 55 nN. Each

image covers a 15.4 μm x 15.4 μm area with the central 5.8 μm x 4.8 μm area scanned under a high load indicated above each image. Bottom: fluorescence microscopy images acquired at the same areas as those above. Lateral scale bars are 5.0 μm. **(B)** The right plot shows the fluorescence intensities, normalized with respect to the 600 nN square's fluorescence (blue, normalized PL), and relative height difference (black) as a function of load.

Figure 3.7. (A) The designed gradient image file shown in grey scale. **(B)** A 7.0 μm x 6.6 μm AFM topographic image of a PGMA brush overlaid with the physical location and dimension of **A** prior to activation. AFM lithography was executed, applying the corresponding forces following the designed gradient pattern. (**C**) AFM topographic image of the same area as **B** post lithography. The polymer brush height was 10.6 ± 0.6 nm above the Si wafer surface, passivated by 1.4±0.2 nm thick oligomeric ethylene oxide. Lateral scale bar and vertical range are 2.0 μm, and 0-14 nm, respectively. **(D)** Height profile as indicated by the horizontal line in **C**.

Figure 3.8. (**A**) AFM topographic image taken after scanning a complex grey scale image (inset) onto 12.1 ± 1.3 nm thick PGMA brush immobilized by MA mechanophores on a Si-wafer, passivated by 1.4±0.2 nm thick oligomeric ethylene oxide. (**B**) Fluorescence microscopy image of the same region as A, under 360 nm excitation and collected from 410-430 nm. All scale bars are 1.0 μm.

Figure 3.9. A complex, multishade mechanophore feature of UC Davis Aggie logo. (inset) A greyscale force bitmap of the UC Davis Aggie logo.[51] The force applied ranged from 8.8 nN to 1.3 μN for black to white respectively, and other important lithography parameters are included. (A) AFM topographic image of the Aggie logo multishade features. (B) Corresponding fluorescence microscopy image of the same region as A, under 360 nm excitation and collected from 410-430

nm. All scale bars are 2.0 μm.

Figure 3.10. Confirmation of interfacial mechanophore activation using AFM lithography. (A) Fluorescence image of an 'T' feature fabricated. (B)ToF-SIMS image for fragment 41.99 u (CNO^-) which corresponds to the maleimide moiety of the fabricated 'T' feature. (C) Optical image of fabricated the 'T' feature. (D) AFM topographic image of fabricated 'T' feature. The scale bars are 20 μm.

Figure 3.11. Images (A) and (B) were acquired under identical conditions as Figures 3.5A and 3.5B, respectively, except that the surface adsorbates were polymer brushes without mechanophores. (C) Schematic diagram illustrates the surface functionalities corresponding to the AFM image B. (D) Fluorescence image of the same region as B. All scale bars are 5.0 μm.

Figure 3.12. Example of hierarchical feature produced using AFM. The lateral AFM image of the hierarchical feature is shown. (Inset) An 'T' feature patterned with a square grid, custom designed. The scale bar is 1.0 μm.

Figure 4.1. (A) The design of a pair of S and R spirals. (B) AFM topographic image (1.5 μm x 0.75 μm) of the pair of chiral structures produced following A. Image was acquired in a 0.02 mM C_{18} solution under a force of 6.7 nN and a scanning speed of 3.76 μm/s. Lateral scale bar is 0.2 μm.

Figure 4.2. (A) An S-spiral defined by the parametric equations (7) and (8). (B) A 3.0 μm x 3.0 μm AFM topographic image containing the S-spiral of C_{18} inlaid in a C_8 SAM. AFM image was acquired in an ethanol solution containing 0.02 mM $C_{18,}$ under a force of 6.7 nN and at a speed of 7.52 μm/s. Lateral scale bar is 0.5 μm. (C) Schematic diagram of nanografted C_{18} inlaid in the C_8 SAM revealing the adsorption conformation of the alkanethiols.

Figure 4.3. (A) The design of a 6-bladed fan feature with R chirality. (B) A 6 μm x 6 μm AFM topographic image taken after production of the R-bladed fan shown in (A). The image was

acquired in DMSO under an imaging force of 18 nN at 17.53 μm/s. Scale bar is 1.0 μm. (C) Schematic diagram illustrating the molecular adsorbates and terminal functionalities across the patterned region.

Figure 4.4. (A) An AFM topographic image taken after scanning the chiral grayscale image inset on a MA surface. (B) Lateral image acquired simultanesouly. Both images were collected in DMSO under 70 nN and a speed of 22.54 μm/s. Scale bars are 1.0 μm.

Figure 4.5 AFM topographic image of a 3 x 3 array of chiral structures produced following similar protocols as that in Figure 4.3. Each chiral structure is a 6-bladed fan with R chirality. Dark features correspond to anthracene termini while the lighter features are the bromine termini of the PGMA chains. The image was acquired in DMSO under an imaging force of 18 nN at 17.52 μm/s. Scale bar = 1.0 μm.

Figure 4.6. (A) A design of a R^R hierarchical spiral. (B) A 11.4 μm x 10.1 μm deflection image of the R^R hierarchical spiral produced following the design in (A). The image was acquired in DMSO under an imaging force of 51 nN at 37.56 μm/s. The lateral scale bar is 2.0 μm.

Figure 4.7. The four AFM deflection images of the hierarchical chiral spirals produced following the designs. All four possible combinations of chirality were designed and produced, as indicated in the images. All images were acquired in DMSO under the imaging force of 51, 13, 47 and 23 nN, with the scanning speed of 37.56, 31.30, 35.06 and 32.55 μm/s, respectively, in the four experiments. All lateral scale bars = 2.0 μm.

Figure 5.1. Schematic diagram of an integrated AFM with microfluidic delivery probe. An enlarged view illustrates the probe−surface contact. The chemical structure of solute, PEG-*bis*Tz, is also shown. The inset at the lower left is a SEM image of the nanopipette apex with a 300 nm aperture. Scale bar is 500 nm.

Figure 5.2. (A) An AFM topographic image of an array of PEG-*bis*Tz spherical caps. (B) A zoom-in view of a single feature as indicated in (A). The top inset is the corresponding cursor profile. (C) A further zoom-in view from the region as indicated (B).

Figure 5.3. (A) AFM topographic image of an array of PEG-*bis*Tz spherical caps created with various dwell times from 0.1 to 5 s under pressure of 200 mbar. (B) Plot showing the variation of the dimensions of PEG-bisTz spherical caps with dwell time.

Figure 5.4. (A) An AFM topographic image of 4 PEG-*bis*Tz lines from an array of 20 lines with periodicity of 5 μm. (B) An AFM topographic image of 4 PEG-*bis*Tz lines from an array 20 lines with periodicity of 5 μm. The stage movement in (B) is perpendicular to that in (A). (C) Combined cursor profiles from the lines indicated in (A) (red) and (B) (blue), and the schematic diagram indicates the movement directions. (D) AFM topographic image of an array of 9 PEG-*bis*Tz lines formed with increasing speed, under the delivery pressure of 200 mbar.

Figure 5.5. (A) AFM topographic image of a representative area of PEG-*bis*Tz mesh. (B) Cursor profile of two cursors in (A). (C) 3D display of the zoom-in of the green square in (A). (D) Schematic diagram of droplet delivery on SAM. (E) Schematic diagram of continuous line delivery, (F) Schematic diagram illustrating the difference of hypothetical solution distribution and actual distribution, with the darker color line representing the dried line from the first printed set.

Figure 5.6. AFM topographic images of a representative region of the three PEG-*bis*Tz grids with periodicity of (A) 15 μm, (B) 10 μm and (C) 5 μm, respectively. Each line in the first array was printed diagonally from top-left to bottom-right in each image. Each line in the second array was produced from lower-left to upper-right in each frame. (D) Cursor profiles as indicated in images (A), (B) and (C), respectively.

Figure 5.7. (A) 20 x 20 μm AFM topographic image from the printed area following the protocol described above. (B) Ligation between surface bound PEG-*bis*Tz and C12-*bis*TCO in toluene solution form multiblock copolymers.

Figure 6.1: High resolution lateral AFM image of mithrene's (001) plane. The lateral scale bar of the AFM image is 1.0 nm.

Figure 6.2 Deflection AFM images of mithrene crystals in isopropyl alcohol. (A) Low force (5.1 nN shearing) of a mithrene crystal before any high force scans. (B) After 51 nN shear force. (C) After 153 nN shear force. (D) After 255 nN shear force. Lateral scale bars are 500 nm.

Figure 6.3. TERS and far field Raman spectra of gold coated mithrene crystals. The peak assignments for all major peaks are labelled, with the green text representing new peaks on the TERS spectra compared to far field.

Figure 6.4: AFM topographic images (1.2 μm x 1.2 μm) of (A) CNCs, (B) DS-CNCs, and (C) AQ-CNCs. All images were acquired using tapping mode in ambient. Scale bars = 0.2 μm. AFM amplitude images of aggregates are shown for (D) CNCs, (E) DS-CNCs and (F) AQ-CNCs samples

LIST OF TABLES

Table 3.1. The Weight Average Molecular Weight (M_w), Number Average Molecular Weight (M_n), and PDI of the Synthesized PGMA for 5, 10, 20 min Polymerization Time

Table 4.1 Summary of hierarchical chiral structures produced, representing all four possible hierarchical chiralities. The top block lists the equations and dimensions of the individual Archimedean spirals. The bottom block lists the dimensions of the rectangular spirals.

Table 5.1. The PEG-*bis*Tz spherical caps formed via controlled assembly, in correlation with contact time.

Table 5.2. The PEG-*bis*Tz nanolines formed via controlled assembly, in correlation with the moving speed of the probe along the line

Table 6.1. Normal and shear forces for the AFM deflection images in Figure 6.2.

Table 6.2. Raman peak assignments for TERS of mithrene.

Table 6.3: Dimensions of individual CNCs measured from Figure 6.4 images A-C.

CHAPTER 1

Introduction

1.1 Three Dimensional Nanoprinting via Scanning Probe Microscopy Based Nanolithography.

Creating 3D nanostructures by design is one of the current holy grails of surface science and nanotechnology. The ability to create custom 3D nanostructures has a variety of potential applications, including catalysis,[1, 2] sensors,[3, 4] nanophotonics,[5, 6] nanoelectronics[7, 8] and even water treatment.[9, 10] This multitude of potential applications speaks to the critical importance of developing a reliable means to create 3D nanostructures from a variety of materials. Macroscale 3D printers, like those available for home and industrial use, are an appealing method for the construction of 3D materials; building up the structure layer by layer, with precise control over the morphology and material of each layer.[11, 12] Unfortunately, these consumer units, as well as more complex industrial ones, cannot reach the level of precision needed to create nanoscale structures, as their highest resolution is on the order of tens of microns. To address this limitation, Atomic Force Microscopy (AFM) was chosen, as it can reach an atomic scale resolution.[13, 14] Combining this nanoscale resolution with surface chemistry will enable the fabrication of custom 3D nanostructures by design. Our lab has an extensive history of utilizing nanolithography to selectively modify surfaces and create nanoscale features.[15, 16]

1.2 Thesis Objective.

In this dissertation, three advances are presented in our development of 3D nanolithography. The first is the utilization of mechanochemistry in conjunction with AFM-based nanolithography to create functional nanostructures. The second builds atop of this development and extends the capability to creating nanochiral features. The third reports the preliminary success in constructing 3D nanostructures. Collectively, this thesis clearly demonstrates the concept and feasibility of the approach, paving the way for developing 3D nanoprinting into a new tool in additive manufacturing, and enabling new science and technological applications.

1.2.1 Nanofabrication Via Localized Mechanophore Activation.

In the first method, we applied AFM-based nanolithography to a covalently bound mechanophore system. In brief, a substrate was functionalized with a mechanically labile group known as a mechanophore.[17] Mechanochemistry is an attractive candidate for surface modification, as mechanically sensitive molecules known as mechanophores could theoretically be activated with an AFM tip.[18] Mechanophore activation can be used to great effect for a variety of desirable chemical transformations, including depolymerization, catalytic reactions, and small molecule release.[19] Here, we used a mechanophore known as maleimide-anthracene, which was covalently bound to the substrate.[17] After linkage to the surface was established, polymer tails were grown from each mechanophore group, effectively yielding a ‘carpet’ with embedded mechanophore groups. A sharp (nm radius) AFM tip was scanned over the surface in two different force regimes, chosen based on the desired outcome. Scanning at low applied forces, the AFM tip imaged the surface, revealing its local topography. Upon scanning with a sufficiently high force, a scanned

region could be selectively activated, resulting in spatially controlled activation of the surface. This spatially controlled activation allows us to selectively choose our areas of activation, and thus control the exposure of different chemical moieties on the surface. This concept of nanolithography has been reported previously with self-assembled monolayers (SAMs),[1-2] now its application to a mechanophore system allows us to expand this technique from 2D to 3D structure fabrication. A key component of this is the reactive site exposed upon activation of the mechanophore, which could be built upon to create subsequent, covalently linked layers. In the maleimide-anthracene system, anthracene functions more as a check to verify activation, as it exhibits characteristic emission at 420 nm under excitation by a mercury lamp centered at 360 nm. We were able to successfully demonstrate the localized activation of the maleimide-anthracene mechanophore by tuning the force applied by the AFM tip to either imaging or activation regimes. This accurate force and spatial control was then applied to create features ranging from simple to complex, allowing us to create both binary and multilevel contrast designs, further advancing the applications of AFM-based nanolithography.

1.2.2 Nanofabrication of Chirality by Design Using AFM.

The second method builds atop our previous success, demonstrating that this same localized activation method could be applied to create a variety of chiral features by design. Chirality is traditionally associated intrinsically chiral molecules, such as lysine or alanine. However, there is another type of chirality that is less commonly discussed known as organizational chirality, where the chirality is derived from the arrangement of molecules on the surface.[20, 21] This chirality can be found for both chiral and achiral molecule systems, opening up the possibility of creating chiral

features with intrinsically achiral molecules. Past work in this field has primarily been divided into two categories: self-assembly of molecules with organizational chirality and patterning of thin films to create organizational chirality.[22] The former is more widely studied, however it is intrinsically limited in terms of the systems it applied to, as the formation of structures with organizational chirality is at the mercy of thermodynamics and control of the features formed is limited. The latter is of key interest to us, as our methodology could be used to create chiral features on functionalized surfaces. Previously, fabrication of features with organizational chirality has been achieved in polymer thin films using an AFM tip for patterning. Measurements of the chirality of the surface via liquid crystal rotation revealed that the patterned organizational chiral features did in fact possess chirality, affecting the strength and direction of the liquid crystal rotation by varying the pattern spacing and handedness.[23] We expand up the zigzag lines fabricated in the thin film systems by creating more complex structures such as spirals, multi-shade features and hierarchical features. This expanded capability of AFM-nanolithography to create these chiral nanostructures paves the way for future applications in enantioselective separation and enantiomeric heterogeneous catalysis.

1.2.3 Controlled Assembly via Microfluidic Delivery for the Creation of Custom Nanostructures.

The third method utilizes a microfluidic delivery system known as a Fluid FM, which is capable of delivery incredibly small volumes (<0.4 aL) of solution to a surface, with nm scale precision. This means of solution delivery opens a world of possibilities for creating nanostructuress by design. Previous work with this system[3-4] has demonstrated its feature

fabrication capabilities with large molecules such as star polymers and UV-glue. Here, we expand the repertoire of materials to include small molecules, in this case poly(ethylene glycol) (PEG-*bis*Tz), which has a dynamic radius of 1.5 nm. This methodology was used to successfully create both 0D dot, 1D lines and 3D grid features. Varying the spacing of this patterning of the lines on the surface also allowed us to control the redistribution of the solution through its solvent philic nature. Stabilization of the features on the surface was achieved by reacting the PEG-*bis*Tz with *trans*-cyclooctene (TCO), resulting in an array of stable features. These grid structures demonstrate preliminary success in creating 3D nanostructures using controlled assembly of small molecules. This advance demonstrates the feasibility of our approach and enables new science and technological applications of this customizable method.

1.3 Structure of the thesis

Following the introduction in the first chapter, Chapter 2 describes the fundamental techniques used in this paper: AFM and microfluidics. Chapter 3 describes the application of AFM-based nanolithography to selectively activate a surface bound mechanophore, maleimide-anthracene, with the end result of creating nanostructures by design. This fabrication is further expanded in Chapter 4, where the technique is used in conjunction with surface chemistry to create organizational chiral features by design using this same mechanophore system. Chapter 5 employs microfluidics to create nanoscale features by design using controlled assembly of small molecules. Lastly, Chapter 6 summarizes conclusions and ongoing and future work.

1.4 References.

1. Xu, G.; Bai, H. W.; Huang, X. Q.; He, W. B.; Li, L. L.; Shen, G.; Han, G. R., Self-assembled 3D flower-like perovskite PbTiO3 nanostructures and their application in the catalytic oxidation of CO. *Journal of Materials Chemistry A* **2015,** *3* (2), 547-554.

2. Fan, Q. F.; Lan, Q.; Zhang, M. L.; Fan, X. M.; Zhou, Z. W.; Zhang, C. L., Preparation and photocatalytic activities of 3D flower-like CuO nanostructures. *J Semicond* **2016,** *37* (8).

3. Yim, E. K. F.; Pang, S. W.; Leong, K. W., Synthetic nanostructures inducing differentiation of human mesenchymal stem cells into neuronal lineage. *Exp Cell Res* **2007,** *313* (9), 1820-1829.

4. Umar, A.; Ibrahim, A. A.; Kumar, R.; Almas, T.; Sandal, P.; Al-Assiri, M. S.; Mahnashi, M. H.; AlFarhan, B. Z.; Baskoutas, S., Fern shaped La2O3 nanostructures as potential scaffold for efficient hydroquinone chemical sensing application. *Ceram Int* **2020,** *46* (4), 5141-5148.

5. von Freymann, G.; Ledermann, A.; Thiel, M.; Staude, I.; Essig, S.; Busch, K.; Wegener, M., Three-Dimensional Nanostructures for Photonics. *Advanced Functional Materials* **2010,** *20* (7), 1038-1052.

6. Busch, K.; von Freymann, G.; Linden, S.; Mingaleev, S. F.; Tkeshelashvili, L.; Wegener, M., Periodic nanostructures for photonics. *Phys Rep* **2007,** *444* (3-6), 101-202.

7. Jiang, H.; Lee, P. S.; Li, C. Z., 3D carbon based nanostructures for advanced supercapacitors. *Energ Environ Sci* **2013,** *6* (1), 41-53.

8. Duan, X. J.; Lieber, C. M., Nanoelectronics Meets Biology: From New Nanoscale Devices for Live-Cell Recording to 3D Innervated Tissues. *Chem-Asian J* **2013,** *8* (10), 2304-2314.

9. Zhong, L. S.; Hu, J. S.; Liang, H. P.; Cao, A. M.; Song, W. G.; Wan, L. J., Self-assembled 3D flowerlike iron oxide nanostructures and their application in water treatment. *Advanced Materials*

2006, *18* (18), 2426-+.

10. Fei, J. B.; Cui, Y.; Yan, X. H.; Qi, W.; Yang, Y.; Wang, K. W.; He, Q.; Li, J. B., Controlled preparation of MnO2 hierarchical hollow nanostructures and their application in water treatment. *Advanced Materials* **2008,** *20* (3), 452-+.

11. Chia, H. N.; Wu, B. M., Recent advances in 3D printing of biomaterials. *J Biol Eng* **2015,** *9*.

12. Egorov, V.; Gulzar, U.; Zhang, Y.; Breen, S.; O'Dwyer, C., Evolution of 3D Printing Methods and Materials for Electrochemical Energy Storage. *Advanced Materials* **2020,** *32* (29).

13. Giessibl, F. J.; Binnig, G., Investigation of the (001) Cleavage Plane of Potassium-Bromide with an Atomic Force Microscope at 4.2-K in Ultra-High Vacuum. *Ultramicroscopy* **1992,** *42*, 281-289.

14. Ohnesorge, F.; Binnig, G., True Atomic-Resolution by Atomic Force Microscopy through Repulsive and Attractive Forces. *Science* **1993,** *260* (5113), 1451-1456.

15. Xu, S.; Laibinis, P. E.; Liu, G.-y., Accelerating the Kinetics of Thiol Self-Assembly on GoldA Spatial Confinement Effect. *Journal of the American Chemical Society* **1998,** *120* (36), 9356-9361.

16. Xu, S.; Liu, G. Y., Nanometer-scale fabrication by simultaneous nanoshaving and molecular self-assembly. *Langmuir : the ACS journal of surfaces and colloids* **1997,** *13* (2), 127-129.

17. Sulkanen, A. R.; Sung, J.; Robb, M. J.; Moore, J. S.; Sottos, N. R.; Liu, G. Y., Spatially Selective and Density-Controlled Activation of Interfacial Mechanophores. *Journal of the American Chemical Society* **2019,** *141* (9), 4080-4085.

18. Brantley, J. N.; Wiggins, K. M.; Bielawski, C. W., Polymer mechanochemistry: the design and study of mechanophores. *Polym Int* **2013,** *62* (1), 2-12.

19. Li, J.; Nagamani, C.; Moore, J. S., Polymer Mechanochemistry: From Destructive to

Productive. *Accounts Chem Res* **2015,** *48* (8), 2181-2190.

20. Gellman, A. J., Chiral Surfaces: Accomplishments and Challenges. *Acs Nano* **2010,** *4* (1), 5-10.

21. Bombis, C.; Weigelt, S.; Knudsen, M. M.; Norgaard, M.; Busse, C.; Laegsgaard, E.; Besenbacher, F.; Gothelf, K. V.; Linderoth, T. R., Steering Organizational and Conformational Surface Chirality by Controlling Molecular Chemical Functionality. *Acs Nano* **2010,** *4* (1), 297-311.

22. Whitesides, G. M.; Grzybowski, B., Self-assembly at all scales. *Science* **2002,** *295* (5564), 2418-2421.

23. Pendery, J.; Ferjani, S.; Rosenblatt, C.; Petschek, R. G., Spatially controllable surface chirality at the nanoscale. *Epl-Europhys Lett* **2011,** *96* (2).

24. Schriber, E. A.; Popple, D. C.; Yeung, M.; Brady, M. A.; Corlett, S. A.; Hohman, J. N., Mithrene Is a Self-Assembling Robustly Blue Luminescent Metal–Organic Chalcogenolate Assembly for 2D Optoelectronic Applications. *ACS Applied Nano Materials* **2018,** *1* (7), 3498-3508.

25. Trang, B.; Yeung, M.; Popple, D. C.; Schriber, E. A.; Brady, M. A.; Kuykendall, T. R.; Hohman, J. N., Tarnishing Silver Metal into Mithrene. *Journal of the American Chemical Society* **2018,** *140* (42), 13892-13903.

26. Liu, N.; Sun, G.; Zhu, J., Photo-induced self-cleaning functions on 2-anthraquinone carboxylic acid treated cotton fabrics. *Journal of Materials Chemistry* **2011,** *21* (39), 15383-15390.

27. Zhu, Y. W.; Sulkanen, A.; Liu, G. Y.; Sun, G., Daylight-Active Cellulose Nanocrystals Containing Anthraquinone Structures. *Materials* **2020,** *13* (16).

CHAPTER 2

Experimental

2.1 Atomic Force Microscopy

Atomic force microscopy (AFM) was invented in 1986 by Binnig, Quate and Gerber, providing means to image a surface with a resolution on the nanometer scale, expanding the scope of suitable samples to include a variety of materials previously unsuitable for scanning tunneling microscopy.[1] The resolutions achievable using AFM far exceed that of traditional light-based lithography,[2] with lateral and vertical resolutions reaching as high as 0.1 Å and 0.01 Å respectively.[3] In addition to its superior spatial resolution, AFM microscopy can apply forces as small as 10^{-18} N,[1] allowing for the imaging of delicate samples without destruction.[4-6]

AFM is a scanning probe technique, and functions by scanning a surface with an ultra-sharp tip in a raster pattern, mapping the topography of the surface. The tip is kept in contact with the surface using a feedback loop, maintaining one of multiple potential modes of operation. The signal for the feedback loop is typically generated by reflecting a laser off the back of the cantilever near the end and focusing the reflected beam onto a photodiode detector (PD),[7] as shown in Figure 2.1. By monitoring the position of the beam on the photodiode, the deflection and tip position can be tracked. A piezo mounted on the cantilever allows the tip-surface distance to be controlled to maintain a desired deflection or oscillation of the cantilever. The combined movement of the piezo and bending of the cantilever is translated into a topographical map of the surface and a readout of tip-surface interactions.[8] The torsional rotation of the cantilever can also be tracked through the lateral movement of the laser beam on the photodiode, yielding additional information about tip-

surface interactions.

This super sensitive monitoring of the tip deflection and movement, combined with the precise piezo positioning, is what enables the sub-nanometer resolution mapping of the surface, which is substantially lower than the optical diffraction limit of ~250 nm associated with conventional light-based microscopy.

Two common modes of AFM operation are the constant contact and intermittent contact modes. The most common mode is contact mode, where the tip is brought into contact with the surface until the desired level of cantilever deflection is reached. When the surface is scanned perpendicularly to the long axis of the cantilever, the torsional rotation of the cantilever can be monitored, yielding frictional information about the surface separated from the deflection of the cantilever. This mode yields both topographic and lateral information about the surface scanned. The second most common mode is intermittent contact mode, or tapping mode, in which a cantilever is subjected to an oscillating voltage close to the resonant frequency of the cantilever, causing the cantilever to oscillate.[9, 10] The oscillating tip is brought close to the surface until the desired level of oscillation dampening is achieved due to the attenuating contact with the surface. The dampening of the tip oscillation is monitored through the laser's reflection onto the photodiode, creating a feedback loop where the piezo is used to move the tip closer to or further from the surface in order to maintain the desired attenuation. The movement of the piezo is used to construct a topographic plot of the surface. In additional to the topographic information generated, the offset phase of the measured cantilever oscillation can be compared to the applied waveform, providing information about the mechanical properties of the surface struck by the cantilever. This tapping mode is especially helpful for delicate samples,[11] or samples proven too

'sticky' for contact mode imaging.[12]

Both contact and tapping modes were used in this work for material characterization, and the details of each are described in the experimental sections of each chapter. The combination of high spatial precision and force control not only enables characterization of a variety of surfaces, but also makes the atomic force microscope useful for nanomanipulation[13] and nanolithography.[14, 15] Utilizing these capabilities of the atomic force microscope, we can not only produce functional nanostructures by design, but image them with the same instrument used for fabrication.

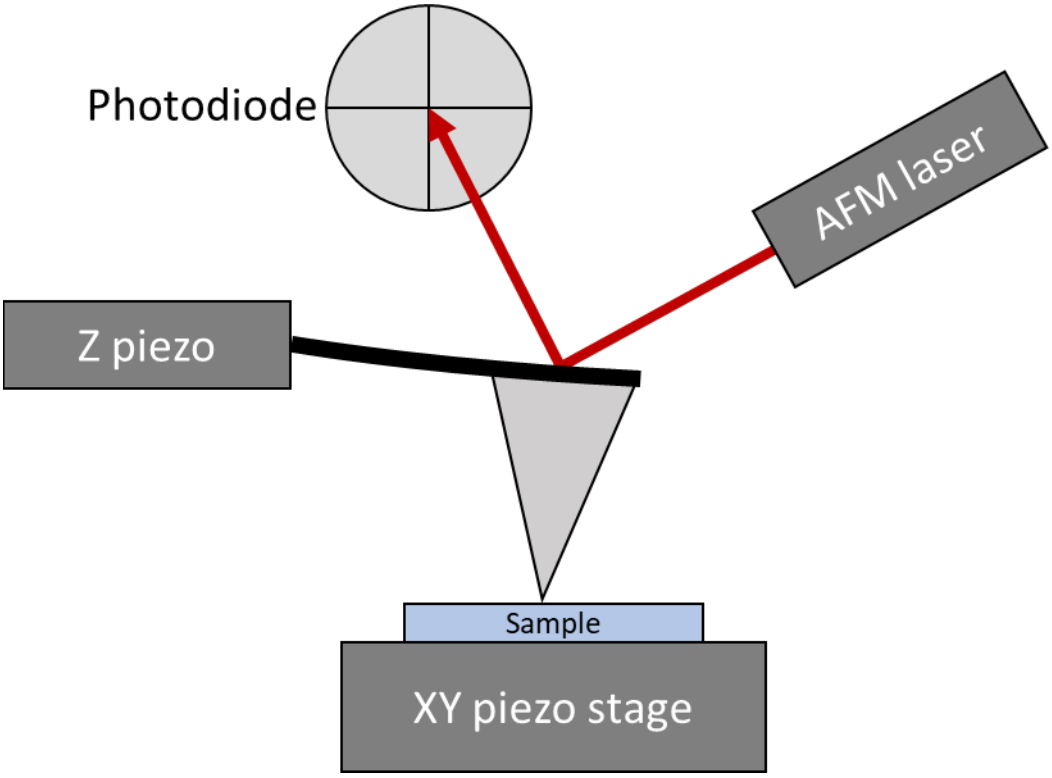

Figure 2.1. Schematic diagram of a deflection type AFM.

2.1 Microfluidic Delivery

A popular technique in 3D writing and additive manufacturing is the direct delivery method, which can

produce structures down to micrometer scale. Similar to the fused deposition model 3D printers available for consumers, structures are produced by extruding a fluid ink through a nozzle at a controlled rate,[16, 17] often involving a curing step to retain the shape. Particulate and polymeric materials suspended in a liquid solvent are suitable inks for this method of delivery. Alternatively, solid materials, such as polylactic acid (PLA), polyethylene terephthalate glycol (PETG), Nylon and other plastics can be heated to allow them to be extruded through the nozzle and then cooled to solidify their shape. Sub-millimeter precision is easily achievable for creating 2D/3D structures via direct delivery, however reaching nanometer and micrometer levels of precision is challenging due to the required accuracy in positioning and material dispensing. Micrometer precision has been achieved so far by combining smaller injection systems and suitable materials that can self-cure upon deposition.[18] Further miniaturizing the features (ideally reaching the nanometer scale) is challenging due to the high accuracy required for both reliable positioning and material delivery in order to achieve nanometer scale inter and intra layer alignment. This desired miniaturization of 2D and 3D features can be achieved by combining atomic force microscopy's high spatial precision with sub-attoliter (sub-aL) delivery precision of microfluidics, which has been reported previously.[19, 20]

The direct delivery of our chosen ink was carried out using an integrated AFM and microfluidic instrument, FluidFM BOT, shown in Figure 2.2. This combination enabled 3D printing with nanometer positioning prevision and sub-aL volume delivery control. The stage was mounted onto an inverted optical microscope, allowing monitoring of position and delivery but necessitating transparent samples. The range of movement for the XY stage was 240 mm x 74 mm, with a precision of 100 nanometers. The Z movement was independently controlled with a precision of 4 nm over a 50 mm range

Combining the volume control with the high precision positioning control of the FluidFM, custom features can be fabricated with a wide variety of inks, enabling unparalleled customization

of both feature morphology and functionality.

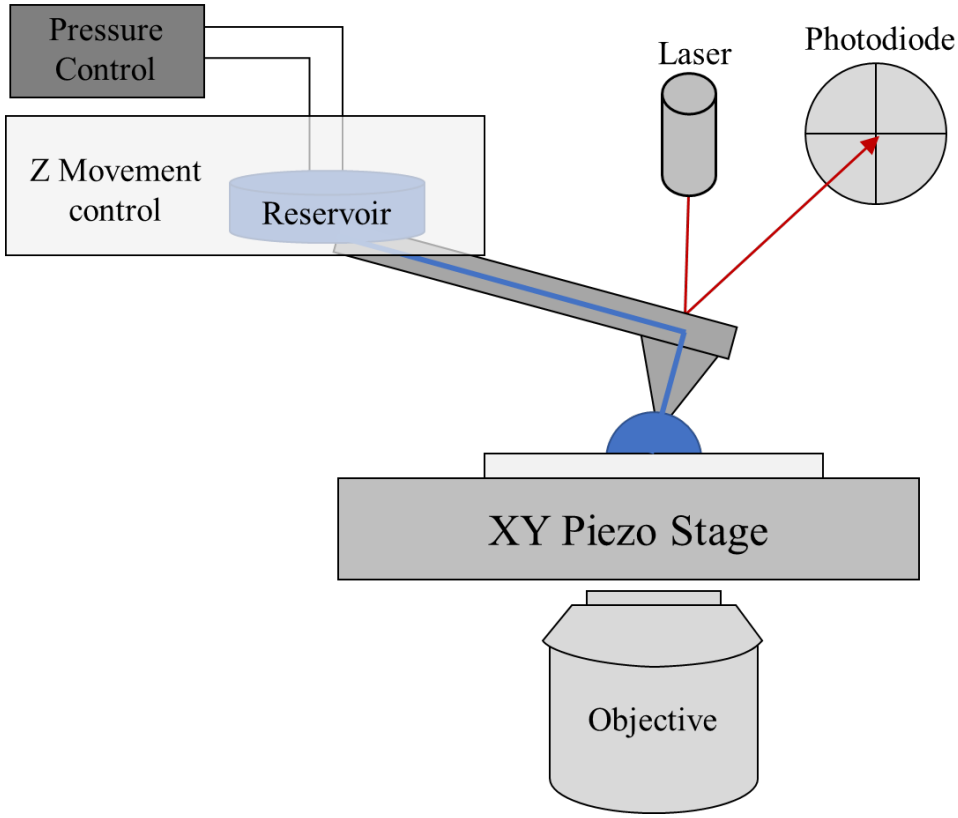

Figure 2.2. Schematic diagram of the key parts of the microfluidic AFM (FluidFM).

2.3 References

1. Binnig, G.; Quate, C. F.; Gerber, C., Atomic Force Microscope. *Physical Review Letters* **1986,** *56* (9), 930-933.

2. de Lange, F.; Cambi, A.; Huijbens, R.; de Bakker, B.; Rensen, W.; Garcia-Parajo, M.; van Hulst, N.; Figdor, C. G., Cell biology beyond the diffraction limit: near-field scanning optical microscopy. *J Cell Sci* **2001,** *114* (23), 4153-4160.

3. Neuman, K. C.; Nagy, A., Single-molecule force spectroscopy: optical tweezers, magnetic tweezers and atomic force microscopy. *Nat Methods* **2008,** *5* (6), 491-505.

4. Kuzuya, A.; Sakai, Y.; Yamazaki, T.; Xu, Y.; Komiyama, M., Nanomechanical DNA origami 'single-molecule beacons' directly imaged by atomic force microscopy. *Nature Communications* **2011,** *2*.

5. Foster, B., New Atomic Force Microscopy (AFM) Approaches Life Sciences Gently, Quantitatively, and Correlatively. *Am Lab* **2012,** *44* (4), 24-+.

6. Kurland, N. E.; Drira, Z.; Yadavalli, V. K., Measurement of nanomechanical properties of biomolecules using atomic force microscopy. *Micron* **2012,** *43* (2-3), 116-128.

7. Putman, C. A. J.; Degrooth, B. G.; Vanhulst, N. F.; Greve, J., A Detailed Analysis of the Optical Beam Deflection Technique for Use in Atomic Force Microscopy. *J Appl Phys* **1992,** *72* (1), 6-12.

8. Butt, H. J., Measuring Electrostatic, Vanderwaals, and Hydration Forces in Electrolyte-Solutions with an Atomic Force Microscope. *Biophys J* **1991,** *60* (6), 1438-1444.

9. Liu, Z. G.; Li, Z.; Wei, G.; Song, Y. H.; Wang, L.; Sun, L. L., Manipulation, dissection, and lithography using modified tapping mode atomic force microscope. *Microsc Res Techniq* **2006,** *69* (12), 998-1004.

10. Putman, C. A. J.; Vanderwerf, K. O.; Degrooth, B. G.; Vanhulst, N. F.; Greve, J., Tapping Mode Atomic-Force Microscopy in Liquid. *Appl Phys Lett* **1994,** *64* (18), 2454-2456.

11. Howard, A. J.; Rye, R. R.; Houston, J. E., Nanomechanical basis for imaging soft materials with tapping mode atomic force microscopy. *J Appl Phys* **1996,** *79* (4), 1885-1890.

12. Umemura, K.; Arakawa, H.; Ikai, A., High-Resolution Images of Cell-Surface Using a Tapping-Mode Atomic-Force Microscope. *Jpn J Appl Phys 2* **1993,** *32* (11b), L1711-L1714.

13. Rubio-Sierra, F. J.; Heckl, W. M.; Stark, R. W., Nanomanipulation by atomic force microscopy. *Adv Eng Mater* **2005,** *7* (4), 193-196.

14. Xu, S.; Laibinis, P. E.; Liu, G.-y., Accelerating the Kinetics of Thiol Self-Assembly on GoldA Spatial Confinement Effect. *Journal of the American Chemical Society* **1998,** *120* (36), 9356-9361.

15. Xu, S.; Liu, G. Y., Nanometer-scale fabrication by simultaneous nanoshaving and molecular self-assembly. *Langmuir : the ACS journal of surfaces and colloids* **1997,** *13* (2), 127-129.

16. Fang, A. P.; Dujardin, E.; Ondarcuhu, T., Control of droplet size in liquid nanodispensing. *Nano Letters* **2006,** *6* (10), 2368-2374.

17. Gratson, G. M.; Xu, M. J.; Lewis, J. A., Microperiodic structures - Direct writing of three-dimensional webs. *Nature* **2004,** *428* (6981), 386-386.

18. Hirt, L.; Ihle, S.; Pan, Z. J.; Dorwling-Carter, L.; Reiser, A.; Wheeler, J. M.; Spolenak, R.; Voros, J.; Zambelli, T., Template-Free 3D Microprinting of Metals Using a Force-Controlled Nanopipette for Layer-by-Layer Electrodeposition. *Advanced Materials* **2016,** *28* (12), 2311-2315.

19. Gruter, R. R.; Voros, J.; Zambelli, T., FluidFM as a lithography tool in liquid: spatially controlled deposition of fluorescent nanoparticles. *Nanoscale* **2013,** *5* (3), 1097-1104.

20. Zhang, J. L.; Piunova, V. A.; Liu, Y.; Tek, A.; Yang, Q. B.; Frommer, J.; Liu, G. Y.; Sly, J., Controlled Molecular Assembly via Dynamic Confinement of Solvent. *J Phys Chem Lett* **2018,** *9* (21), 6232-6237.

CHAPTER 3

Spatially Selective and Density-Controlled Activation of Interfacial Mechanophores

3.1 Introduction.

Polymer mechanochemistry has attracted much interest recently to understand fundamental scientific questions on force-activation of chemical change, as well as for its technological potential related to the preparation of mechanoresponsive materials.[1-4] Mechanically sensitive molecules known as mechanophores are activated via force to trigger desirable chemical transformations such as color changes,[5-7] catalytic reactions,[8] depolymerization,[9] small molecule release,[10] and changes in electrical conductivity.[11] Immobilizing mechanophores on solid surfaces has provided new opportunities for producing functional materials with responsive interfaces such as polymer-silica particles,[12] polymer-cellulose,[13] and silk-epoxy materials,[14], and for applications including fabrication of sensors and nanodevices.

The commonly reported means of activation include applying mechanical forces to bulk polymeric materials,[6, 15, 16] ultrasonicating dilute polymer solutions,[17-19] or performing single molecule force spectroscopy on surface bound polymers.[20-24] More recently, a laser-spallation technique was utilized to activate and characterize mechanochemical transformations at a solid interface.[25] While previous approaches are effective at triggering activation, methods that enable nanometer spatial precision are critical for producing custom-designed structures, as well as fabricating nanocomposite materials and nanodevices with desired structural, physical, and chemical properties.

Atomic force microscopy (AFM) is known for its molecular resolution in imaging and lithography.[26, 27] In addition, AFM operates in various environments, including ultra-high vacuum,

ambient, and in solution, and as such, is versatile enough to accommodate a wide range of chemical reactions.[28-30] Furthermore, AFM enables accurate force control over a wide range: from pN to hundreds of μN in one experimental setup.[30-33] The local pressure at contact is tunable from kPa to GPa.[34] Finally, AFM enables surface nanolithography as well as structural characterization *in situ*.[35-38] Previously, AFM has been used as a nanolithography tool to pattern self-assembled monolayers (SAMs) such as alkane thiols on precious metals,[37, 39, 40] silanes on Si wafers and glass,[41] and polymers.[27, 42]

This work reports using AFM probes to activate mechanochemical reactions at interfaces. Taking advantage of the spatial precision and force tunability of AFM, this approach affords excellent control over the spatial activation of mechanochemical reactions on surfaces. This level of control over interfacial reactions enables the fabrication of complex structures with nanometer precision and signifies a critical step towards programming the surface chemistry molecule-by-molecule. The outcomes of our experiments demonstrate the feasibility for controlling mechanophore-based surface chemical reactions, 3D nanoprinting, and production of advanced coatings and composite materials that require nanopatterning or texture control, as well as nanodevices and sensor for mechanical stress and damage *in situ*.[1, 2, 43-45]

3.2 Experimental

3.2.1 Materials

Polished silicon wafers, Si(100) with 300 nm thermal oxide layer, were purchased from University Wafers Inc. (Boston, MA, U.S.A.) for sample fabrication. Dimethyl sulfoxide (DMSO) (≥99.9%) was purchased from Sigma-Aldrich (St. Louis, MO, U.S.A.) and used without further purification. Ethanol (200 proof) was purchased from Sigma Aldrich. Water (≥18.2 MΩ) was purified by a Milli-Q system (Q-GARD 2, Millipore, Billerica, MA, U.S.A.). Polished silicon wafers, Si(111) doped with boron, were purchased from Virginia Semi- conductor Inc. (Fredericksburg, VA, U.S.A.) and used for cantilever calibration. Sulfuric acid (95.0%), hydrogen peroxide (30% aqueous solution) were purchased from Sigma-Aldrich (St. Louis, MO, U.S.A.). Nitrogen gas (99.999%) was purchased from Praxair, Inc. (Danbury, CT, U.S.A.). AC240TS-R3 silicon cantilevers were purchased from Oxford Instruments Asylum Research (6310 Hollister Ave, Santa Barbara, CA, 93117, U.S.A.). All other materials were used without further treatment or modification, unless otherwise stated.

3.2.2 Active Fabrication Process.

Active specimens with Maleimide-Anthracene (MA) mechanophores immobilized on the surface were prepared with a surface functionalization approach following previously reported methods, shown in Figure 3.1.[25] In this work, the surface-bound MA mechanophores terminated with a bromoisobutyrate group were used to initiate a copper-catalyzed living radical

polymerization of glycidyl methacrylate to grow polymer brushes.

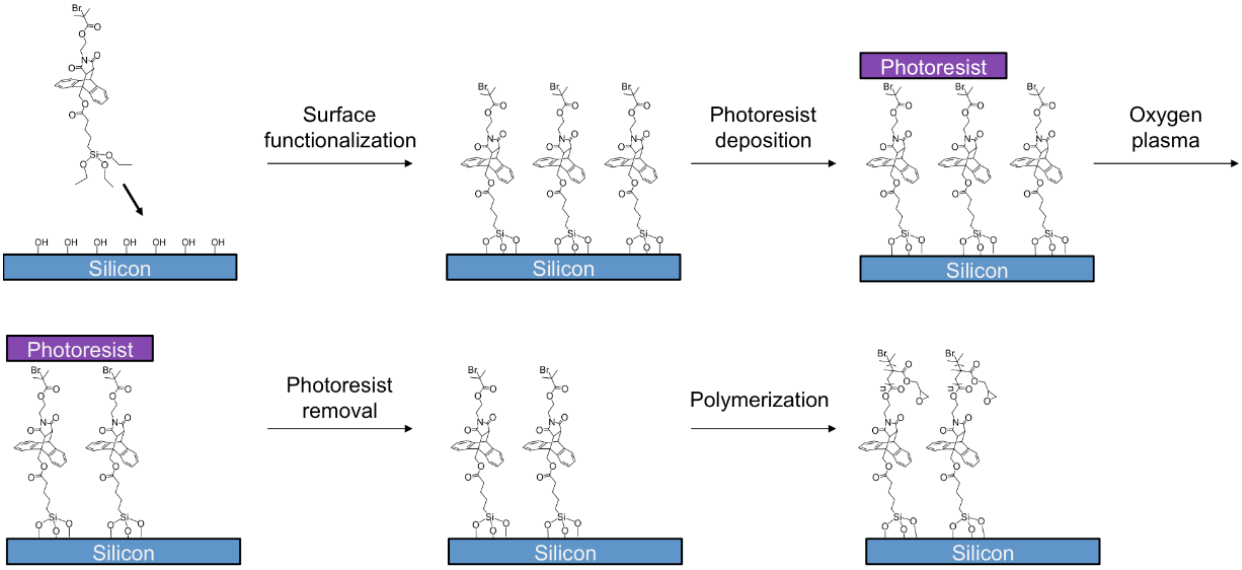

Figure 3.1. Fabrication steps for patterned PGMA brush-MA mechanophore grafted active specimen on silicon substrate.

3.2.3 Surface Functionalization of Silicon Substrate with MA Mechanophore.

500 nm thick silicon substrates with 300 nm thermally grown oxide layer were cleaned in piranha solution at 120 ℃ for 30 minutes. Cleaned substrates were washed with DI water and dried in a stream of air. The substrates were further dried in a convection oven at 120 °C for 30 min. For surface functionalization, cleaned substrates were immersed in a 10 mM toluene solution of functionalized maleimide-anthracene adduct and kept in a sealed container for 24 h on a bench top. After 24 h, the substrates were sonicated in toluene and subsequently rinsed with toluene, isopropyl alcohol, and DI water followed by drying under a stream of air.

3.2.4 Surface Patterning MA Mechanophore Functionalized Silicon Substrate.

The patterned MA surface was fabricated by photo patterning a photoresist (AZ 5214 E, microChem) and removing exposed MA moieties with oxygen plasma (Harric Plasma Cleaner Pdc-32g)[46]. After oxygen plasma treatment, residual photoresist was removed by rinsing with N-methyl-2-pyrrolidone.

3.2.5 Polymer Brush Formation on MA Functionalized Substrate.

Poly(glycidyl methacrylate) brushes with varying thicknesses were synthesized on MA initiator-functionalized substrates using activators regenerated by electron transfer atom transfer radical polymerization (ARGET-ATRP).[47] Silicon substrates with patterned MA initiator were placed in 20 ml vial containing 2 ml methanol/DMF/anisole (1:1:1 volume ratio). To the vial, 1.7 g of glycidyl methacrylate (Sigma-Aldrich, filtered through basic alumina to remove inhibitor) and 2 ml of a catalyst stock solution (containing 0.0036 mmol $CuBr_2$ and 0.036 mmol PMDETA) were added. After mixing, the vial was purged with nitrogen for 20 minutes. Ethyl-2-bromoisobutyrate (7 µl, EIB) was added to simultaneously initiate solution polymerization of glycidyl methacrylate along with the surface-initiated polymerization. The molecular weight of free polymer EIB-PGMA was used as a reference to estimate the degree of polymerization of the surface attached polymer.[48] The mixed solution was subjected to three cycles of freeze-pump-thaw process for complete degassing. After degassing, vial was filled with nitrogen and 1 ml ascorbic acid stock solution (8.4 mM ascorbic acid in methanol/DMF/anisole (1:1:1 volume ratio) solvent) was added. Four samples were prepared, which were polymerized for 10 minutes (three samples) and 20 minutes (one sample). After polymerization, the specimen was washed with DCM and ethanol. To remove

residual solvent, we dried the silicon substrate in a vacuum oven at 50 ℃ for 24 h. Representative size exclusion chromatography data is shown in Figure 3.2. The weight average molecular weight (M_w), number average molecular weight (M_n), and PDI of the synthesized polymer is summarized in Table 3.1. Thickness of the polymer brush was determined using AFM probe in DMSO, which were 11.4 ± 1.2 and 26.0 ± 1.3 nm. For the sample containing the gradient feature, spiral pattern, and the hierarchical 'T' pattern, the exposed silicon surface after oxygen plasma etching was functionalized in 10 mM 2-[methoxy(polyethyleneoxy)6-9propyl]trichlorosilane(oligomeric ethylene oxide) (Gelest) toluene solution. For the samples with the passivated oligomeric ethylene oxide surfaces, the polymer brush heights were 9.2 ± 0.6 and 10.7 ± 1.3 nm relative to the surrounding oligomeric ethylene oxide. The oligomeric ethylene oxide layer height was measured at 1.4 ± 0.2 nm.

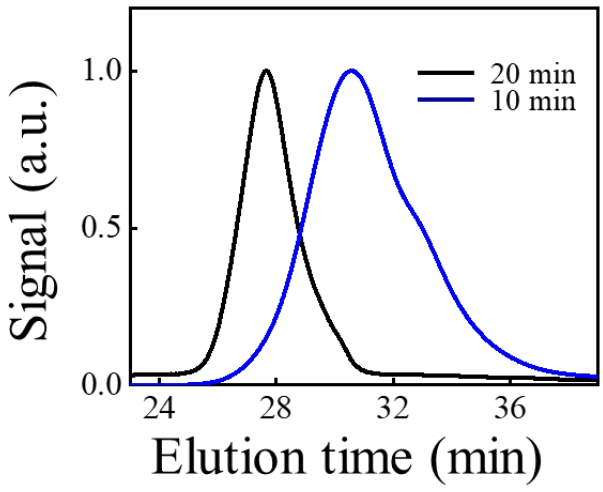

Figure 3.2. Representative size exclusion chromatography results of the synthesized PGMA for the 10- and 20-min polymerization times.

Table 3.1. The Weight Average Molecular Weight (M_w), Number Average Molecular Weight (M_n), and PDI of the Synthesized PGMA for 5, 10, 20 min Polymerization Time

Specimen	Figures 3.2, 3.4, 3.5	Figure 33.
Polymerization Time	10 min	20 min
M_w (kDa)	29.1	46.9
M_n (kDa)	22.2	40.8
PDI	1.31	1.15
Brush Height	11.4 ± 1.2 nm, 10.6 ± 0.6 nm, 12.1 ± 1.3 nm	26.0 ± 1.3

3.2.6 Control Specimen Fabrications.

The control specimen was fabricated to investigate the effects of high-load force on PGMA brush without the MA mechanophore. The control specimen was prepared using a similar fabrication steps to that of the active specimen. Piranha-cleaned silicon substrate was functionalized with (3-(trimethoxysilyl)propyl 2-bromo-2-methylpropionate, Gelest) by immersing it in 10 mM toluene solution for 24 h. The functionalized surface was subsequently patterned using photolithography. PGMA brush was prepared by ARGET-ATRP (20-minute reaction time) as described above. The thickness of the polymer brush was 9.6 nm in DMSO, which was determined by AFM.

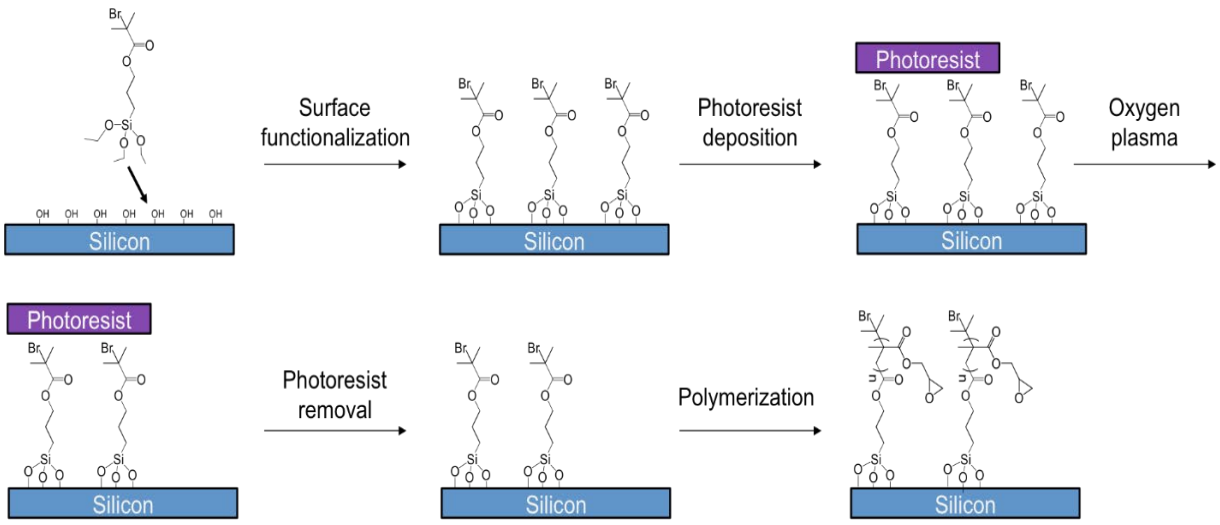

Figure 3.3. Fabrication steps for patterned PGMA brush grafted control specimen on silicon substrate.

3.2.7 Preparation of Silicon Wafers for Calibration.

Polished silicon wafers were used to calibrate the cantilever before AFM imaging and activation. The wafers were cleaned by immersion in piranha solution for 30 minutes and cleaned twice more with fresh piranha solution before being rinsed with copious amounts of milli-Q water. Cleaned wafers were subsequently stored in ultra-pure water, and rinsed with ethanol and dried under nitrogen before further use.

3.2.8 AFM Imaging

All mechanophore and control samples were characterized using an atomic force microscope (MFP-3D, Asylum Research Corp., Santa Barbara, CA). Silicon probes, AC 240-TS (Olympus

America, Central Valley, PA) were used for imaging and activation. The nominal force constant of the probes was 1.7 N/m, with a resonant frequency of 70 kHz in air. Silicon probes were used in their original state, with a brief cleaning in ethanol and nitrogen drying before each experiment. All experiments were carried out in DMSO in a liquid cell. Before imaging, all cantilevers were calibrated on a clean Si (111) wafers. In the DMSO media, the mechanophore features were imaged in contact mode with a load of 10-66 nN, with speeds ranging from 2.50-135.22 μm/s. The AFM images were acquired and analyzed using Asylum MFP-3D software developed on the Igor Pro 6.34 platform.

3.2.9 AFM Activation.

Activation of the surface bound mechanophore was achieved using an atomic force microscope (MFP-3D, Asylum Research Corp., Santa Barbara, CA). The mechanophore samples were imaged under low forces [10-66 nN] until suitable areas were found. Silicon probes, AC 240-TS (Olympus America, Central Valley, PA) were used for activation by scanning with a high force (ranging from 200 nN to 1.3 μN) in contact mode in DMSO. After the high force scan, the areas were imaged again with low force scans to determine the extent of mechanophore activation.

3.2.10 AFM Custom Design

Microlithography Mechanophore regions were imaged at low contact forces (10-66 nN) using AFM to determine suitable areas for microlithography. Utilizing custom design software in Igor Pro 6.34, a bitmap image (either user designed or taken from the internet) was uploaded into the

program, converted into greyscale and translated into force vectors. The color scale was assigned minimum and maximum force values, ranging from nanonewtons to micronewtons. Additional parameters, such as feature size, scan speed, lines per scan and scan angle were also specified. Feature fabrication using this method typically took anywhere from 2-8 minutes, depending on feature size, scan speed and image line density. After the lithography scan was completed, the area was imaged again under low force with the same AFM tip to assess success.

3.2.11 Fluorescence Measurement

Fluorescence images were acquired using a Cascade 512b high sensitivity camera, which was attached to Zeiss Axiovert 200M. A mercury lamp source was used with 360 nm centered/FWHM 11 nm band pass excitation filter, 410 nm pass dichroic mirror, and 420 nm/FWHM 20 nm band pass filter (Edmund Optics). For Figure 3.6 fluorescence measurements, the exposure time was set to 100 ms and 40x magnification on objective lens. Fluorescence images were processed with Image J.7 Fluorescence intensity was measured by averaging over 20 μm x 20 μm region. Normalized photoluminescence (Figure 3.6 right) was calculated by setting the average fluorescence intensity of 600 nN applied specimen to 100 and non-activated bare specimen as 0. For Figure 3.8 fluorescence measurements, the exposure time was 200 ms and 63x magnification on objective lens.

3.2.12 ToF-SIMS Imaging

Active specimens that were subjected to a contact force of 450 nN were analyzed with ToF-SIMS

(Physical Electronics PHI Trift III) imaging. For ToF-SIMS imaging, Au liquid source run with Au+ ion under static mode accelerated at 22 KeV energy was used as the source. Data was collected for 10-minute duration.

3.3 Results and Discussion

3.3.1 Spatially-selective Activation of Interfacial Mechanophore.

The concept of spatially-selective activation is illustrated in Figure 3.4, using the well-known maleimide-anthracene (MA) mechanophore. The MA mechanophore has been reported by us[12, 49] and others[50,51] to undergo a mechanically activated retro-Diels-Alder reaction (retro [4+2] cycloaddition) to form maleimide and anthracene in solution, and at nanoparticle-liquid interfaces. In this work, MA mechanophores were immobilized on a Si wafer surface via alkyl-siloxane self-assembly,[52] and a poly(glycidyl methacrylate) (PGMA) brush was grown subsequently. PGMA was chosen because the activation of the mechanophore would release the polymer brush, yielding a significant reduction of film height to enable *in situ* monitoring of activation. Synthesis of surface-bound MA mechanophores has been reported in previous literature and the formation of polymer brushes on Si wafers is described in detail in the experimental section.

The imaging and activation of the MA mechanophore were achieved in three steps. The mechanophore-functionalized polymer brush surface was first imaged in dimethyl sulfoxide (DMSO) in contact mode via AFM under a gentle force, e.g. 10 nN, or 0.35 GPa, pressure estimated using Hertzian contact mechanics.[30, 34] Upon selecting the activation region, the AFM probe was moved to the designated location and the contact force was increased, e.g. to 350 nN,

or 1.16 GPa. During the scan, molecules underneath the probe were subject to vertical pressure as well as lateral shear. The combined local mechanical perturbation is known to break van der Waals interactions, hydrogen bonds, chemosorbed species,[37, 53, 54] and ionic and covalent bonds.[55] Given that each MA mechanophore is specifically designed to undergo a force-activated retro-Diels-Alder reaction,[12] we envision a force range that could selectively activate the mechanophore without inducing scission of the covalent bonds in each polymer brush. The proof of this concept paves the way to generate locally defined patterns that are chemically differentiated according to the scanning trajectory of the AFM probe.

Our experimental studies had to first address variations in probe apexes by determining an activation threshold for each experiment. The threshold value was found by scanning a test area with systematically increasing loads. After high-load scanning of a designated area, the load was reduced to a low force, e.g. 10 nN, and the region was reimaged for changes in the surface morphology (Figure 3.4). The outcome and spatial-selectivity of each high-load scan was successfully characterized by AFM, *in situ*, as each activation event cleaves a polymer strand, reducing the layer's height by a measurable degree, and exposing surface bound anthracene. To confirm that the mode of activation was via the retro-Diels-Alder reaction, the substrates were examined by fluorescence microscopy, as anthracene exhibits fluorescence from 365-500 nm.[50]

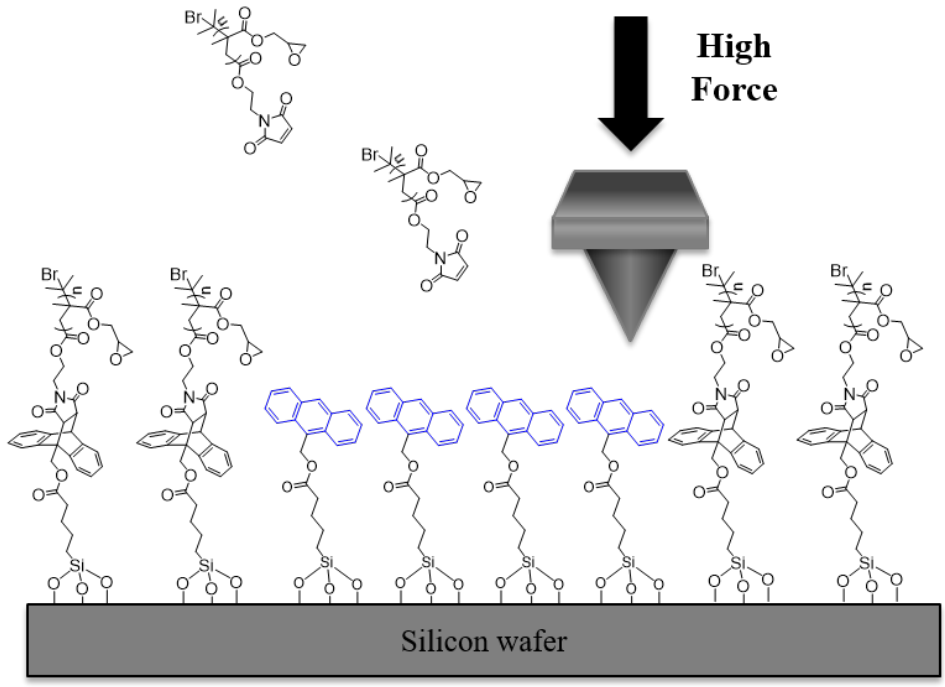

Figure 3.4. A schematic diagram illustrating activation of MA mechanophores at the interface between a polymer brush and silicon surface using an AFM probe. Each mechanophore activation produces a free maleimide and a surface-bound anthracene group via a retro [4+2] cycloaddition reaction.

The successful activation of the MA mechanophores is demonstrated in Figure 3.5, where an 18.6 µm x 18.6 µm region of PGMA polymer brush is shown in the center of Figure 3.5A. The height of the polymer brush measures 11.4 ± 1.2 nm above the Si-wafer surface. The central 5.46 µm x 4.80 µm region was selected to undergo a high-load (450 nN) scan in DMSO. The outcome is shown in Figure 3.5B, where the perturbed area appears 7.8 ± 1.3 nm lower than surrounding or 3.5 ± 0.6 nm above the wafer surface (schematic shown in Figure 3.5C). Under excitation of a mercury lamp (centered at 360 nm), the central region exhibited fluorescence at 410-430 nm (Figure 3.5D), which is characteristic of anthracene.[50] The AFM and fluorescence microscopy

images verify that the interfacial MA mechanophores underwent a retro [4+2] cycloaddition to generate surface-bound anthracene. Additionally, *ex situ* time-of-flight secondary ion mass spectroscopy (ToF-SIMS) further supports mechanophore activation (not pictured). The high spatial selectivity is evident from Figure 3.5B; the feature has sharp 90˚corners, and straight edges.

Control experiments were performed to verify that the high local force applied triggers the retro [4+2] cycloaddition of MA mechanophores without rupturing bonds elsewhere in the molecule. Identical experiments were carried out using a polymer brush, i.e. PGMA covalently linked to the Si-wafer surface without a mechanophore moiety (not pictured). The control sample was prepared following similar procedures used for fabrication of the brush in Figure 3.5. After being scanned under high force (450 nN), the control sample showed no discernable changes in the AFM topographic image within the force range used in this work. Fluorescence microscopy revealed no emission in the 410-430 nm region. The combined evidence from these control experiments indicates that only the weakest bonds, i.e. the MA mechanophore, were disturbed under 450 nN of force. Therefore, AFM provides a means for selective activation of interfacial MA mechanophores with high spatial fidelity.

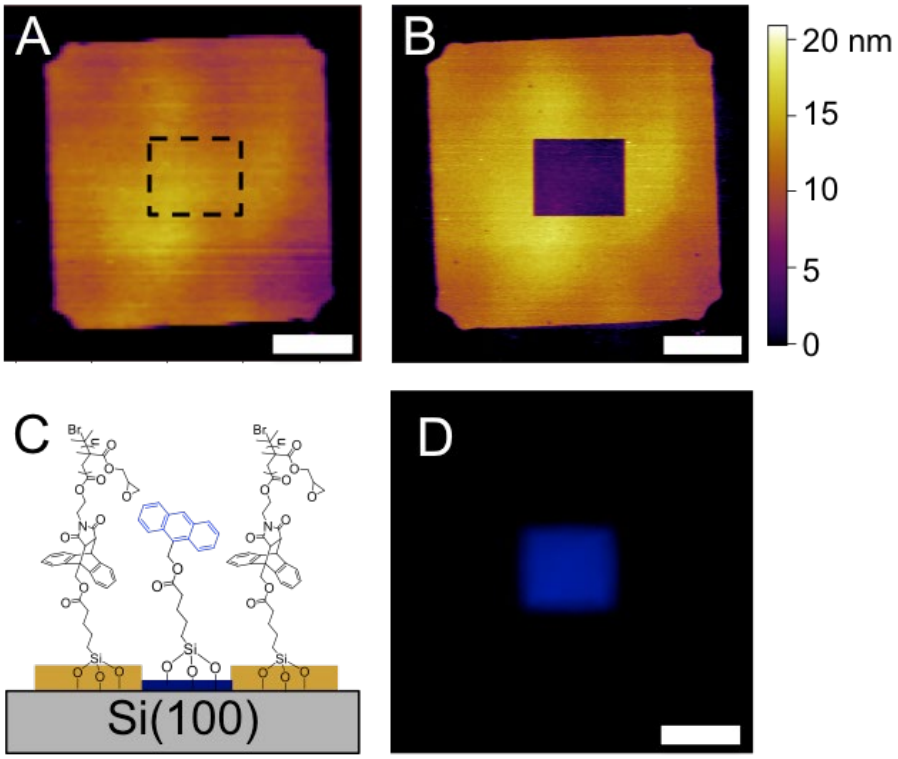

Figure 3.5. (A) A 24 x 24 µm AFM topographic image of a PGMA brush acquired in DMSO under 10 nN force. **(B)** The same area as (**A)** after the central 5.46 µm x 4.80 µm region was subjected to high force (450 nN) scans at 12.52 µm/s with 256 lines. **(C)** Schematic diagram illustrates the surface functionalities across the middle of image (**B**). **(D)** Fluorescence microscopy image of the same region as (**B)** collected from 410 to 430 nm. All scale bars are 5.0 µm.

3.3.2 Control Over the Density of Mechanophore Activation.

Given the force sensitivity of the MA mechanophores, controlling the density of mechanochemical activation is theoretically possible by varying the number and location of high force sites within a given area. Various means are available in AFM to control the number and

location of high load sites, e.g. by controlling the line density where the probe applies a high load, employing contact at sporadic sites instead of the entire region, or reducing the local contact force, which is equivalent to reducing transient contact area.[34, 56] In the example shown in Figure 3.6A, the outcomes under five loads (200, 300, 400, 500 or 600 nN) are compared. The PGMA polymer brush measured 26.0 ± 1.3 nm taller than the surrounding Si-wafer surface. For the lowest load of 200 nN, the outline of the central region is barely discernable, and minimal fluorescence is observed, indicating only a small portion of the MA mechanophores was activated. Between the 300 to 400 nN squares, drastic changes in both AFM topograph and the fluorescence intensity are evident. At the highest load of 600 nN, the central 5.8 μm x 4.8 μm region measured 24.6 ± 0.9 nm below the surrounding PGMA, and the fluorescence reached its highest intensity. Fluorescence images of the region confirmed the presence of surface-bound anthracene. Both the AFM height measurements and fluorescence intensities suggest quantitative activation of mechanophores within the scanned region, which used the deepest feature as a reference to quantify activation density as a function of AFM force (Figure 3.6B).

By using relative feature depth to quantify mechanophore activation density, we can further explore the mechanism of control over activation density. The height measured from AFM topography decreases with increasing MA activation, as the resulting anthracene is shorter than the PGMA brush, and thus the remaining PGMA chains adopt a more relaxed packing than the initial brush.[57, 58] Assuming a linear correlation, MA mechanophore activation is estimated from height measurements and plotted in Figure 3.6B,[59] and the quantification is consistent with fluorescence intensity measurements as seen from the combined plot. The control over the density of MA mechanophore activation is rationalized by the AFM probe-brush contact. A higher force

manifests as a higher contact diameter, and as a larger activation area in each scan line, while the inter-line spacing is constant under the set scan line density. This increase in activation area per line results in an overall height decrease for the scanned area. For example, at 512 line scans covering the central 5.8 µm x 4.8 µm area, the nearest neighbor line spacing would be 9.4 nm. With contact diameter larger than the inter-line spacing, complete activation of the mechanophores is expected, while reducing the load leads to contact diameters smaller than inter-line spacing, and thus a lower activation density.

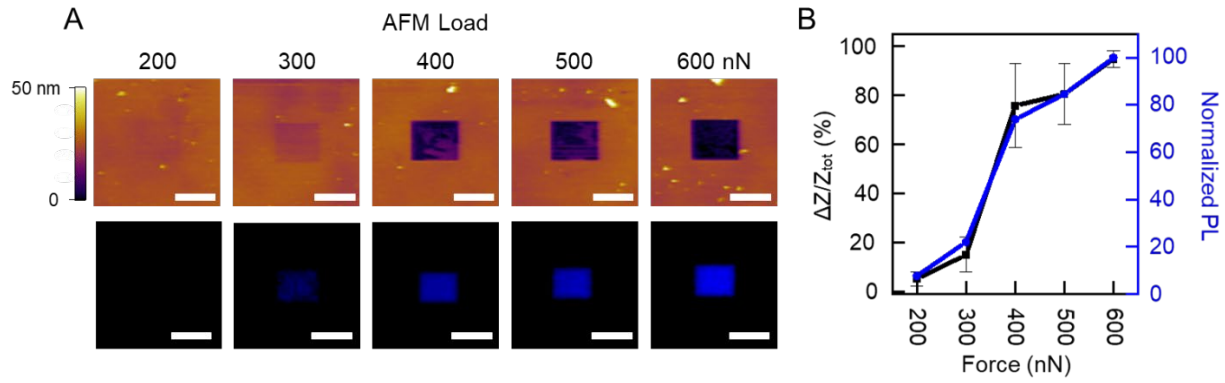

Figure 3.6. (A) Top: AFM topographic images of a PGMA brush on a Si-wafer, taken at 5 designated locations. The images were acquired in DMSO under an imaging force of 55 nN. Each image covers a 15.4 µm x 15.4 µm area with the central 5.8 µm x 4.8 µm area scanned under a high load indicated above each image. Bottom: fluorescence microscopy images acquired at the same areas as those above. Lateral scale bars are 5.0 µm. **(B)** The right plot shows the fluorescence intensities, normalized with respect to the 600 nN square's fluorescence (blue, normalized PL), and relative height difference (black) as a function of load.

3.3.3 Production of Complex Patterns by Design.

To further test the spatial-selectivity and density control, we designed and produced a gradient feature. A rectangular greyscale gradient feature was first designed and saved in bitmap format (Figure 3.7A). After imaging the polymer brush in DMSO at low force, a relatively flat region was selected. Then the design from Figure 3.7A was input to the AFM imaging software using the program's bitmap lithography tool and applied to the selected region. The location and size of the design were adjusted to the configuration shown in Figure 3.7B. Then the grey scale in the design (dark to bright) was assigned to specific loads by defining the minimum and maximum value, e.g. black = 0.1, and white = 1.0 μN, with a linear relationship for the grey scale in between. Finally, the design was transcribed onto the PGMA brush at the assigned load line-by-line. The result was imaged in contact mode in DMSO under a low force of 66 nN, as shown in Figure 3.7C. The gradient feature covers the central 4.8 μm x 2.8 μm area, requiring 351 lines and 8 minutes to produce. Comparing Figures 3.7A and 3.7C, the design was "transferred" with high fidelity in both geometry and gradient contrast. A cursor profile shown in Figure 3.7D indicates that the height is continuously decreasing along the x-direction during the first 2.7 μm, with the height gradient of $\Delta Z/\Delta X$ = 6.1 nm / 2.7 μm = 2.26 nm/μm. Beyond 2.7 μm, the topography plateaued due to activation of all the mechanophores. The gradient can be controlled by varying the load assigned to the contrast or changing the x-range, demonstrating the feasibility and high degree of control in spatial selectivity and activation density.

The results shown in Figures 3.7 also facilitates the understanding of AFM based MA activation mechanism, e.g., pulling, normal load, or lateral shearing under high normal force. In Figure 3.7, for example, a series of lines were produced under increasing load. The tip remained

in contact with the polymers throughout the scan. Thus, only normal force and shearing were present. The only pulling force experienced is the end contact point at the corner of the image, yet, activation was observed following the trajectory of each line, and the degree of activation is in good accordance of the normal load. In addition, we also applied normal force without lateral movement. Within the force range used in this work, no detectable activation was observed. Therefore, we infer that shearing under high load between AFM apex and molecules under contact is primarily responsible for mechano-activation.

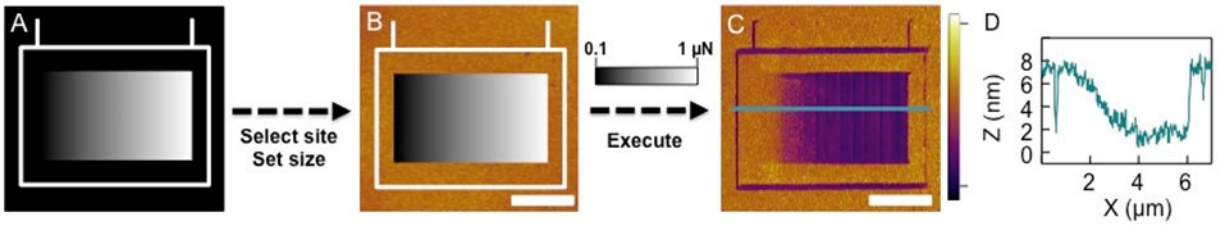

Figure 3.7. (A) The designed gradient image file shown in grey scale. (B) A 7.0 μm x 6.6 μm AFM topographic image of a PGMA brush overlaid with the physical location and dimension of A prior to activation. AFM lithography was executed, applying the corresponding forces following the designed gradient pattern. (C) AFM topographic image of the same area as B post lithography. The polymer brush height was 10.6 ± 0.6 nm above the Si wafer surface, passivated by 1.4±0.2 nm thick oligomeric ethylene oxide. Lateral scale bar and vertical range are 2.0 μm, and 0-14 nm, respectively. (D) Height profile as indicated by the horizontal line in C.

A more complex design (Figure 3.8) was also tested. Following the same method as that in Figure 3.7 and defining the force range as 50 nN – 900 nN, the design was successfully replicated within the 6.15 μm x 6.15 μm area with two successive scans.

The intricate geometry, such as the blades of the spiral, and the central circle, were accurately produced. Even small features were replicated with high fidelity, such as the points of the blades (55 nm). Note that all the non-connected domains, such as the blades and the central circle, were also transcribed with high fidelity without any traces of dragging. The three different shades on the blades were also faithfully "translated" by assigning the shades to different forces to be applied during the scan. The corresponding fluorescence image was shown in Figure 3.8B, where the intensity map is highly consistent with the location and local abundance of anthracene termini. The robustness of high spatial selectivity was verified by production of a hierarchical feature (not pictured). Results from Figures 3.7 and 3.8 demonstrate that combining AFM with the mechanochemical reaction led to high fidelity and spatial accuracy. Such a high degree of control and selectivity paves the way for a broad range of applications, including composite material engineering, molecular control over the chemical and physical properties of surfaces, and fabrication of stress-sensitive nanodevices.[1, 2, 43, 44]

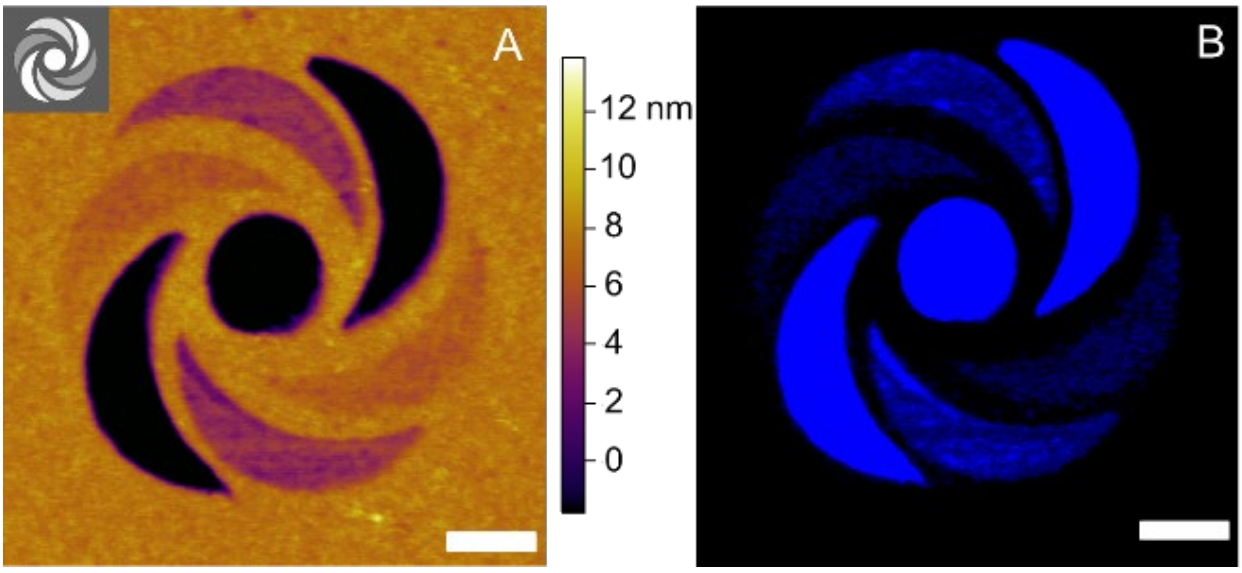

Figure 3.8. (A) AFM topographic image taken after scanning a complex grey scale image (inset) onto 12.1 ± 1.3 nm thick PGMA brush immobilized by MA mechanophores on a Si-wafer, passivated by 1.4±0.2 nm thick oligomeric ethylene oxide. (B) Fluorescence microscopy image of the same region as A, under 360 nm excitation and collected from 410-430 nm. All scale bars are 1.0 μm.

The high degree of control was applied to create a complex, multishade feature by design via the regio-selective and density-controlled activation of the mechanophore groups. Shown in Figure 3.9 inset is the bitmap image of the UC Davis Aggie logo. Following previous protocol to the gradient feature, the AFM tip scanned over the surface, applying 8.8 nN and 1.3 μN for the black and white regions, respectively. The area was reimaged at a low force, as shown in the AFM topographic image Figure 3.9A. The feature demonstrated high spatial fidelity, from left ear to the tip of the nose, the actual distance was 8.18 μm while the intended distance was 8.16 μm. Even small features, such as the pupil, nostril and inner ear were fabricated with high fidelity to the

original design, despite their miniscule sizes. The Aggie feature demonstrated multiple levels of complexity including: the multishade appearance due differing degrees of mechanophore activation and geometric complexity. This complexity is also reflected in the corresponding fluorescence microscopy image in Figure 3.9B. The feature shows bright fluorescence in regions subjected to the highest scanning force, demonstrating that activation as achieved even with the complex shape and spatial limitations. In the areas where only a portion of the mechanophore were activated (along the ridge of the nose), a faint blue fluorescence can be seen in Figure 3.9B. Based on the evidence present, a complex, multishade feature was created via the regio selective and density-controlled activation.

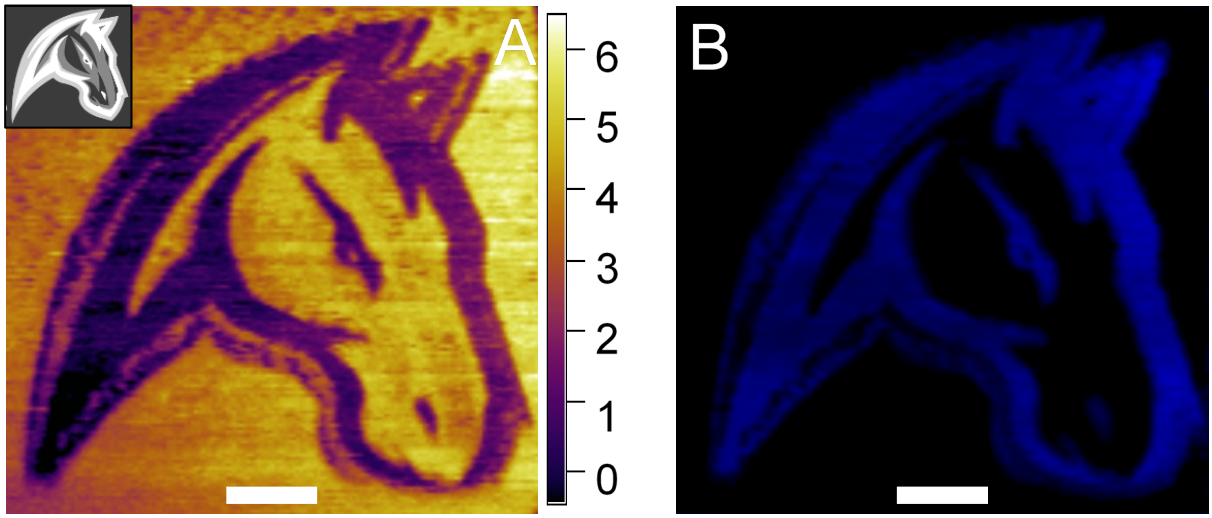

Figure 3.9. A complex, multishade mechanophore feature of UC Davis Aggie logo. (inset) A greyscale force bitmap of the UC Davis Aggie logo.[51] The force applied ranged from 8.8 nN to 1.3 μN for black to white respectively, and other important lithography parameters are included. (A) AFM topographic image of the Aggie logo multishade features. (B) Corresponding fluorescence microscopy image of the same region as A, under 360 nm excitation and collected from 410-430 nm. All scale bars are 2.0 μm.

3.3.4 Confirmation of Mechanochemical Activation Using Fluorescence Microscopy, ToF-SIMS, Optical Microscopy, and AFM Topographic Imaging

Chemical and topographical changes after mechanochemical activation of interfacial MA at micrometer scale were confirmed with fluorescence microscopy, Time of Flight-Secondary Ion Mass Spectroscopy (ToF-SIMS), optical microscopy, and AFM. Shown in Figure 3.10A, the fluorescence image was collected from 410-430 nm emission upon 360 nm excitation, which detects fluorescence from the surface bound anthracene.[1]The fluorescence signal exclusively from the fabricated region confirms that high contact force successfully translated to mechanochemical activation. ToF-SIMS (Figure 3.10B) for the CNO^- negative ion, originating from the maleimide fragment,[2] was collected to map surface distribution of the intact MA adduct on the surface after fabrication. A low concentration of maleimide moiety was detected inside the fabricated 'T' feature, whereas the intact regions showed a relatively high concentration. This result is consistent with the fluorescence measurements that showed selective mechanophore activation where high contact force was applied, which led to the loss of the maleimide fragment. The optical micrograph in Figure 3.10C shows color contrast between the fabricated region and intact region due to removal of the polymer brush. The AFM topographic image in Figure 3.10D shows a height difference after fabricating the 'T' feature with 450 nN contact force. AFM topography image shows height difference after fabricating the 'T' feature with 450 nN contact force, which further

verifies the removal of the PGMA brush.

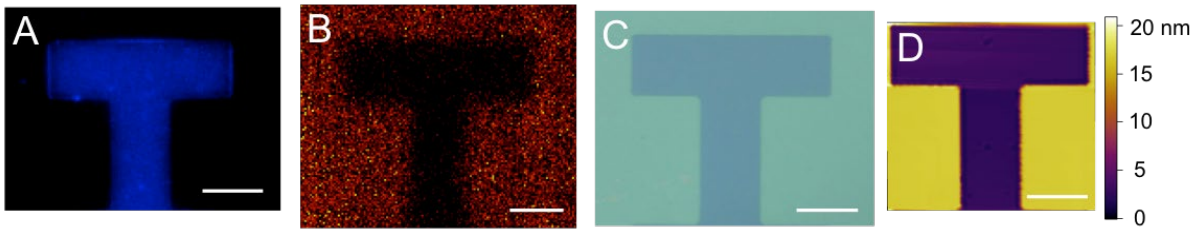

Figure 3.10. Confirmation of interfacial mechanophore activation using AFM lithography. (A) Fluorescence image of an 'T' feature fabricated. (B)ToF-SIMS image for fragment 41.99 u (CNO^-) which corresponds to the maleimide moiety of the fabricated 'T' feature. (C) Optical image of fabricated the 'T' feature. (D) AFM topographic image of fabricated 'T' feature. The scale bars are 20 μm.

3.3.5 Attempted Activation of Control Samples

To determine if PGMA removal was due to the mechanophore group, and to verify that the PGMA brush itself is stable under high force, we subjected a control sample (see Figure 3.11C) to the same 450 nN force with identical scan parameters as the mechanophore sample shown in Figure 3.5. The control sample shows no height decrease after high force application (see Figure 3.11B) when compared to the sample before high force (Figure 3.11A), indicating none of the PGMA brushes were cleaved. Upon 360 nm excitation, the control sample showed no detectable fluorescence at 410-430 nm (Figure 3.11D), further verifying that the fluorescence seen in the mechanophore sample is due to the cleavage of the maleimide-anthracene moiety.

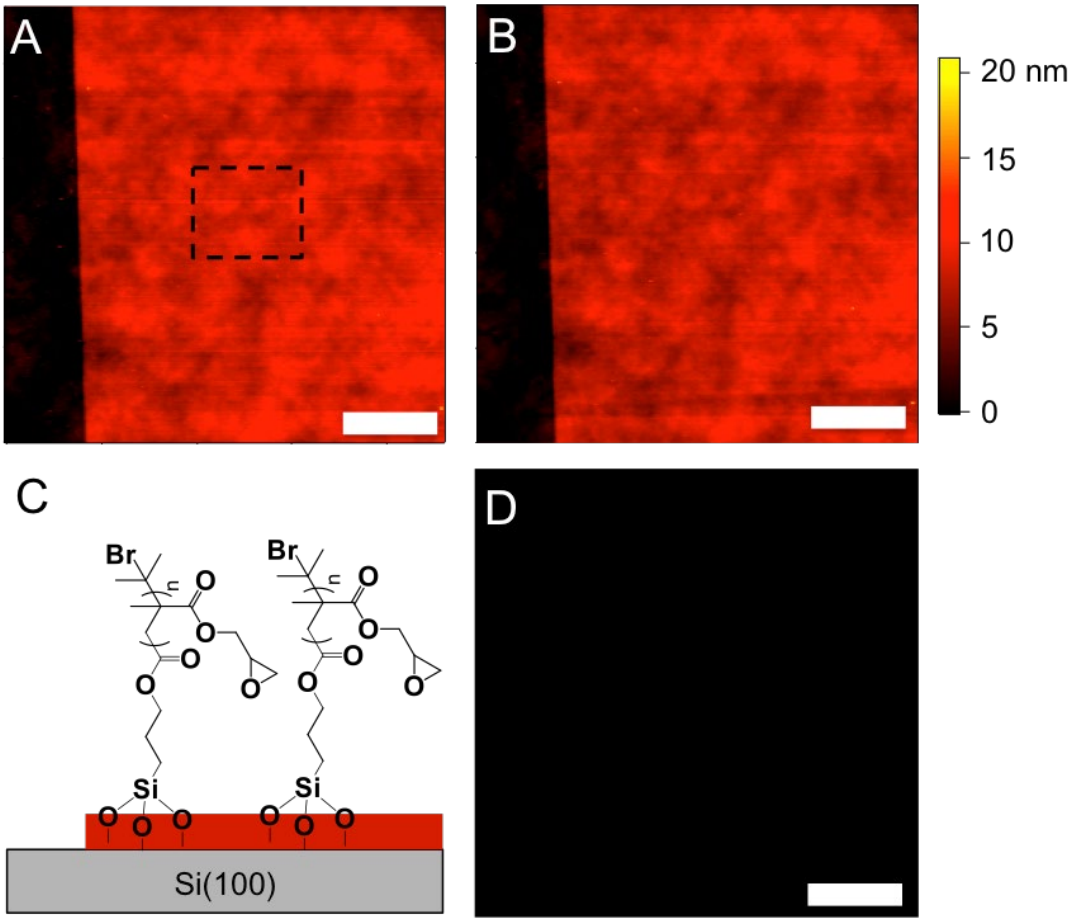

Figure 3.11. Images (A) and (B) were acquired under identical conditions as Figures 3.5A and 3.5B, respectively, except that the surface adsorbates were polymer brushes without mechanophores. (C) Schematic diagram illustrates the surface functionalities corresponding to the AFM image in B. (D) Fluorescence image of the same region as B. All scale bars are 5.0 μm.

3.3.6 Production of Hierarchical Patterns

The robustness of the spatially selective activation was further demonstrated by producing a hierarchical feature (Figure 3.12). Using the design tool included in the AFM's software (MicroAngelo macro written using Igor Pro 6.34), the hierarchical structure was

designed in two steps: first, the hollow letter ‘T’; second, periodical squares fill the space within the hollow ‘T’ feature. Upon setting the load (700 nN) and the physical dimensions, the AFM scan replicated the design in a couple of minutes. In the lateral force image shown above, the anthracene-termini region exhibited lower friction than surrounding polymer brush terminated by tert-butyl bromide, which is expected given the hydrophobic nature of the anthracene termini and the hydrophilic character of the cantilever. The grids lines of the ‘T’ feature were 83 nm wide. The inner grid rectangles measured 142 nm x 161 nm, while the size of the overall feature is 2.2 μm x 2.8 μm. This magnitude of difference in size indicates that this method is capable of producing small features without sacrificing the fidelity of the larger scale feature, verifying its robustness. The fidelity of the feature produced coupled with the magnitude in difference in feature size verifies the robustness of the high activation of the MA mechanophore using AFM technology.

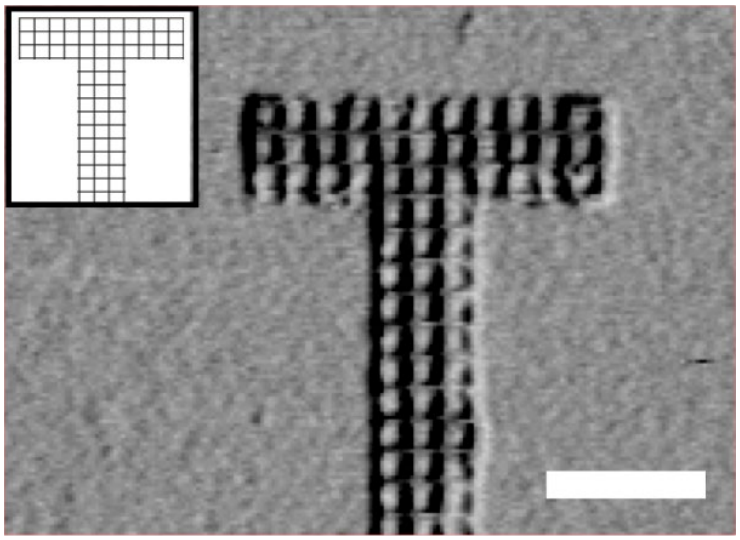

Figure 3.12. Example of hierarchical feature produced using AFM. The lateral AFM image of the hierarchical feature is shown. (Inset) An ‘T’ feature patterned with a square grid, custom designed. The scale bar is 1.0 μm.

3.4 Conclusions

We demonstrate the activation of a surface immobilized maleimide-anthracene mechanophore with a PGMA brush using AFM. Taking advantage of the accurate force control in AFM, the contact force between the probe apex and the substrate-bound mechanophore was tuned for either imaging or activation. The retro [4+2] cycloaddition upon activation of the MA mechanophore was verified by the topographic changes revealed by in situ AFM imaging and fluorescence microscopy, where surface-bound anthracene exhibits a characteristic emission at 410-430 nm. This new means to activate mechanophores has the intrinsic advantages of (a) a wide range of force control and tunability; (b) high spatial precision which enables nanolithography with a focus on utilizing AFM nanolithography; and (c) in situ activation and characterization. The high spatial resolution of AFM enabled nanolithography of complex structures with high spatial accuracy and selectivity. Unlike prior 2D nanolithography where the contrast is mostly binary, we demonstrate that multi-level contrast in the original design, including gradient features and hierarchical micro- and nano-structures, could be faithfully translated via spatially controlled surface chemistry. The concept and methodology developed in this work is of generic importance for other mechanophore containing materials. Work is in progress to construct 3D nanostructures by combing this approach with subsequent surface reactions, which will enable 3D nanoprinting. Future applications include production of coatings and composite materials that require nanopatterning or texture control, as well as nanodevices and sensors for measuring mechanical stress and damages *in situ.*

3.5 References

1. Li, J.; Nagamani, C.; Moore, J. S., Polymer Mechanochemistry: From Destructive to Productive. *Accounts Chem Res* **2015,** *48* (8), 2181-2190.

2. Black, A. L.; Lenhardt, J. M.; Craig, S. L., From molecular mechanochemistry to stress-responsive materials. *J Mater Chem* **2011,** *21* (6), 1655-1663.

3. Brantley, J. N.; Wiggins, K. M.; Bielawski, C. W., Polymer mechanochemistry: the design and study of mechanophores. *Polym. Int.* **2013,** *62* (1), 2-12.

4. Allison, D. P.; Hinterdorfer, P.; Han, W. H., Biomolecular force measurements and the atomic force microscope. *Curr Opin Biotech* **2002,** *13* (1), 47-51.

5. Robb, M. J.; Kim, T. A.; Halmes, A. J.; White, S. R.; Sottos, N. R.; Moore, J. S., Regioisomer-Specific Mechanochromism of Naphthopyran in Polymeric Materials. *J. Am. Chem. Soc.* **2016,** *138* (38), 12328-12331.

6. Davis, D. A.; Hamilton, A.; Yang, J.; Cremar, L. D.; Van Gough, D.; Potisek, S. L.; Ong, M. T.; Braun, P. V.; Martinez, T. J.; White, S. R.; Moore, J. S.; Sottos, N. R., Force-induced activation of covalent bonds in mechanoresponsive polymeric materials. *Nature* **2009,** *459* (7243), 68-72.

7. Gossweiler, G. R.; Hewage, G. B.; Soriano, G.; Wang, Q.; Welshofer, G. W.; Zhao, X.; Craig, S. L., Mechanochemical activation of covalent bonds in polymers with full and repeatable macroscopic shape recovery. *Acs Macro Lett* **2014,** *3* (3), 216-219.

8. Piermattei, A.; Karthikeyan, S.; Sijbesma, R. P., Activating catalysts with mechanical force. *Nat. Chem.* **2009,** *1* (2), 133-7.

9. Diesendruck, C. E.; Peterson, G. I.; Kulik, H. J.; Kaitz, J. A.; Mar, B. D.; May, P. A.; White, S. R.; Martínez, T. J.; Boydston, A. J.; Moore, J. S., Mechanically triggered heterolytic unzipping

of a low-ceiling-temperature polymer. *Nat Chem* **2014,** *6* (7), 623-628.

10. Larsen, M. B.; Boydston, A. J., "Flex-activated" mechanophores: using polymer mechanochemistry to direct bond bending activation. *J. Am. Chem. Soc.* **2013,** *135* (22), 8189-92.

11. Chen, Z.; Mercer, J. A.; Zhu, X.; Romaniuk, J. A.; Pfattner, R.; Cegelski, L.; Martinez, T. J.; Burns, N. Z.; Xia, Y., Mechanochemical unzipping of insulating polyladderene to semiconducting polyacetylene. *Science* **2017,** *357* (6350), 475-479.

12. Li, J.; Shiraki, T.; Hu, B.; Wright, R. A.; Zhao, B.; Moore, J. S., Mechanophore activation at heterointerfaces. *J Am Chem Soc* **2014,** *136* (45), 15925-8.

13. Imato, K.; Natterodt, J. C.; Sapkota, J.; Goseki, R.; Weder, C.; Takahara, A.; Otsuka, H., Dynamic covalent diarylbibenzofuranone-modified nanocellulose: mechanochromic behaviour and application in self-healing polymer composites. *Polym. Chem.* **2017,** *8* (13), 2115-2122.

14. Woodcock, J. W.; Beams, R.; Davis, C. S.; Chen, N.; Stranick, S. J.; Shah, D. U.; Vollrath, F.; Gilman, J. W., Observation of Interfacial Damage in a Silk-Epoxy Composite, Using a Simple Mechanoresponsive Fluorescent Probe. *Adv Mater Interfaces* **2017,** *4* (10).

15. Beiermann, B. A.; Kramer, S. L. B.; May, P. A.; Moore, J. S.; White, S. R.; Sottos, N. R., The Effect of Polymer Chain Alignment and Relaxation on Force-Induced Chemical Reactions in an Elastomer. *Adv. Funct. Mater.* **2014,** *24* (11), 1529-1537.

16. Kim, T. A.; Beiermann, B. A.; White, S. R.; Sottos, N. R., Effect of Mechanical Stress on Spiropyran-Merocyanine Reaction Kinetics in a Thermoplastic Polymer. *Acs Macro Lett* **2016,** *5* (12), 1312-1316.

17. Potisek, S. L.; Davis, D. A.; Sottos, N. R.; White, S. R.; Moore, J. S., Mechanophore-linked addition polymers. *J. Am. Chem. Soc.* **2007,** *129* (45), 13808-9.

18. May, P. A.; Munaretto, N. F.; Hamoy, M. B.; Robb, M. J.; Moore, J. S., Is Molecular Weight or Degree of Polymerization a Better Descriptor of Ultrasound-Induced Mechanochemical Transduction? *ACS Macro Lett.* **2016,** *5* (2), 177-180.

19. Berkowski, K. L.; Potisek, S. L.; Hickenboth, C. R.; Moore, J. S., Ultrasound-induced site-specific cleavage of azo-functionalized poly (ethylene glycol). *Macromolecules* **2005,** *38* (22), 8975-8978.

20. Gossweiler, G. R.; Kouznetsova, T. B.; Craig, S. L., Force-rate characterization of two spiropyran-based molecular force probes. *J. Am. Chem. Soc.* **2015,** *137* (19), 6148-51.

21. Kersey, F. R.; Yount, W. C.; Craig, S. L., Single-molecule force spectroscopy of bimolecular reactions: system homology in the mechanical activation of ligand substitution reactions. *J. Am. Chem. Soc.* **2006,** *128* (12), 3886-3887.

22. Wang, J. P.; Kouznetsova, T. B.; Niu, Z. B.; Ong, M. T.; Klukovich, H.; Rheingold, A. L.; Martinez, T. J.; Craig, S. L., Inducing and quantifying forbidden reactivity with single-molecule polymer mechanochemistry. *Nat Chem* **2015,** *7* (4), 323-327.

23. Zou, S.; Schonherr, H.; Vancso, G. J., Stretching and rupturing individual supramolecular polymer chains by AFM. *Angew Chem Int Edit* **2005,** *44* (6), 956-959.

24. Klukovich, H. M.; Kouznetsova, T. B.; Kean, Z. S.; Lenhardt, J. M.; Craig, S. L., A backbone lever-arm effect enhances polymer mechanochemistry. *Nat Chem* **2013,** *5* (2), 110-114.

25. Sung, J.; Robb, M. J.; White, S. R.; Moore, J. S.; Sottos, N. R., Interfacial Mechanophore Activation Using Laser-Induced Stress Waves. *J. Am. Chem. Soc.* **2018,** *140* (15), 5000-5003.

26. Liu, M.; Amro, N. A.; Liu, G.-y., Nanografting for surface physical chemistry. *Annu. Rev. Phys. Chem.* **2008,** *59*, 367-386.

27. Kaholek, M.; Lee, W. K.; LaMattina, B.; Caster, K. C.; Zauscher, S., Fabrication of stimulus-responsive nanopatterned polymer brushes by scanning-probe lithography. *Nano Lett* **2004,** *4* (2), 373-376.

28. Carpick, R. W.; Salmeron, M., Scratching the surface: Fundamental investigations of tribology with atomic force microscopy. *Chem Rev* **1997,** *97* (4), 1163-1194.

29. Drake, B.; Prater, C. B.; Weisenhorn, A. L.; Gould, S. A. C.; Albrecht, T. R.; Quate, C. F.; Cannell, D. S.; Hansma, H. G.; Hansma, P. K., Imaging Crystals, Polymers, and Processes in Water with the Atomic Force Microscope. *Science* **1989,** *243* (4898), 1586-1589.

30. Vezenov, D. V.; Noy, A.; Ashby, P., Chemical force microscopy: probing chemical origin of interfacial forces and adhesion. *J Adhes Sci Technol* **2005,** *19* (3-5), 313-364.

31. Garcia-Manyes, S.; Sanz, F., Nanomechanics of lipid bilayers by force spectroscopy with AFM: A perspective. *Bba-Biomembranes* **2010,** *1798* (4), 741-749.

32. Fisher, T. E.; Oberhauser, A. F.; Carrion-Vazquez, M.; Marszalek, P. E.; Fernandez, J. M., The study of protein mechanics with the atomic force microscope. *Trends Biochem Sci* **1999,** *24* (10), 379-384.

33. Ludwig, M.; Rief, M.; Schmidt, L.; Li, H.; Oesterhelt, F.; Gautel, M.; Gaub, H. E., AFM, a tool for single-molecule experiments. *Appl Phys a-Mater* **1999,** *68* (2), 173-176.

34. Asif, S. A. S.; Wahl, K. J.; Colton, R. J.; Warren, O. L., Quantitative imaging of nanoscale mechanical properties using hybrid nanoindentation and force modulation (vol 90, pg 1192, 2001). *J Appl Phys* **2001,** *90* (11), 5838-5838.

35. Liu, J. F.; Cruchon-Dupeyrat, S.; Garno, J. C.; Frommer, J.; Liu, G. Y., Three-dimensional nanostructure construction via nanografting: Positive and negative pattern transfer. *Nano Lett*

2002, *2* (9), 937-940.

36. Xu, S.; Laibinis, P. E.; Liu, G. Y., Accelerating the kinetics of thiol self-assembly on gold - A spatial confinement effect. *J Am Chem Soc* **1998,** *120* (36), 9356-9361.

37. Liu, M.; Amro, N. A.; Liu, G. Y., Nanografting for surface physical chemistry. *Annu Rev Phys Chem* **2008,** *59*, 367-386.

38. Liu, G. Y.; Amro, N. A., Positioning protein molecules on surfaces: A nanoengineering approach to supramolecular chemistry. *P Natl Acad Sci USA* **2002,** *99* (8), 5165-5170.

39. Xu, S.; Liu, G. Y., Nanometer-scale fabrication by simultaneous nanoshaving and molecular self-assembly. *Langmuir* **1997,** *13* (2), 127-129.

40. Piner, R. D.; Zhu, J.; Xu, F.; Hong, S. H.; Mirkin, C. A., "Dip-pen" nanolithography. *Science* **1999,** *283* (5402), 661-663.

41. Maoz, R.; Frydman, E.; Cohen, S. R.; Sagiv, J., "Constructive nanolithography": Inert monolayers as patternable templates for in-situ nanofabrication of metal-semiconductor-organic surface structures - A generic approach. *Adv Mater* **2000,** *12* (10), 725-+.

42. Zhou, X. C.; Liu, Z. L.; Xie, Z.; Liu, X. Q.; Zheng, Z. J., High-Resolution, Large-Area, Serial Fabrication of 3D Polymer Brush Structures by Parallel Dip-Pen Nanodisplacement Lithography. *Small* **2012,** *8* (23), 3568-3572.

43. Frazier, W. E., Metal Additive Manufacturing: A Review. *J Mater Eng Perform* **2014,** *23* (6), 1917-1928.

44. Ivanova, O.; Williams, C.; Campbell, T., Additive manufacturing (AM) and nanotechnology: promises and challenges. *Rapid Prototyping J* **2013,** *19* (5), 353-364.

45. Nofen, E. M.; Dasgupta, A.; Zimmer, N.; Gunckel, R.; Koo, B.; Chattopadhyay, A.; Dai, L.

L., Universal Stress-Sensing Dimeric Anthracene-Based Mechanophore Particle Fillers Incorporated into Polyurethane Thermoset Matrices. *Polym Eng Sci* **2017,** *57* (8), 901-909.

46. Chen, J.-K.; Chang, C.-J., Fabrications and applications of stimulus-responsive polymer films and patterns on surfaces: a review. *Materials* **2014,** *7* (2), 805-875.

47. Song, Y.; Ye, G.; Lu, Y.; Chen, J.; Wang, J.; Matyjaszewski, K., Surface-Initiated ARGET ATRP of Poly(Glycidyl Methacrylate) from Carbon Nanotubes via Bioinspired Catechol Chemistry for Efficient Adsorption of Uranium Ions. *ACS Macro Letters* **2016,** *5* (3), 382-386.

48. Li, D.; Sheng, X.; Zhao, B., Environmentally responsive "hairy" nanoparticles: Mixed homopolymer brushes on silica nanoparticles synthesized by living radical polymerization techniques. *J. Am. Chem. Soc.* **2005,** *127* (17), 6248-6256.

49. Li, J.; Hu, B.; Yang, K.; Zhao, B.; Moore, J. S., Effect of Polymer Grafting Density on Mechanophore Activation at Heterointerfaces. *Acs Macro Lett* **2016,** *5* (7), 819-822.

50. Li, H.; Göstl, R.; Delgove, M.; Sweeck, J.; Zhang, Q.; Sijbesma, R. P.; Heuts, J. P. A., Promoting Mechanochemistry of Covalent Bonds by Noncovalent Micellar Aggregation. *ACS Macro Lett.* **2016,** *5* (9), 995-998.

51. Church, D. C.; Peterson, G. I.; Boydston, A. J., Comparison of Mechanochemical Chain Scission Rates for Linear versus Three-Arm Star Polymers in Strong Acoustic Fields. *Acs Macro Lett* **2014,** *3* (7), 648-651.

52. Ulman, A., Formation and structure of self-assembled monolayers. *Chem Rev* **1996,** *96* (4), 1533-1554.

53. Liu, G. Y.; Xu, S.; Qian, Y. L., Nanofabrication of self-assembled monolayers using scanning probe lithography. *Accounts Chem Res* **2000,** *33* (7), 457-466.

54. Drexler, C. I.; Moore, K. B.; Causey, C. P.; Mullen, T. J., Atomic Force Microscopy Characterization and Lithography of Cu-Ligated Mercaptoalkanoic Acid "Molecular Ruler" Multilayers. *Langmuir* **2014,** *30* (25), 7447-7455.

55. Hirtz, M.; Brinks, M. K.; Miele, S.; Studer, A.; Fuchs, H.; Chi, L. F., Structured Polymer Brushes by AFM Lithography. *Small* **2009,** *5* (8), 919-923.

56. Helt, J. M.; Batteas, J. D., Implications of the contact radius to line step (CRLS) ratio in AFM for nanotribology measurements. *Langmuir* **2006,** *22* (14), 6130-6141.

57. Milner, S., Polymer brushes. *Science* **1991,** *251* (4996), 905-914.

58. Chen, T.; Amin, I.; Jordan, R., Patterned polymer brushes. *Chem Soc Rev* **2012,** *41* (8), 3280-3296.

59. Zhou, T.; Qi, H.; Han, L.; Barbash, D.; Li, C. Y., Towards controlled polymer brushes via a self-assembly-assisted-grafting-to approach. *Nat Commun* **2016,** *7*.

CHAPTER 4

Producing Organizational Chirality by Design via Scanning Probe Nanolithography

4.1 Introduction

Surface chirality is an area of growing interest, as there are many potential applications such as chiral sensors, enantiomeric separation as well as enantioselective heterogeneous catalysis.[5-6] In addition to the well-known molecular chirality, surface chirality can also arise from achiral molecules, as certain absorbed conformations induce chirality.[7-8] A less studied form of surface induced chirality is organizational chirality, which solely arises from the arrangement of the molecules on the surface.[9] Current means to produce organizational chirality primarily relies on self-assembly, from simple and small organic molecules[9-11] to large aromatic ones.[12-13] The resulting chiral structures are restricted to those driven by the thermodynamics of absorption.

In order to go beyond this restriction and achieve organizational chirality by design, we turn to combining atomic force microscopy (AFM) and surface chemistry. Taking the full advantage of the high spatial precision of AFM in performing nanolithography and creating simple chiral geometry, [14-15] various functionalities and complex chiral designs can be achieved, e.g., by utilizing designed surface reactions such as thiol adsorption on precious metals, and retro-Diels−Alder reactions of maleimide anthracene mechanophores. Various chiral structures have been designed and produced with nanometer precision, from simple chiral spirals to arrays of chiral nanofeatures to hierarchical chiral structures within which both individual features and overall layout were chiral. In addition to nanolithography, AFM also provides a powerful and high-resolution readout of the chiral features produced.[16] The concept and methodology reported here

enable a new and generic means to perform organizational chiral chemistry, with the intrinsic advantages of chiral structure by design. The results open new and promising applications including organizational chiral sensors, 3D chiral nanoprinting, enantiomeric separation, and enantiomeric heterogeneous catalysis.

Data for Figures 4.1 and 4.2 was contributed by Dr. Logan Swartz, data for Figures 4.6 and 4.7 was contributed by Minyuan Wang. All other data (Figures 4.3-4.5) was collected by me.

4.2 Experimental

4.2.1 Materials.

Chemical reagents were used without further purification unless specifically stated. Ethanol (200 proof) was purchased from VWR (Radnor, PA). Gold slugs (99.999% pure) were purchased from Alfa Aesar (Haverhill, MA). Mica sheets were purchased from S & J Trading Inc. (Glen Oaks, NY). Deionized and ultrapure water with a resistivity of 18.2 MΩ · cm at 25 °C was generated by a Milli-Q water system (EMD Millipore, Billerica, MA). Dimethyl sulfoxide (99.9%) was obtained from Sigma Aldrich (St. Louis, MO). 1-Octanethiol (≥98.5%) and 1-octadecanethiol (98%) were purchase from Sigma Aldrich (St. Louis, MO). [Jay, can you put your reagents for your samples here?] Silicon cantilevers (AC-240, spring constant, k = 1.7 N/m) were procured from Olympus America (Central Valley, PA). Silicon nitride cantilevers (MSNL-10, k = 0.6 N/m) were procured from Bruker Nano (Camarillo, CA).

4.2.2 Preparation of Self-Assembled Monolayers on Surfaces.

Ultraflat gold thin films were prepared based on previously published methods.[17] Self-assembled monolayers were formed by soaking the gold thin films in 1.0 mM of C_8 thiol in ethanol

solutions. The substrates remained in these solutions until used for nanografting to ensure high coverage and minimal contamination.

Maleimide-anthracene mechanophore samples were prepared according to previously published methods.[16, 18]

4.2.3 High-Resolution AFM Imaging and Nanolithography.

A deflection type AFM (MFP-3D, Oxford Instrument, Santa Barbara, CA) was used for nanolithography and high-resolution imaging. Data acquisition was carried out using MFP-3D software developed based on the Igor Pro 6.12 platform. The basic protocol of nanografting has been reported previously.[1, 17] Briefly, SAMs were first imaged using a silicon nitride cantilever with low force in contact mode in a solution of C_{18} in ethanol. After selecting a desired region, nanolithography was done by applying a high force to the AFM tip (indicated for each figure) and tracing the desired pattern. After the lithography scans, the areas were scanned again with a low force to visualize the lithography results. Data analysis was done using the MFP-3D's Igor Pro 6.12 software. The results are shown in Figures 4.1 and 4.2. Imaging and nanofabrication conditions varied and are provided for each experiment.

For the maleimide anthracene mechanophore AFM images shown in Figures 4.3-4.7, a protocol similar to previously published methods was used.[16] The silicon cantilevers were used in contact mode for imaging and nanolithography in DMSO. Imaging and nanofabrication conditions varied and are provided for each experiment.

4.3 Results and Discussion

4.3.1 Production of Organizational Chiral Structures by Design Using Nanolithography and Self-assembled Surface Chemistry.

To demonstrate that AFM based nanolithography enables production of organizational chiral structures, we first designed a pair of simple Archimedean spirals, as shown in Figure 4.1A. The spiral on the left rotates counterclockwise outward from the center, thus is denoted as the "S" chirality. Its mirror image on the right thus exhibits the "R" chirality. The chirality is further verified by the lack of centers of symmetry in each feature, i.e., neither spiral can be superimposed with its mirror image within the plane.

Translating the design into true chemical features requires the selection of surface chemistry (i.e., for canvas and active components); scaling the design to actual size and setting nanolithography conditions; and finally performing the AFM based nanolithography accordingly. A 1-octanethiol (abbreviated as C_8) layer on an ultraflat Au thin film,[17] known as a self-assembled monolayer (SAM), was used as the matrix or canvas, and 1-octadecanethiol (abbreviated as C_{18}) molecules were used the active component for the spirals. The C_8 SAM was first imaged via AFM in a solution of 0.02 mM C_{18} in ethanol under a low force of 6.7 nN, from which the nanolithography site was chosen. The design (shown in Figure 4.1A) could easily be produced using any design software including MS-PowerPoint and saved in png format, which was then read and displayed directly by our AFM data acquisition program. The upload spirals were then moved to the designated location, and changed into the desired size, in this case by the Eqs. 1 and 2:

$$r\ (nm) = 18.00\ (nm) \times \theta \quad (1)$$

$$r\ (nm) = -18.00\ (nm) \times \theta \quad (2)$$

for S and R spirals, respectively. Here, r is the distance between the point to center and θ is the angle counter-clockwise with respect to the horizontal axis, and ranged from 0 to 6.5 π. Setting the spiral line contrast as the applied force (218 nN), the AFM tip was then scanned at 1.0 μm/s at this high load following the trajectory of the spirals. The high force shaved the C_8 from the Au surface, and the void was then immediately filled by the C_{18} molecules in the imaging medium. After nanografting, the 1.5 μm x 0.75 μm area was imaged at a much-reduced force of 6.7 nN. As shown in Figure 4.1B, the two spirals were faithfully produced following the following trajectory of Eqs. 3 and 4:

$$r\ (nm) = 18.10\ (nm) \times \theta \quad (3)$$

$$r\ (nm) = -17.82\ (nm) \times \theta \quad (4)$$

where θ ranged from 0 to 6.5 π. The height of C_{18} was measured as 0.7 ± 0.2 nm above the C_8 SAM in the surrounding, consistent with the known SAM structure with the close packed alkanethiol molecules whose chains are tilt of 30° from the surface normal.[19-21] The S-spiral has 3 rotations, with the linewidth (defined as full-width at half-maximum, FWHM) measured to be 24.9 ± 1.5 nm, separated by 104.2 ± 3.8 nm from its nearest-neighbors. Although alkanethiols are achiral molecules, both C_{18} spirals are considered organizational chiral structures based on the definition of organizational chirality.[5]

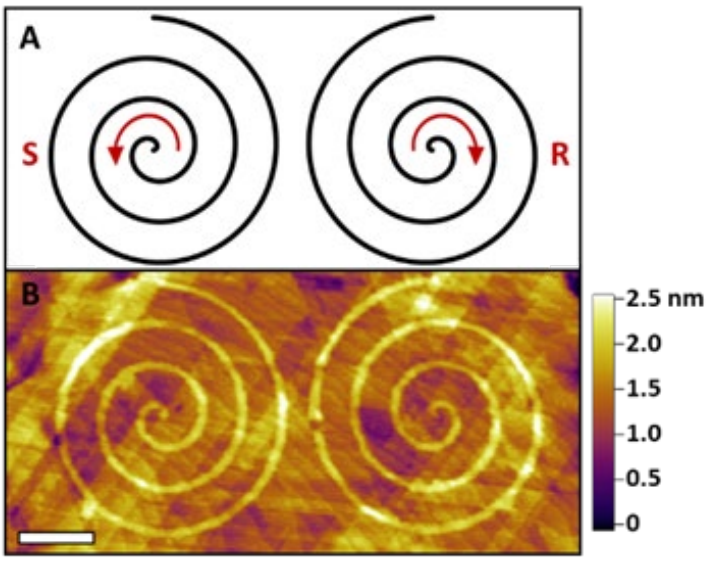

Figure 4.1. (A) The design of a pair of S and R spirals. (B) AFM topographic image (1.5 µm x 0.75 µm) of the pair of chiral structures produced following A. Image was acquired in a 0.02 mM C_{18} solution under a force of 6.7 nN and a scanning speed of 3.76 µm/s. Lateral scale bar is 0.2 µm.

For AFM instruments without the capability of using polar coordinate or uploading graphic designs, one could easily produce chiral features by defining the specific values in the X and Y scanning directions. Using Archimedean spirals as an example, the XY positions of the spiral follow simple parametric equations:

$$X = C_1\,(nm) \times \theta \times (cos(C_2\theta)) \tag{5}$$

$$Y = D_1\,(nm) \times \theta \times (sin(D_2\theta)) \tag{6}$$

Where the X and Y represent the coordinates of the designed structure; C_1, C_2, D_1 and D_2 are coefficients defining the chirality (e.g., positive values yield S-chirality), symmetry (e.g., equal in X and Y dimension or not), and detailed geometry of the spirals (e.g., density of rotations); and

the range of θ determines the overall size.

A specific design and feature are shown in Figure 4.2, where an Archimedean S-spiral can be represented and quantified using Eqs. 7 and 8:

$$X = \frac{1}{10}\ (nm) \times \theta \times \left(cos\left(\frac{\theta}{10}\right)\right) \quad (7)$$

$$Y = \frac{1}{10}\ (nm) \times \theta \times \left(sin\left(\frac{\theta}{10}\right)\right) \quad (8)$$

Where the variable θ ranged from 0 to 318.0 π with increments of 0.318 π. Setting the shaving force to 218 nN, both equations were entered into the AFM scanning commands. During the scan at 1.0 μm/s, the spiral paths were traced under 218 nN, according to XY positions defined by Equations 7 and 8. Again, nanografting took place, where the C_8 was replaced by the C_{18} molecules in the solution of 0.02 mM C_{18} in ethanol above, at the locations defined by Equations 7 and 8. The resulting feature is revealed in Figure 4.2B, where the S-spiral has 16 rotations, with linewidth equal to 23.5 ± 0.0 nm, separated by 83.9 ± 2.9 nm from its nearest neighbors. The spiral was 0.9 ± 0.1 nm above its surrounding C_8 SAM, which is consistent with the expected height difference of between the C_{18} and C_8 SAMs.[22]

Compared with prior approaches of producing organizational chiral structures, our method allows production of organizational chiral structures by design instead of being restricted to simple structures dictated by thermodynamics. The spatial precision of AFM enables nanometer resolution in both production and imaging. The organizational chirality, feature geometry, and overall feature size follow researchers' design faithfully. Combining with the recent advances in SAM chemistry,[18, 23-26] this approach enables accommodating a wide range of material and functionality. Example head-groups include thiols,[17] dithiols,[27] disulfides,[28] and silane

chemistries,[29] with terminal groups of COOH, CHO, NH_2, biotin etc.[22, 26]

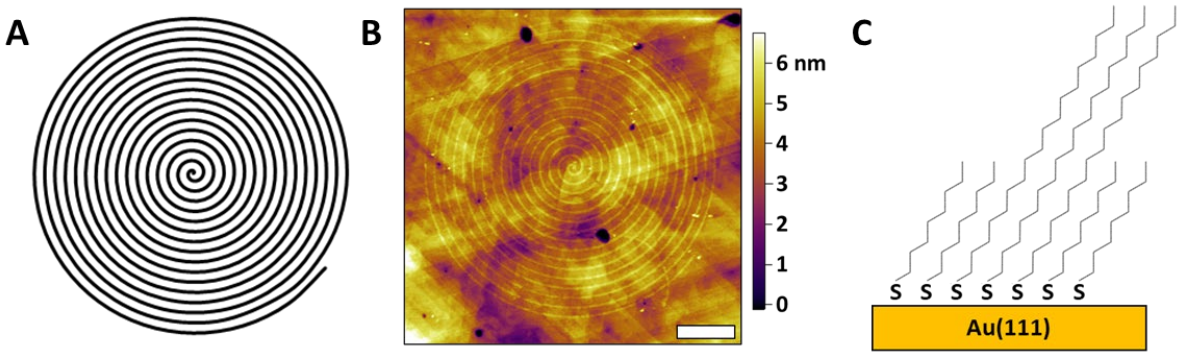

Figure 4.2. (A) An S-spiral defined by the parametric equations (7) and (8). (B) A 3.0 µm x 3.0 µm AFM topographic image containing the S-spiral of C_{18} inlaid in a C_8 SAM. AFM image was acquired in an ethanol solution containing 0.02 mM C_{18}, under a force of 6.7 nN and at a speed of 7.52 µm/s. Lateral scale bar is 0.5 µm. (C) Schematic diagram of nanografted C_{18} inlaid in the C_8 SAM revealing the adsorption conformation of the alkanethiols.

4.3.2 Production of Organizational Chiral Structures by Design Using Nanolithography and Mechanochemistry.

Expanding our designs beyond simple Archimedean spirals, a bladed fan feature was selected, which also exhibits organizational chirality. Figure 4.3A illustrates how a R-bladed fan design is generated. Each of the 'blades' is produced by the overlapping region of the two equal sized circles (blue and pink). The diameter of the circles, **D**, as well as the separation between their centers, **d,** determine the overall size and geometry of each 'blade'. Neighboring 'blades' are

rotated 60° with respect to each other, with a shared side, and a shared point, thus completing this 6-bladed fan feature.

Utilizing mechanochemistry[30] of an interfacial maleimide anthracene mechanophore system,[31] we have produced the 6-bladed fan consisting of anthracene-termini on Si-wafers, as shown in Figure 4.3. Following procedures previously reported,[16] a siloxane SAM was first produced on Si(100) surfaces. Each covalently bound molecule contains a maleimide-anthracene mechanophore and is terminated by a poly(glycidylmethacrylate) (PGMA) tail. This thin film was imaged via AFM in a dimethyl sulfoxide (DMSO) under a low force of 18 nN, to enable selection of sites for nanofabrication. The design in Figure 4.3A was exported as a bitmap image and directly uploaded into our AFM data acquisition software for displaying and sizing. With the black contrast set to 30 nN and bright contrast set to 800 nN, the AFM scanned the blade pattern with the defined forces. The results are shown in Figure 4.3B, where the blade is clearly visible, appearing as negative contrast in the AFM topograph. The structure faithfully followed the design with R chirality. The parent circles had **D** = 3.43 ± 0.15 μm, with center-center separation of **d** = 0.79 ± 0.08 μm. The width of the blade lines at FWHM was 0.23 ± 0.07 μm. The diameter of the central circle was 1.15 ± 0.07 μm. The anthracene termini regions were 3.83 ± 0.39 nm lower than that of the surrounding polymer brush. This structure is consistent with the activation of the MAs under the high force via the retro-Diels−Alder reaction, followed by the departure of PGMA groups.[16]

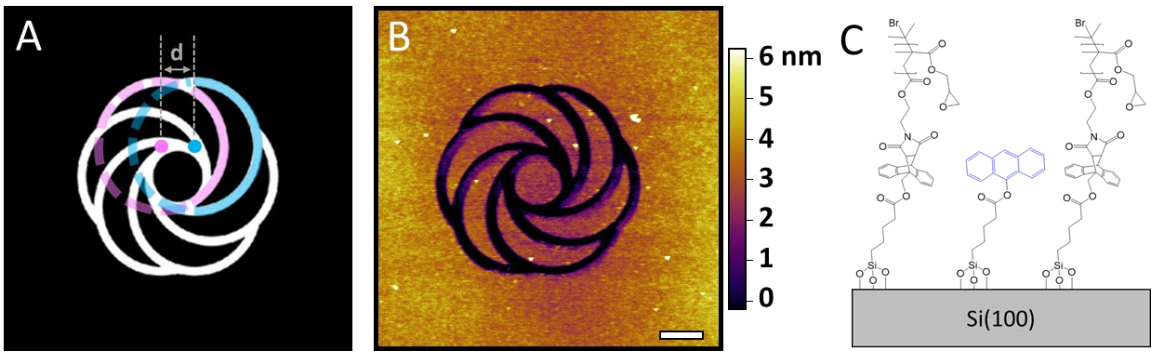

Figure 4.3. (A) The design of a 6-bladed fan feature with R chirality. (B) A 6 µm x 6 µm AFM topographic image taken after production of the R-bladed fan shown in (A). The image was acquired in DMSO under an imaging force of 18 nN at 17.53 µm/s. Scale bar is 1.0 µm. (C) Schematic diagram illustrating the molecular adsorbates and terminal functionalities across the patterned region.

While the reactions used in Figures 4.1 and 4.2 were adsorption directed by AFM scans, the reactions achieved in Figures 4.3 and 4.4 were based on detachment of PGMA tails by the local force exerted via the AFM probe. The later enables production of multi-contrast organizational chiral features, as illustrated in Figure 4.4. A multi-contrast R-bladed fan was designed and produced. Different from the design in Figure 4.3, the fan in Figure 4.4 has 6 solid and well-separated blades, with each pair of opposite blades assigned a contrast in grey scale (Figure 4.4A, inset). Setting the shaving force, based on blade contrast in the design, to be 333, 617 and 900 nN for dark, grey and bright, respectively, the AFM probe was able to activate the MA groups in the blade regions, with the number of MA groups activated based on the actual force setting,[16] resulting in the complex, multi-contrast organizational chiral structure shown in Figure 4.4. The diameter, **D** of the parent circles measured 3.79 ± 0.04 µm with center-center separation **d** = 0.97 ± 0.03 µm.

as shown in Figure 4.4A. The diameter of the central circle was 1.28 ± 0.02 μm, with a depth of 7.0 nm. The depths of each 'blade' feature are 1.63, 4.19 and 7.00 nm lower than the surrounding, corresponding to the densities of MA activation of 23%, 60% and 100%, respectively.[16] Corroborating evidence arises from the lateral image, acquired simultaneously with the AFM topograph, shown in Figure 4.4B, where the contrast is opposite of that in topographic image, as the lateral force in the anthracene regions is higher than that in the bromide terminated regions.[16]

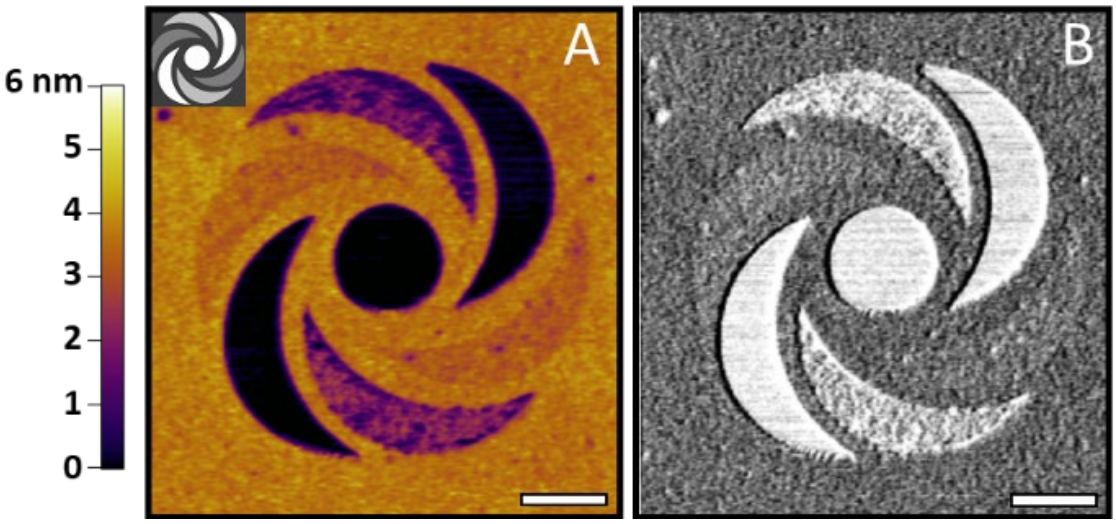

Figure 4.4. (A) An AFM topographic image taken after scanning the chiral grayscale image inset on a MA surface. (B) Lateral image acquired simultaneously. Images were collected in DMSO under 70 nN and a speed of 22.54 μm/s. Scale bars = 1.0 μm.

In the case of organizational chirality from self-assembly, the area covered by chiral features depended on the interplay between thermodynamics and kinetics. Often the region occupied by one type of chiral features is finite[8, 10, 13, 32-34] and the entire surface is covered by

interspaced regions of various structures and chiralities.[10, 12, 33, 35-38] Our approach, in principle, could cover the entire surface with one type of chiral features by design, which brings organizational chiral structures closer towards practical applications.[39] Figure 4.5 demonstrates the feasibility to produce arrays of chiral features by design on the designated locations on surfaces. A 3 x 3 array of R-bladed fans was designed and produced, following the similar protocols to that in Figures 4.3. The periodicity of the 3 x 3 array measured 1.69 ± 0.01 μm. The individual feature within the array were R-bladed fans. The parent circles **D** measured 0.90 ± 0.03 μm, with center-center separation of **d** = 0.27 ± 0.02 μm. The width of the blade lines at FWHM was 0.13 ± 0.01 μm. The lateral dimension of the central region was 0.28 ± 0.01 μm.

The current AFM instrument used for this investigation has the capability to produce chiral features covering an entire 100 μm x 100 μm in a single scan-frame. Then the probe could be moved manually via a precision micrometer to the adjacent 100 μm x 100 μm area to repeat the nanofabrication, until a millimeter sized surface regions are covered..

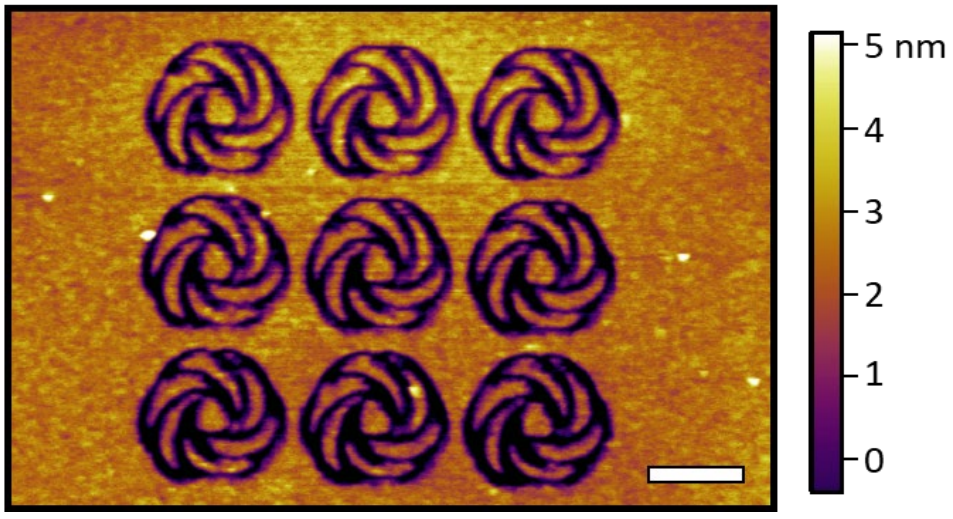

Figure 4.5. AFM topographic image of a 3 x 3 array of chiral structures produced following similar protocols as that in Figure 4.3. Each chiral structure is a 6-bladed fan with R chirality. Dark

features correspond to anthracene termini while the lighter features are the bromine termini of the PGMA chains. The image was acquired in DMSO under an imaging force of 18 nN at 17.52 μm/s. Scale bar = 1.0 μm.

4.3.3 Production of Hierarchical Chiral Features by Design.

Taking full advantages of this technology's capability to make organizational chiral structures by design, we attempted to produce highly complex designs, i.e., hierarchical chiral structures where the individual structures and their arrangement are both chiral. Figure 4.6A provides an example design of a hierarchical chiral structure where each element was an Archimedean spiral with R chirality, and these spirals were arranged periodically along a rectangular spiral, also with R chirality. This design is referred to as an $\mathbf{R}^{\mathbf{R}}$ structure, where R represents the chirality of the individual elements and superscript $^{\mathbf{R}}$ denotes the chirality of their arrangement along the chiral feature.

Quantitatively, the designed Archimedean spirals have R-chirality, and followed Eq. 9:

$$r\ (nm) = -29.00\ (nm) \times\ \theta \tag{9}$$

with θ ranging from 0 to 6.5π. This design is similar to the R spiral in Figure 4.1A. There are 35 Archimedean spirals in this design, whose centers were arranged following the trajectory of the rectangular spiral with a periodicity of 1.30 μm. To facilitate understanding of the arrangement and progression in this design, we started with the smallest rectangle with the side lengths of a_1 and b_1 (Fig. 6A). Starting at the corner, the spiral was placed as per the designed periodicity, then the spiral adjacent to the upper left corner was removed, thus leading to a rectangular spiral instead

of a simple rectangle. The 2nd rectangle utilized three sides of the first rectangle, excluding the side with a missing spiral, then expanded b_1 by two periods creating a_2, and reassigned a_1 as b_2. Next, the spirals were again placed from the top left corner and along the top side with 1.00 μm separation to complete b_2. Finally, the spiral adjacent to the top right corner of a_2 was removed. This iteration or progression continued till the 5th cycle to complete our design shown in Figure 4.6A, following Eqs. 10 and 11:

$$a_n\,(\mu m) = (n+2) \times \mathrm{p}\,(\mu m) \tag{10}$$

$$b_n\,(\mu m) = (n+1) \times p\,(\mu m) \tag{11}$$

Where p is the periodicity; a_n and b_n are the long and short side of each rectangle, respectively; and n = 1 to 5 represents the number of progression cycles.

Figure 4.6B shows the results of the AFM-directed nanolithography following the design in Figure 4.6A, using the protocols similar to that described in Figure 4.1. The individual Archimedean spirals follow the design faithfully, with the spirals defined by Eq. 12:

$$r = (-28.25 \pm 1.24) \times \theta \tag{12}$$

with θ ranging from 0 to 6.5 π. The width of the spiral line at FWHM was 96.07 ± 13.58 nm. These Archimedean spirals were aligned along the R-rectangular spiral with the periodicity, p, measured as 1.33 ± 0.03 μm. The R-rectangular spiral expanded up to 5 progressions. The Archimedean spiral lines correspond to the anthracene-terminated areas, which measured 5.21 ± 0.78 nm lower than the surrounding from AFM topographic images, consistent with the activation of the MA mechanophores. In the AFM deflection image shown in Figure 4.6B, the bright contrast corresponds to the anthracene functionality while the surrounding is bromine termini of the PGMA chains.

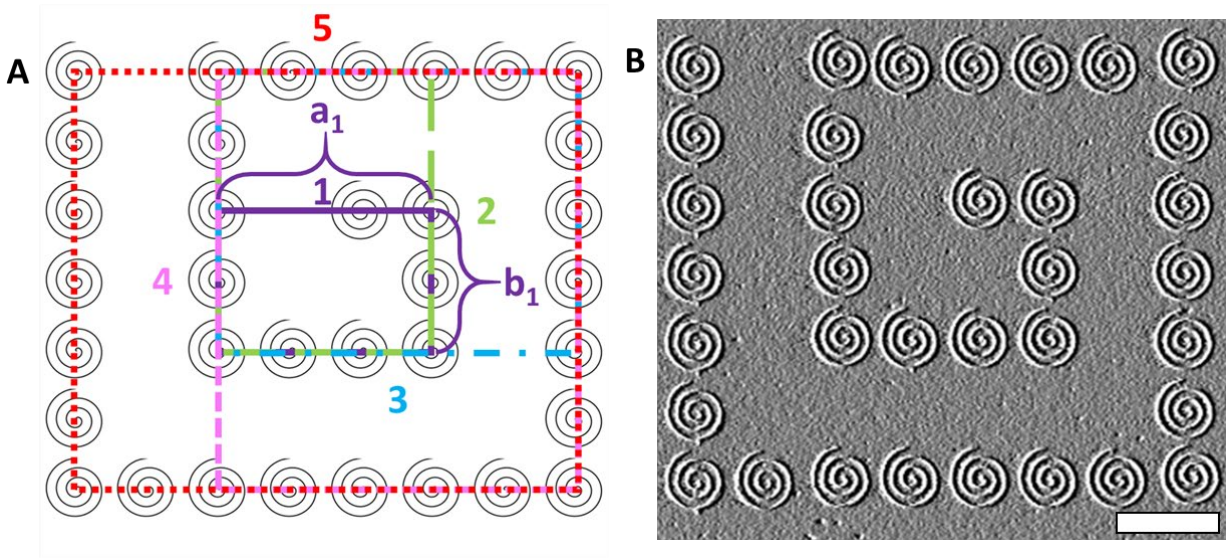

Figure 4.6. (A) A design of a R^R hierarchical spiral. (B) A 11.4 µm x 10.1 µm deflection image of the R^R hierarchical spiral produced following the design in (A). The image was acquired in DMSO under an imaging force of 51 nN at 37.56 µm/s. The lateral scale bar is 2.0 µm.

Following the same procedure as the R^R hierarchical spiral, three additional combinations of hierarchical spirals were fabricated with the chirality combinations as follows: R^R, R^S, S^R and S^S as shown in Figure 4.7 and Table 4.1.

To demonstrate the robustness of the concept of "producing hierarchical chiral structures by design," we have completed the design and production of all four possible combinations of chirality associated with Figure 4.6, i.e., R^R, R^S, S^R and S^S. The results of all four types of hierarchical chiral structures are shown in Figure 4.7 and summarized in Table 4.1. The fidelity is very high in this AFM-based nanolithography. The progression of each of the rectangular spiral is n = 5, and accurately following the design. Using the R^R spiral was an example, the alignment of

the spiral along the rectangle was within 16.7 ± 48.7 nm precision of the intended rectangular spiral line and the periodicity is preserved within tens of nanometers of the design. The other three hierarchical spiral features had similar levels of precise alignment, demonstrating that all configurations can be successfully and precisely produced.

Table 4.1. Summary of hierarchical chiral spirals produced, representing all four possible combinations of chirality. The measurements are taken from AFM topographic as well as deflection images.

Hierarchical Chirality	R^R	R^S	S^R	S^S
Archimedean Spirals Produced				
Equation form of the Archimedean spirals produced	$r = \theta \times (-28.25 \pm 1.24)$	$r = \theta \times (-26.90 \pm 1.98)$	$r = \theta \times (29.60 \pm 0.58)$	$r = \theta \times (25.54 \pm 0.74)$
θ Range	0 to 6.5 π	0 to 6.5 π	0 to 6.5 π	0 to 6.5 π
Line width (nm)	96.07 ± 13.58	88.05 ± 15.45	98.64 ± 17.33	91.58 ± 12.91
Height difference after MA activation (nm)	5.21 ± 0.78	6.10 ± 0.78	5.26 ± 1.46	6.33 ± 1.11
Alignment of Archimedean Spirals Along the Rectangular Spiral				
Progression range, n	n= 1-5	n= 1-5	n= 1-5	n= 1-5
Periodicity, p (μm)	1.33 ± 0.03	1.27 ± 0.02	1.46 ± 0.0.08	1.22 ± 0.02

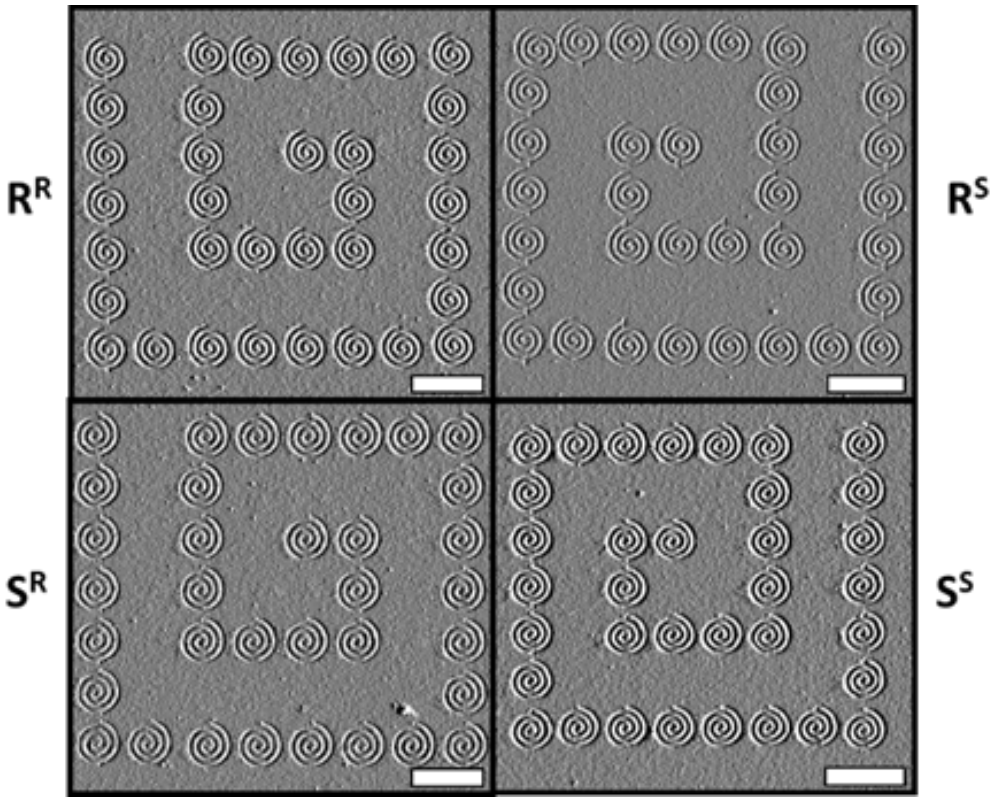

Figure 4.7. The four AFM deflection images of the hierarchical chiral spirals produced following the designs. All four possible combinations of chirality were designed and produced, as indicated in the images. All images were acquired in DMSO under the imaging force of 51, 13, 47 and 23 nN, with the scanning speed of 37.56, 31.30, 35.06 and 32.55 μm/s, respectively, in the four experiments. All lateral scale bars = 2.0 μm.

4.4 Conclusions

This work introduces our approach to create organizational chirality by design. Current methods for production of organizational chirality are primarily based upon self-assembly of molecules. While powerful, the chiral structures produced are restricted to those dictated by reactions thermodynamics. Using atomic force microscopy in conjunction with one's chosen

surface reactions, our methodology enables production of various chiral structures by design with nanometer precision, from simple chiral spirals to arrays of chiral nanofeatures to hierarchical chiral structures. The size, geometry, and organizational chirality followed the designs with a high degree of spatial fidelity. The concept and methodology enabled researchers to carry out organizational chiral chemistry, with the intrinsic advantages of chiral structures by design. The individual chiral structures, their locations on surfaces, and total coverage by these organizational chiral structures can all be controlled. Being able to selectively produce a single chiral form offers the possibility to create enantioselectivity on the surface, which is critical for future enantioselective applications of these structures. By employing parallel processing techniques,[39] the throughput of organizational chirality by design can be greatly increased, making large scale array feasible in a reasonable amount of time. The results open new and promising applications including organizational chiral sensors, 3D nanoprinting of chiral structures, enantiomeric separation, and enantiomeric heterogeneous catalysis.

4.5 References

1. Mallat, T.; Orglmeister, E.; Baiker, A., Asymmetric catalysis at chiral metal surfaces. *Chemical Reviews* **2007,** *107* (11), 4863-4890.

2. Gellman, A. J., Chiral Surfaces: Accomplishments and Challenges. *Acs Nano* **2010,** *4* (1), 5-10.

3. Mark, A. G.; Forster, M.; Raval, R., Recognition and Ordering at Surfaces: The Importance of Handedness and Footedness. *Chemphyschem* **2011,** *12* (8), 1474-1480.

4. Darling, G. R.; Forster, M.; Lin, C.; Liu, N.; Raval, R.; Hodgson, A., Chiral segregation driven

by a dynamical response of the adsorption footprint to the local adsorption environment: bitartrate on Cu(110). *Phys Chem Chem Phys* **2017,** *19* (11), 7617-7623.

5. Bombis, C.; Weigelt, S.; Knudsen, M. M.; Norgaard, M.; Busse, C.; Laegsgaard, E.; Besenbacher, F.; Gothelf, K. V.; Linderoth, T. R., Steering Organizational and Conformational Surface Chirality by Controlling Molecular Chemical Functionality. *Acs Nano* **2010,** *4* (1), 297-311.

6. Barlow, S. M.; Raval, R., Complex organic molecules at metal surfaces: bonding, organisation and chirality. *Surf Sci Rep* **2003,** *50* (6-8), 201-341.

7. Raval, R., Chiral expression from molecular assemblies at metal surfaces: insights from surface science techniques. *Chem Soc Rev* **2009,** *38* (3), 707-721.

8. Liu, J.; Chen, T.; Deng, X.; Wang, D.; Pei, J.; Wan, L. J., Chiral Hierarchical Molecular Nanostructures on Two-Dimensional Surface by Controllable Trinary Self-Assembly. *Journal of the American Chemical Society* **2011,** *133* (51), 21010-21015.

9. Ecija, D.; Seufert, K.; Heim, D.; Auwarter, W.; Aurisicchio, C.; Fabbro, C.; Bonifazi, D.; Barth, J. V., Hierarchic self-assembly of nanoporous chiral networks with conformationally flexible porphyrins. *ACS Nano* **2010,** *4* (8), 4936-42.

10. Pendery, J.; Ferjani, S.; Rosenblatt, C.; Petschek, R. G., Spatially controllable surface chirality at the nanoscale. *Epl-Europhys Lett* **2011,** *96* (2).

11. Navikas, V.; Gavutis, M.; Rakickas, T.; Valiokas, R., Scanning Probe-Directed Assembly and Rapid Chemical Writing Using Nanoscopic Flow of Phospholipids. *ACS applied materials & interfaces* **2019,** *11* (31), 28449-28460.

12. Sulkanen, A. R.; Sung, J.; Robb, M. J.; Moore, J. S.; Sottos, N. R.; Liu, G.-y., Spatially

Selective and Density-Controlled Activation of Interfacial Mechanophores. *Journal of the American Chemical Society* **2019,** *141* (9), 4080-4085.

13. Xu, S.; Miller, S.; Laibinis, P. E.; Liu, G. Y., Fabrication of nanometer scale patterns within self-assembled monolayers by nanografting. *Langmuir : the ACS journal of surfaces and colloids* **1999,** *15* (21), 7244-7251.

14. Xu, S.; Cruchon-Dupeyrat, S. J. N.; Garno, J. C.; Liu, G. Y.; Jennings, G. K.; Yong, T. H.; Laibinis, P. E., In situ studies of thiol self-assembly on gold from solution using atomic force microscopy. *Journal of Chemical Physics* **1998,** *108* (12), 5002-5012.

15. Strong, L.; Whitesides, G. M., Structures of Self-Assembled Monolayer Films of Organosulfur Compounds Adsorbed on Gold Single-Crystals - Electron-Diffraction Studies. *Langmuir : the ACS journal of surfaces and colloids* **1988,** *4* (3), 546-558.

16. Dubois, L. H.; Nuzzo, R. G., Synthesis, Structure, and Properties of Model Organic-Surfaces. *Annual Review of Physical Chemistry* **1992,** *43*, 437-463.

17. Liu, M.; Amro, N. A.; Liu, G.-y., Nanografting for Surface Physical Chemistry. *Annual Review of Physical Chemistry* **2008,** *59* (1), 367-386.

18. Love, J. C.; Estroff, L. A.; Kriebel, J. K.; Nuzzo, R. G.; Whitesides, G. M., Self-assembled monolayers of thiolates on metals as a form of nanotechnology. *Chemical Reviews* **2005,** *105* (4), 1103-1169.

19. Ulman, A., Formation and structure of self-assembled monolayers. *Chemical Reviews* **1996,** *96* (4), 1533-1554.

20. Xia, Y. N.; Rogers, J. A.; Paul, K. E.; Whitesides, G. M., Unconventional methods for fabricating and patterning nanostructures. *Chemical Reviews* **1999,** *99* (7), 1823-1848.

21. Gates, B. D.; Xu, Q. B.; Stewart, M.; Ryan, D.; Willson, C. G.; Whitesides, G. M., New approaches to nanofabrication: Molding, printing, and other techniques. *Chemical Reviews* **2005,** *105* (4), 1171-1196.

22. Wen, K.; Maoz, R.; Cohen, H.; Sagiv, J.; Gibaud, A.; Desert, A.; Ocko, B. M., Postassembly chemical modification of a highly ordered organosilane multilayer: New insights into the structure, bonding, and dynamics of self-assembling silane monolayers. *Acs Nano* **2008,** *2* (3), 579-599.

23. Rosa, L. G.; Liang, J., Atomic force microscope nanolithography: dip-pen, nanoshaving, nanografting, tapping mode, electrochemical and thermal nanolithography. *J Phys-Condens Mat* **2009,** *21* (48).

24. Bu, D. L.; Mullen, T. J.; Liu, G. Y., Regulation of Local Structure and Composition of Binary Disulfide and Thiol Self-Assembled Monolayers Using Nanografting. *Acs Nano* **2010,** *4* (11), 6863-6873.

25. Jung, H.; Kulkarni, R.; Collier, C. P., Dip-pen nanolithography of reactive alkoxysilanes on glass. *Journal of the American Chemical Society* **2003,** *125* (40), 12096-12097.

26. Li, J.; Nagamani, C.; Moore, J. S., Polymer Mechanochemistry: From Destructive to Productive. *Accounts Chem Res* **2015,** *48* (8), 2181-2190.

27. Li, J.; Shiraki, T.; Hu, B.; Wright, R. A. E.; Zhao, B.; Moore, J. S., Mechanophore Activation at Heterointerfaces. *Journal of the American Chemical Society* **2014,** *136* (45), 15925-15928.

28. Chen, T.; Yang, W. H.; Wang, D.; Wan, L. J., Globally homochiral assembly of two-dimensional molecular networks triggered by co-absorbers. *Nat Commun* **2013,** *4*, 1389.

29. De Cat, I.; Guo, Z.; George, S. J.; Meijer, E. W.; Schenning, A. P.; De Feyter, S., Induction of chirality in an achiral monolayer at the liquid/solid interface by a supramolecular chiral auxiliary.

J Am Chem Soc **2012,** *134* (6), 3171-7.

30. Stepanow, S.; Lin, N.; Vidal, F.; Landa, A.; Ruben, M.; Barth, J. V.; Kern, K., Programming supramolecular assembly and chirality in two-dimensional dicarboxylate networks on a Cu(100) surface. *Nano Lett* **2005,** *5* (5), 901-4.

31. Chen, T.; Wang, D.; Wan, L.-J., Two-dimensional chiral molecular assembly on solid surfaces: Formation and regulation. *National Science Review* **2015,** *2*.

32. Vidal, F.; Delvigne, E.; Stepanow, S.; Lin, N.; Barth, J. V.; Kern, K., Chiral phase transition in two-dimensional supramolecular assemblies of prochiral molecules. *J Am Chem Soc* **2005,** *127* (28), 10101-6.

33. Ernst, K.-H., Molecular chirality at surfaces. *physica status solidi (b)* **2012,** *249* (11), 2057-2088.

34. Raval, R., Chiral expressions at metal surfaces. *Current Opinion in Solid State and Materials Science* **2003,** *7* (1), 67-74.

35. Vettiger, P.; Despont, M.; Drechsler, U.; Durig, U.; Haberle, W.; Lutwyche, M. I.; Rothuizen, H. E.; Stutz, R.; Widmer, R.; Binnig, G. K., The "Millipede"—More than thousand tips for future AFM storage. *IBM Journal of Research and Development* **2000,** *44* (3), 323-340.

36. Xu, S.; Liu, G.-y., Nanometer-Scale Fabrication by Simultaneous Nanoshaving and Molecular Self-Assembly. *Langmuir : the ACS journal of surfaces and colloids* **1997,** *13* (2), 127-129.

CHAPTER 5

Controlled Molecular Assembly of Tetrazine Derivatives on Surfaces

5.1 Introduction

Assembly of molecules into micro- and nano-scale structures by design still poses a great challenge.[1] Self-assembly (SA) of molecules provides one good means to assemble molecules into mesoscale structures, such as self-assembled monolayers (SAMs),[2-4] phase-separated polymers,[5, 6] molecular brushes[7], block copolymers[8] and lipid bilayers.[9, 10] While powerful, self-assembly is limited to structures or molecular assemblies that are favored thermodynamically.[11, 12] This limitation makes it difficult to achieve molecular assembly by design using self-assembly alone. Thus, new approaches need to be developed to reach "molecular assembly by design", thereby enabling production of a wider range of structures and materials with designed properties and functions.

Controlled assembly to produce 0 dimensional (0D) assemblies has been demonstrated by our team using macromolecules, including star polymers (M_n of 383 kDa, hydrodynamic radius of 13.8 nm).[13] The study indicated that factors governing the solute assembly in ultrasmall droplets significantly differs from that of larger droplets, as ultrasmall droplets exhibit ultrafast evaporation, and as such, the initial droplet geometry and concentration of the solute play dominant roles in dictating the final assembly of solute molecules. The applicability of this methodology to the assembly of low molecular weight molecules, such as small linear polymers, is becoming the new task. The use of small molecules is appealing for several reasons, as they are generally easier to

synthesize, less expensive, more stable, and more readily available than macromolecules that require significant time, money, and research to fabricate. This work applies the concept of controlled assembly to *bis*-tetrazine modified poly(ethylene glycol) (PEG-*bis*Tz), with M_w of 8.1 kDa, and dynamic radius near 1.5 nm.[14, 15] Functionalized PEGs have been widely used for surface modification and for the synthesis of complex molecules and networks.[16, 17] Moreover, the tetrazine functionality within the molecule is known to participate in tetrazine-ligation with *trans*-cyclooctene (TCO) derivatives.[15] These bio-orthogonal inverse electron demand Diels−Alder reactions occurred fast and required no additional additives.[18-22] These reactions are also clean, producing nitrogen gas as the only by product,[18-22] and thus are utilized as an important tool for producing extracellular matrix mimetic hydrogels and polymers.[15, 23, 24] To further advance the applications of PEG-*bis*Tz and three-dimensional (3D) nanoprinting technology, this study demonstrates the concept of controlled molecular assembly of PEG-*bis*Tz from 0D - 3D, combining our methodology of using ultrasmall droplets (sub-aL) and surface patterning. The level of control reported in this work paves the way for future applications including 3D nanoprinting, as well as programmable and engineered means to produce complex and hierarchical structures of materials.[25-27]

5.2 Experimental Methods

5.2.1 Materials.

Glass slides (22 mm × 22 mm × 0.25 mm) were purchased from Fisher Scientific (Pittsburgh, PA). Sulfuric acid (H_2SO_4, 95.0−98.0%), hydrogen peroxide (H_2O_2, 30% aqueous solution), ammonium hydroxide (NH_4OH, 30% aqueous solution), tetrahydrofuran (THF) and toluene (99.8%) were purchased from Sigma-Aldrich (St. Louis, MO). N-(6-aminohexyl) aminopropyltrimethoxysilane (AAPTMS) was purchased from Gelest (Morrisville, PA). Ethanol (99.5%) was purchased from KPTEC (King of Prussia, PA). Milli-Q water (MQ water, 18.2 MΩ·cm at 25 °C) was produced by a Milli-Q water purification system (EMD Millipore, Billerica, MA). Nitrogen gas (99.999%) was purchased from Praxair, Inc. (Danbury, CT, King of Prussia, PA). Deuterated chloroform ($CDCl_3$) was purchased from Cambridge Isotopes (Tewksbury, MA).

5.2.2 Synthesis of PEG-*bis*Tz and C12-*bis*TCO.

PEG-*bis*Tz and C12-*bis*TCO used in this study were synthesized following our previously reported methods using PEG-diamine with a M_w of 7.5 kDa and 1,12-diaminododecane respectively.[15, 28, 29]

5.2.3 Preparation of Surfaces as Support for Material Delivery.

Glass slide substrates were first cleaned following established protocols.[30] Briefly, slides were soaked in piranha solution for 1 h, rinsed with a copious amount of MQ water. Piranha

solution contains H_2SO_4 and H_2O_2 (v/v = 3:1), which should be handled with care for its high corrosiveness. The slides were then treated with a basic bath (mixture of NH_4OH, H_2O_2, and H_2O at a ratio of 5:1:1 (v/v)) for 1 h at 70 °C and then rinsed with a copious amount of MQ water followed by drying in nitrogen gas. Cleaned slides were modified using silane chemistry according to an established protocol.[31] SAM-modified glass slides were prepared as follows: slides were heated at 70−80 °C in a sealed Teflon container (100 mL) containing 200 μL of AAPTMS for 2 h, then rinsed with ethanol and MQ water, and dried again in nitrogen gas.[31] PEG-*bis*Tz coated glass slides were prepared as follows: 20 μL of 2.5×10^{-4} M PEG-*bis*Tz aqueous solution was deposit by 100 μL Eppendorf pipette (Sigma-Aldrich, St. Louis, MO) on AAPTMS modified glass surfaces and dried under ambient conditions for 30 minutes.

5.2.4 Contact Angle Measurement.

Contact angle data of water and PEG-*bis*Tz solution were both collected for the modified substrates with a VCA Optima Contact Angle Measurement system (AST Products, Billerica, MA) according to standard protocols.[32] For water contact angle measurement, typically, a 2 μL drop of MQ water was placed on the substrate using a HPLC needle. At least three different positions per sample were studied to confirm the surface wettability. For PEG-*bis*Tz solution contact angle measurement, an identical procedure was applied except that MQ water was replaced with 2.5×10^{-4} M PEG-*bis*Tz aqueous solution.

5.2.5 Integrated Atomic Force Microscopy and Microfluidic Device.

A microfluidic system (FluidFM Bot, Cytosurge, Glattbrugg, Switzerland) was integrated with an atomic force microscopy (AFM) assembly allowing precise position and movement control, and an inverted optical microscope (IX73, Olympus America, Center Valley, PA).[33, 34] Solution delivery was carried out using a FluidFM Nanopipette (CYPR/001511, Cytosurge, Glattbrugg, Switzerland) with a 300-nm opening. The cantilever was similar to typical AFM silicon probes, 200 μm long, 36 μm wide, and 1.5 μm thick. The spring constant was 2 N/m. The nanopipette was made with a microchannel connected to a reservoir and controlled by a precise pressure controller. The pressure control system enables a pressure application range from −800 to +1000 mbar at a 1 mbar precision. Initially, 1 μL of PEG-*bis*Tz solution was filled into the probe's 2 μL reservoir using a Hamilton 7000 series syringe (Hamilton, Reno, NV).

5.2.6 AFM Imaging.

PEG-*bis*Tz structures deposited on the surface were allowed to dry at room temperature for 30 min before being characterized by AFM (MFP-3D, Oxford Instrument, Santa Barbara, CA). Silicon probes (AC 240-TS, Olympus America, Central Valley, PA) with a force constant of 1.7 N/m and resonant frequency of 70 kHz were used. Topography images were acquired using tapping mode. The driving frequency and damping were set at 70 kHz and 40%, respectively. Images were analyzed using Asylum MFP-3D software on an Igor Pro 6.12 platform. Particularly, the initial volume of droplets deposited on AAPTMS surface was calculated based on the total number of PEG-*bis*Tz molecules in the spherical cap (total solid volume calculated based on the AFM

measured height and diameter/individual PEG-*bis*Tz volume) and the initial concentration in the solution.

5. 3 Results and Discussion

5.3.1 Controlled Assembly of PEG-bisTz in Individual Ultrasmall Droplets.

The surfaces used were clean glass modified by SAMs of AAPTMS. The water contact angles on this SAM measured 55 ± 1.2°, which is consistent with known values for high quality SAMs with amine-termini.[35] Using 2.5×10^{-4} M PEG-bisTz aqueous solution, the contact angle measured 47 ± 1.3°. Thus, the SAM surface is both hydrophilic and "solution-philic". The structure of PEG-bisTz (M_n = 8.1 kDa) is depicted in Figure 5.1. The reduced contact angle of PEG-bisTz solution compared with water is likely due to the stronger interaction of PEG-bisTz solution with the AAPTMS SAMs than pure water. This strong attachment of PEG-bisTz to the AAPTMS surface was also verified independently by subjecting a dried droplet of PEG-*bis*Tz on AAPTMS to a thorough rinsing with water. Despite the hydrophilic nature of PEG, a ~1 nm thick disk of PEG-*bis*Tz remained after the rinse (not shown), demonstrating the stability of the PEG-*bis*Tz assembly on the AAPTMS surface.

Delivery of an ultrasmall droplet was achieved with the microfluidic/AFM delivery system, as illustrated schematically in Figure 5.1. The lateral position of delivery was precisely controlled with a movement range of 240 mm × 74 mm, and precision of 100 nm. An inverted optical microscope with a 10X objective was utilized to monitor the position of probe and the delivery. The vertical or z-movement moves with 4 nm precision and is independent from lateral movement.

The glass slides were placed on the sample stage, above which the probe was mounted to the vertical assembly controlling z-movement. Typical probe-surface contact during delivery is also shown in Figure 5.1, where the contact force was measured and controlled via similar means as conventional AFM with a deflection configuration.[13, 33, 36] The square pyramidal tip tilted 11° from the surface normal. The nanopipette probe had a 300 nm diameter pore located at the probe apex, connected to a microchannel within the probe body. The microchannel was connected to a small reservoir where the PEG-*bis*Tz aqueous solution was stored. This set-up enabled delivery of aqueous droplets as small as 0.4 attoliter (aL).[13]

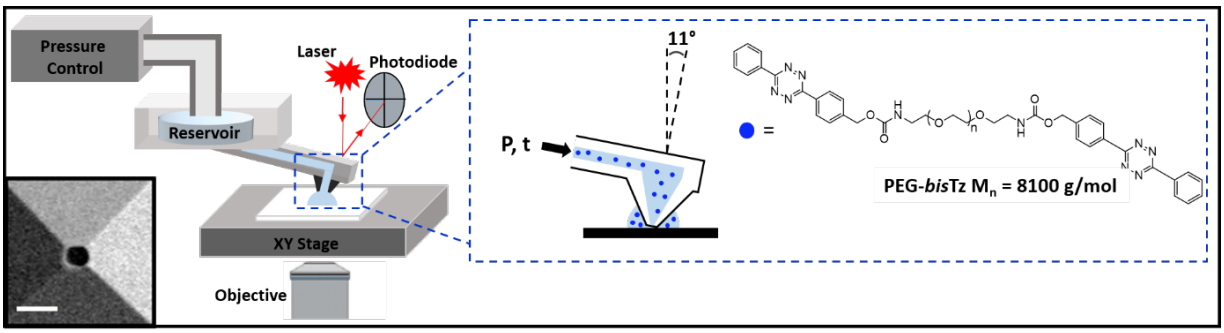

Figure 5.1. Schematic diagram of an integrated AFM with microfluidic delivery probe. An enlarged view illustrates the probe–surface contact. The chemical structure of solute, PEG-*bis*Tz, is also shown. The inset at the lower left is a SEM image of the nanopipette apex with a 300 nm aperture. Scale bar is 500 nm.

First, we have demonstrated that the geometry and size of the individual and concrete assemblies can be controlled with PEG-*bis*Tz molecules tightly packed within. Under a contact force of 40 nN, delivery pressure of 200 mbar and contact time of 0.2 s, 250 aL droplets of PEG-*bis*Tz solution were delivered on the AAPTMS SAM surfaces, as shown in Figure 5.2A. A zoom-in view of one feature is displayed in Figure 5.2B, where PEG-*bis*Tz molecules assembled into a

tiny spherical cap with height and base diameter of 73 nm and 860 nm, respectively. A further zoom-in of a 500 nm × 500 nm area atop of the cap, Figure 5.2C shows a relatively smooth morphology decorated by 16 bumps, ~1.8 nm in height with width ranging from 15-35 nm. These bumps are likely due to clustering of PEG-*bis*Tz molecules. This geometry and the packing can be rationalized by the following: (a) the contact angle of the droplet, 47°, dictated the overall geometry of the droplet and contact 'footprint', i.e. a short spherical hat (b) the solution-surface interaction also determined the evaporation profile, in this case, fast constant area evaporation, due to the quantity of tetrazine in the droplet exceed monolayer, the final feature is a short spherical dome, closely packed, interdigitated within, as shown in Figure 5.2. This is consistent with prior observation with macromolecules as well.[13] The 860 nm diameter base of the cap was dictated by the initial spreading of the droplet, and the number of PEG-*bis*Tz molecules within the mound was determined by the concentration and volume. The intra-feature morphology is also consistent with clustering of PEG-*bis*Tz as a result of constant area evaporation,[37, 38,27], i.e. freezing of PEG-*bis*Tz in the dynamically confined space. These observations are highly reproducible, as we made 11×11 arrays of PEG-*bis*Tz assemblies, shown in Figure 5.2A, where feature dimensions are within 2%, all have spherical cap geometry, and their morphologies are similar to that shown in Figure 5.2C. These observations indicate that using ultrasmall droplet and rapid evaporation, spherical cap shaped assemblies were produced with PEG-*bis*Tz molecules tightly packed within. In other words, the initial droplet shape dictates the outcome of the individual and concrete assemblies of molecules due to fast evaporation. The concept of controlled assembly using small liquid droplets was first reported by our team using macromolecules, e.g. star polymers.[13] This result extends the concept to much smaller molecule, PEG-*bis*Tz, which has a hydrodynamic radius of 1.5 nm.

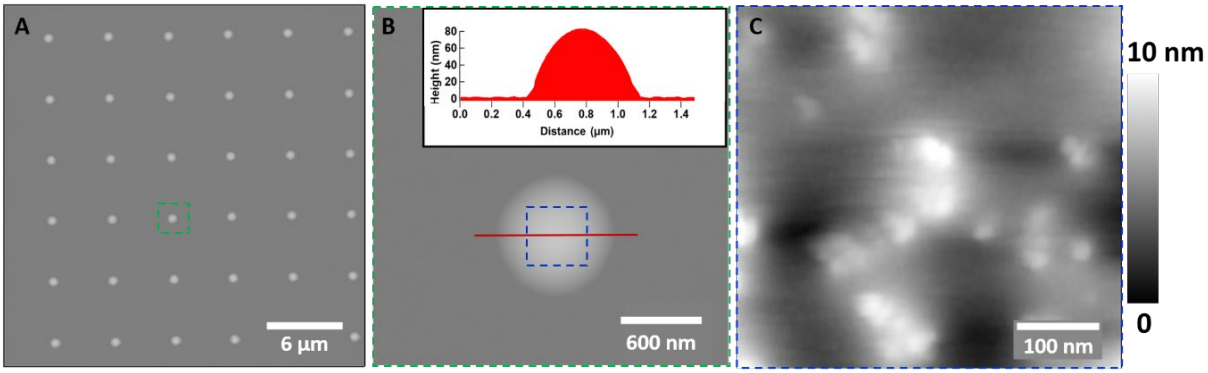

Figure 5.2. (A) An AFM topographic image of an array of PEG-*bis*Tz spherical caps. (B) A zoom-in view of a single feature as indicated in (A). The top inset is the corresponding cursor profile. (C) A further zoom-in view from the region as indicated (B).

The robustness of our approach was demonstrated by forming PEG-*bis*Tz spherical caps with various sizes by varying delivery parameters such as contact time (t) and pressure (p). Results shown in Figure 5.3 correlate the increase of base and height with the increasing contact time. At contact force of 40 nN and delivery pressure of 200 mbar, a 5 × 6 array of PEG-*bis*Tz droplets with periodicity of 7 µm was delivered on an AAPTMS glass surface. From the bottom to the top row in Figure 5.3A, the contact time increased during initial delivery, resulting in larger droplets, thus larger spherical caps, as summarized in Table 5.1. The quantitative plot is shown in Figure 5.3B, where both the base and height increased with increasing contact time. These observations indicate that the size of these individual and concrete 0D structures of PEG-*bis*Tz can be controlled by varying the amount of materials delivery in our approach.

Table 5.1. The PEG-*bis*Tz spherical caps formed via controlled assembly, in correlation with contact time

Dwell Time (s)	Pressure (mbar)	Force (nN)	Volume (aL)	Height (nm)	Base diameter

					(µm)
0.10	200	40	82 ± 5	51 ±2	0.59 ± 0.06
0.20	200	40	250 ± 12	73 ± 3	0.86 ± 0.08
1.33	200	40	474 ± 23	94 ± 2	1.04 ± 0.05
2.56	200	40	1046 ± 45	131 ± 4	1.32 ± 0.07
3.78	200	40	1241 ± 58	139 ± 3	1.41 ± 0.09
5.00	200	40	1633 ± 69	157 ± 5	1.49 ± 0.07

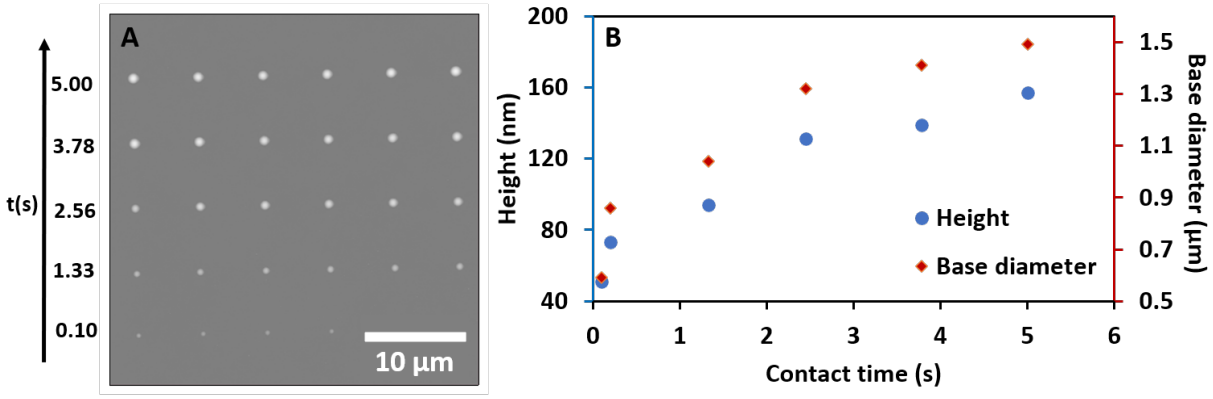

Figure 5.3. (A) AFM topographic image of an array of PEG-*bis*Tz spherical caps created with various dwell times from 0.1 to 5 s under pressure of 200 mbar. (B) Plot showing the variation of the dimensions of PEG-*bis*Tz spherical caps with dwell time.

5.3.2 Controlled Assembly of PEG-*bis*Tz During Continuous Delivery of Solution Along Lines.

With knowledge of the 0D delivery conditions and the corresponding geometry of the resulting PEG-*bis*Tz features, we moved one step further to delivering solutions while moving the surface along a line, thereby creating a 1D trajectory of solute upon drying. One could conceptually understand the 1D delivery as a delivery of droplets continuously, in contrast to delivery of discrete droplets in 0D. Therefore, the 0D delivery conditions were used as a guide for the desired cross-

section and height of lines in the 1D delivery. As material was delivered along the 1D trajectory, the printing speed, pressure and contact force were kept constant. Figure 5.4A shows an array of four lines formed at 5 μm/s, under a contact force of 40 nN, and delivery pressure of 200 mbar, using a 2.5×10^{-4} M PEG-*bis*Tz aqueous solution. These lines were 1.13 ± 0.02 μm wide and 45 ± 3 nm tall, with a fan-shaped cross section. In Figure 5.4B, the line arrays were produced under identical condition as that in 4A, except we changed the delivery direction by 90°. Comparison of the two arrays is further displayed in Figure 5.4C, where the geometry and intra-line morphology are nearly identical. The base width and height of the lines printed at 0° and 90° were measured to be 45 ± 3 nm and 1.13 ± 0.02 μm, 46 ± 3 nm and 1.15 ± 0.03 μm, respectively. Therefore, the delivery of PEG-*bis*Tz solution showed little dependence of the printing directions, in contrast to the printing of highly viscous materials such as photopolymers.[33] These results have been reproduced 40 times along various printing directions. We attribute the independence on printing directions to the low viscosity of PEG-*bis*Tz solution, which is close to 1.0016 mPa·s, similar to that of water.[39, 40] The liquid geometry, upon delivery, is dictated primarily by the volume of liquid and surface tensions at the printing sites, in contrast to in contrast to photopolymers, whose viscosity measured 6,000−13,500 mPa·s, would depend on delivery geometry such as directions.[33] In this low viscosity situation, the outcome of the molecular assembly could be understood as equivalent to a two-step process: producing a liquid line with arched cross section, and rapid drying of solvent to form final assembly. Therefore, the initial liquid line shape and geometry would dictate the overall size and geometry of the final assembly of solid.

The control over 1D delivery of liquid was also demonstrated by producing lines with various widths by tuning the delivery conditions. By decreasing movement speed, while keeping

load and pressure constant, lines with increasing width and height were produced, as shown in Figure 5.4D and quantified in Table 5.2. At contact force of 40 nN and delivery pressure of 200 mbar, 9 PEG-*bis*Tz lines with spacing of 10 µm were delivered on an AAPTMS glass surface. From left to right in Figure 5.4D, the printing speed decreases, resulting in wider and taller lines, from 1.58 µm and 55.8 nm to 2.84 µm and 100.8 nm for base width and height, respectively. This dependence of line height and width on printing speed provides a means to control the size of the 1D assemblies and demonstrates the robustness of this technique. As printing speed decreases, the contact time at each delivery point increases, which is equivalent to a larger droplet being delivered at each point, and results in a larger cross-section collectively along the line. With rapid, constant area evaporation at each point, a line of solute with uniform cross section is produced. In other words, controlled assembly was successfully demonstrated for PEG-*bis*Tz systems to form 1D features: lines and line arrays along designed trajectories.

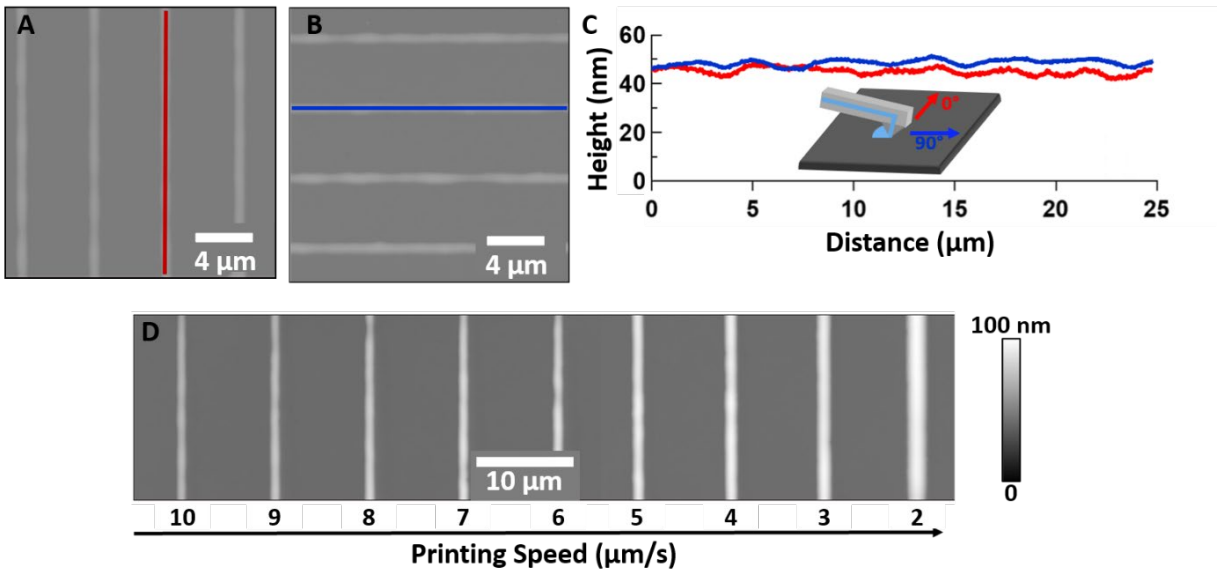

Figure 5.4. (A) An AFM topographic image of 4 PEG-*bis*Tz lines from an array of 20 lines with

periodicity of 5 μm. (B) An AFM topographic image of 4 PEG-*bis*Tz lines from an array 20 lines with periodicity of 5 μm. The stage movement in (B) is perpendicular to that in (A). (C) Combined cursor profiles from the lines indicated in (A) (red) and (B) (blue), and the schematic diagram indicates the movement directions. (D) AFM topographic image of an array of 9 PEG-*bis*Tz lines formed with increasing speed, under the delivery pressure of 200 mbar.

Table 5.2. The PEG-*bis*Tz nanolines formed via controlled assembly, in correlation with the moving speed of the probe along the line.

Printing speed (μm/s)	Pressure (mbar)	Contact Force (nN)	Height (nm)	Base diameter (μm)
2	200	40	100.8 ± 0.6	2.84 ± 0.06
3	200	40	98.5 ± 0.6	2.25 ± 0.03
4	200	40	93.6 ± 0.5	2.05 ± 0.02
5	200	40	89.4 ± 0.5	1.95 ± 0.03
6	200	40	81.7 ± 0.4	1.76 ± 0.03
7	200	40	76.6 ± 0.5	1.76 ± 0.02
8	200	40	71.1 ± 0.6	1.76 ± 0.03

5.3.3 The Impact of Surface Patterning on The Assembly of PEG-bisTz.

Given the significance of the initial liquid shape and geometry, we have attempted various means to control the initial delivery, one of which is to use pre-patterned surfaces. To investigate the effect of surface patterning on the controlled assembly of PEG-*bis*Tz, two sets of perpendicular line arrays were printed within the same area, resulting in a grid of intersecting lines. The first set of lines were an array of 10 PEG-*bis*Tz lines printed on an AAPTMS/glass surface, and then dried under ambient conditions for 30 min. The delivery conditions were 200 mbar, 5 μm/s and 40 nN contact force, which produced solid and homogeneous lines. Each line was 100 μm long, 45 ± 2 nm tall, 1.12 ± 0.04 μm wide, with interline periodicity of 5 μm. Under the same conditions and

design, another array of PEG-*bis*Tz lines was printed, perpendicular to the first set of lines. Figure 5.5A reveals a 25 × 25 μm^2 area of the final structure of intersecting line arrays. The first set of lines contained continuous and homogeneous PEG-*bis*Tz lines on an AAPTMS SAM, which was expected, following the discussion in previous section. The second array, however, contained broken lines, with a bulge at each intersection, despite the fact that both arrays were produced under identical conditions. Cursor plots along the two primary directions are displayed in Figure 5.5B, where the differences were clearly revealed quantitatively. The first set of lines were homogenous continuous lines with height and width of 45 ± 2 nm and 1.12 ± 0.04 μm. The second set of lines were broken lines with bulges, with a bulge-to-bulge distance of 1.72 ±0.06 μm, where there was no material deposition. Figure 5.5C shows an angled 3D AFM image of a representative bulge at a cross-section. This bulge feature measured 117 nm high, with perpendicular short axis and long axis widths of 1.82 μm and 3.71 μm, respectively.

Since PEG-*bis*Tz solutions were delivered under identical conditions in both line arrays, the differences in the resulting structure were attributed to the pre-patterning of the surface. In the case of the first array, the surface region had relatively uniform AAPTMS/glass SAM. In the case of the second array, the surface contained solid line arrays of PEG-*bis*Tz surrounded by the AAPTMS SAM. Figures 5.5D-5.5F rationalize the impact of patterned surfaces on the resulting line geometry of PEG-*bis*Tz. In Figure 5.5D, the geometry of a droplet of PEG-*bis*Tz solution on an AAPTMS SAM is shown: a spherical cap with the contact angle of 47°. Rapid and constant area evaporation led to assembly of PEG-*bis*Tz molecules into a short spherical cap, as discussed in Figure 5.2. Figure 5.5E illustrates the geometry of PEG-*bis*Tz solution upon continuous delivery along a straight line on the AAPTMS SAM surface, assuming no evaporation. This

cylindrical cap can be conceptually considered as the merging of discrete droplets into a line. In reality, evaporation occurred while delivering, but the end result is equivalent, i.e. constant area evaporation at each point during delivery is equivalent to constant area evaporation from the liquid line shown in Figure 5.5E, leading to a solid line with homogeneous height and width. Assuming no interference from the PEG-*bis*Tz lines underneath, delivery linearly along the perpendicular direction should result in a liquid with the shape shown in Figure 5.5F (left). The assumption is incorrect in practice, due to stronger affinity between PEG-*bis*Tz solution and PEG-*bis*Tz lines than that with the AAPTMS surfaces. In fact, the PEG-*bis*Tz solution exhibits a contact angle of 38.0 ± 1.2° atop of dried PEG-bisTz, smaller than that on AAPTMS SAM (47.0 ± 1.3°). Such interactions led to accumulation of the solution at the cross-section region, as illustrated in Figure 5.5F (right), again assuming no evaporation. Finally, constant area evaporation led to the broken line geometry of the second arrays of PEG-*bis*Tz lines. Redistribution of liquid droplets due to micropatterns on surfaces have been reported previously.[41] Our results indicates that the impact of surface patterns goes beyond 0D, e.g., surface patterns underneath directly impact the geometry of lines.

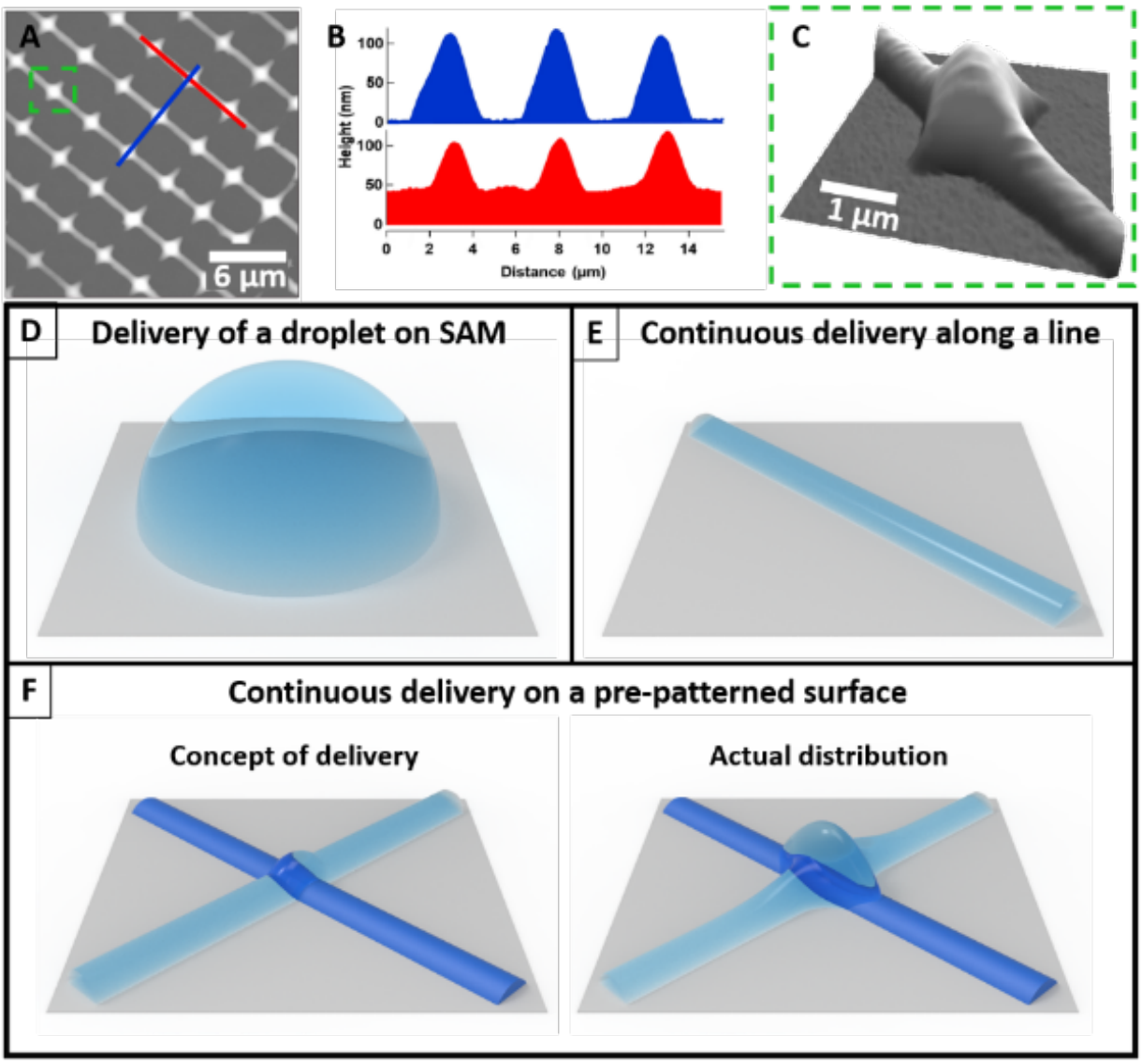

Figure 5.5. (A) AFM topographic image of a representative area of PEG-*bis*Tz mesh. (B) Cursor profile of two cursors in (A). (C) A 3D display of the zoom-in of the green square in (A). (D) Schematic diagram of droplet delivery on SAM. (E) Schematic diagram of continuous line delivery, (F) Schematic diagram illustrating the difference of hypothetical solution distribution and actual distribution, with the darker color line representing the dried line from the first printed set.

The robustness of the aforementioned mechanism was also demonstrated experimentally,

as shown in Figure 5.6. By changing the surface patterns, e.g., decreasing the inter-line spacing or periodicity of the PEG-*bis*Tz lines on AAPTMS surfaces, the geometry of the PEG-*bis*Tz solution delivered during printing of the second set of line arrays could change accordingly. With the identical printing condition as that in Figure 5.5A, three sets of PEG-*bis*Tz line arrays were first produced with the inter-line spacing of 15, 10, and 5 μm, respectively. Each line measured ~100 μm long, 45 ± 2 nm tall, 1.12 ± 0.04 μm wide. The delivery of the second set of line arrays above the three pre-patterned surfaces also followed the same conditions as those in Figure 5.5A. The periodicity of the second set of line arrays matched that of the lines on surfaces, i.e. with the inter-line spacing of 15, 10, and 5 μm, respectively. As shown in Figure 5.6A-5.6C, the resulting three grids reveal clear differences in material redistribution, i.e., the heterogeneity of the second set of line arrays decreased. The cursor profiles in Figure 5.6D compare the heights of the peaks along the lines: 278 ± 10, 166 ± 6, and 114 ± 3 nm, with the decreasing of the periodicity of the line patterns underneath. The short axis base widths also decreased, from 3.8, 3.01 ± 0.07 to 1.77 ± 0.04 μm, while the long axis base widths also decreased from 4.61 ± 0.03, 4.35 ± 0.12 to 3.64 ± 0.08 μm. These trends are consistent with the concept of solution redistribution due to the surface patterns underneath, i.e. less liquid accumulation at the cross-sectional region with decreasing of the inter-line spacing underneath.

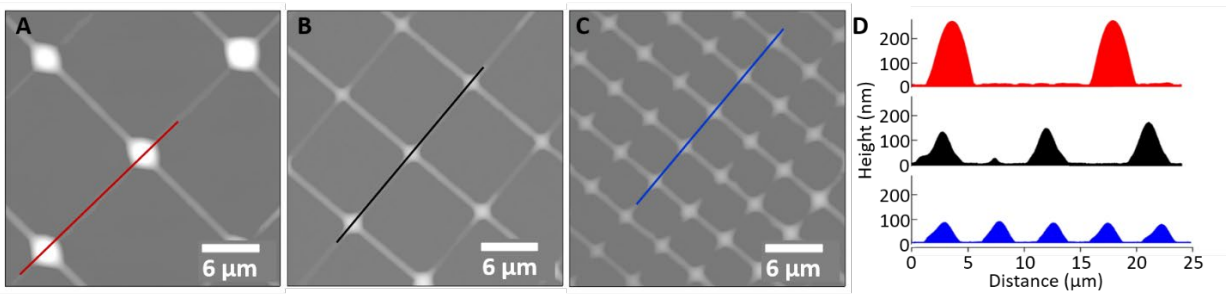

Figure 5.6. AFM topographic images of a representative region of the three PEG-*bis*Tz grids with periodicity of (A) 15 μm, (B) 10 μm and (C) 5 μm, respectively. Each line in the first array was printed diagonally from top-left to bottom-right in each image. Each line in the second array was produced from lower-left to upper-right in each frame. (D) Cursor profiles as indicated in images (A), (B) and (C), respectively.

Further, we have demonstrated that our controlled delivery approach could be combined with surface chemical reactions to produce designed functionalities. Following the same protocols as that in Figure 5.6B, an array of 10 PEG-*bis*Tz lines were produced on AAPTMS glass. Each line was ~100 μm long, 45 nm tall and 1.2 μm wide, with inter-line spacing of 10 μm. Upon drying for 30 minutes under ambient conditions, the surface was immersed into a toluene solution containing 2.5×10^{-4} M dodecane *bis trans*-cyclooctene (C12-*bis*TCO) for 30 minutes, followed by toluene rinsing. The lines measured 1.3 nm tall and 1.2 μm wide, as shown in Figure 5.7A (line features inside the red oval enclosure). These lines were shorter than the initial PEG-*bis*Tz lines deposited. The reduced height from 45 nm to 1.3 nm was due to the Tz-TCO ligation shown in Figure 5.7B, that occurred at the interface of PEG-*bis*Tz solid and C12-*bis*TCO solution. As a result of the reaction, the products located at the outermost solid-solution interaction dissolved into the toluene, exposing fresh PEG-*bis*Tz solid to the C12-*bis*TCO solution above. The cycle of reaction-dissolution perpetuated until reaching the PEG-*bis*Tz attached to the glass surface, where the product remained immobilized on the surface due to the strong attachment of PEG-*bis*Tz to the surface. The surrounding AAPTMS SAM region is known to exhibit little reactivity towards

TCO, thus we anticipate only physisorbed C12-*bis*TCO molecules atop or interdigitated with the AAPTMS molecules.[22]

Next, we created a second array of PEG-*bis*Tz lines, perpendicular to the first, following identical printing conditions as that in the first line array. The new lines, as indicated by the blue arrows in Figure 5.7A, were continuous and relatively homogeneous crossing the un-patterned surface region, with height and base width of 62 nm and 1.35 μm, respectively. Compared to the first array of lines before the C12-*bis*TCO treatment (45 ± 2 nm height, 1.12 ± 0.04 μm width), the second array of lines are taller and wider by 17 nm and 0.15 μm, respectively. This increase in material deposition is mainly attributed to the changes in molecule-surface interactions: from PEG-*bis*Tz with AAPTMS to PEG-*bis*Tz with mixed AAPTMS and C12-*bis*TCO. During the deposition of the 2nd line array, PEG-*bis*Tz molecules reacted with the C12-*bis*TCO molecules immobilized on the surface, thus remaining on site, and leading to structures shown in Figure 5.7A upon drying. At the regions crossing the first set of lines bulges were seen, with a height of 98 nm and a base width of 2.14 μm. In comparison to the lines on the un-patterned region, the bulges at the cross-sections are 0.79 μm wider. This widening is significantly less than in the experiments shown in Figure 5.6B (1.89 μm), where all delivery conditions remained the same. This observation is again attributed to the changes in molecule-surface interactions. In the delivery of PEG-*bis*Tz in the experiments shown in Figure 5.6B, the PEG-*bis*Tz solution interact with AAPTMS surface at the un-patterned area, and with the PEG-*bis*Tz solid lines at the cross section. As such, the liquid "redistributed", leading to thin lines and wider bulges at the cross-sections. In the delivery of PEG-*bis*Tz in the experiments shown in Figure 5.7A, the PEG-*bis*Tz solution interacted mainly with the C12-*bis*TCO functionalities due to our treatments, though the density or coverage of C12-*bis*TCO

functionality is higher at the cross sections. As such, the widening effect is less than that in Figure 5.6B.

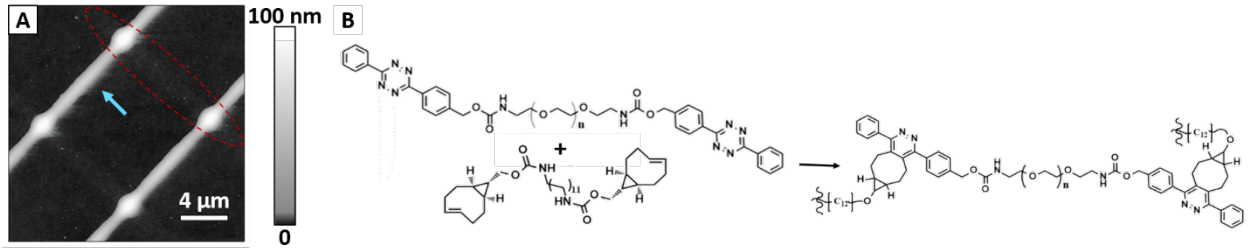

Figure 5.7. (A) 20 x 20 µm AFM topographic image from the printed area following the protocol described above. (B) Ligation between surface bound PEG-*bis*Tz and C12-*bis*TCO in toluene solution form multiblock copolymers.[15]

5.4 Conclusions

Assembly of molecules into micro- and nano-scale structures by design has largely relied on self-assembly of molecules. This work introduces a new means to address this challenge, i.e., controlled assembly of molecules. The principle of this approach is based on delivery of ultrasmall volumes of solution on surfaces using combined AFM and microfluidic delivery. The solvent evaporates rapidly due to the minute volume, thus forcing the assembly of solute, whose overall size and dimension are dictated by the initial liquid geometry and size. Using pre-patterned surfaces, this work revealed that the initial liquid shape can be further tuned, and as such we can control the final assembly of the solute, such as PEG-*bis*Tz molecules. Varieties of structures of PEG-*bis*Tz were produced from 0D to 3D, whose geometry and size could be controlled. Patterns can also be transferred through chemical reaction with C12-*bis*TCO. This work introduces the concept of controlled assembly of molecules, and as such paves the way to achieving 3D

nanoprinting using materials in general. Work is in progress to produce functional 3D nanostructures by design. Beyond the new scientific concept of controlled assembly, the results shall impact technology development, including nanophotonics, nanoelectronics, nanocomposite materials, and tissue engineering.

5.5 References

1. Xu, S.; Liu, G.-y., Nanometer-Scale Fabrication by Simultaneous Nanoshaving and Molecular Self-Assembly. *Langmuir : the ACS journal of surfaces and colloids* **1997,** *13* (2), 127-129.

2. Liu, G.-Y.; Xu, S.; Qian, Y., Nanofabrication of Self-Assembled Monolayers Using Scanning Probe Lithography. *Accounts Chem Res* **2000,** *33* (7), 457-466.

3. Zhang, J.; Piunova, V. A.; Liu, Y.; Tek, A.; Yang, Q.; Frommer, J.; Liu, G.-y.; Sly, J., Controlled Molecular Assembly via Dynamic Confinement of Solvent. *The journal of physical chemistry letters* **2018,** *9* (21), 6232-6237.

4. Ventrici de Souza, J.; Liu, Y.; Wang, S.; Dörig, P.; Kuhl, T. L.; Frommer, J.; Liu, G.-y., Three-dimensional nanoprinting via direct delivery. *The Journal of Physical Chemistry B* **2017,** *122* (2), 956-962.

5. Mallat, T.; Orglmeister, E.; Baiker, A., Asymmetric catalysis at chiral metal surfaces. *Chemical Reviews* **2007,** *107* (11), 4863-4890.

6. Gellman, A. J., Chiral Surfaces: Accomplishments and Challenges. *Acs Nano* **2010,** *4* (1), 5-10.

7. Mark, A. G.; Forster, M.; Raval, R., Recognition and Ordering at Surfaces: The Importance of Handedness and Footedness. *Chemphyschem* **2011,** *12* (8), 1474-1480.

8. Darling, G. R.; Forster, M.; Lin, C.; Liu, N.; Raval, R.; Hodgson, A., Chiral segregation driven by a dynamical response of the adsorption footprint to the local adsorption environment: bitartrate

on Cu(110). *Phys Chem Chem Phys* **2017,** *19* (11), 7617-7623.

9. Bombis, C.; Weigelt, S.; Knudsen, M. M.; Norgaard, M.; Busse, C.; Laegsgaard, E.; Besenbacher, F.; Gothelf, K. V.; Linderoth, T. R., Steering Organizational and Conformational Surface Chirality by Controlling Molecular Chemical Functionality. *Acs Nano* **2010,** *4* (1), 297-311.

10. Barlow, S. M.; Raval, R., Complex organic molecules at metal surfaces: bonding, organisation and chirality. *Surf Sci Rep* **2003,** *50* (6-8), 201-341.

11. Raval, R., Chiral expression from molecular assemblies at metal surfaces: insights from surface science techniques. *Chem Soc Rev* **2009,** *38* (3), 707-721.

12. Liu, J.; Chen, T.; Deng, X.; Wang, D.; Pei, J.; Wan, L. J., Chiral Hierarchical Molecular Nanostructures on Two-Dimensional Surface by Controllable Trinary Self-Assembly. *Journal of the American Chemical Society* **2011,** *133* (51), 21010-21015.

13. Ecija, D.; Seufert, K.; Heim, D.; Auwarter, W.; Aurisicchio, C.; Fabbro, C.; Bonifazi, D.; Barth, J. V., Hierarchic self-assembly of nanoporous chiral networks with conformationally flexible porphyrins. *ACS Nano* **2010,** *4* (8), 4936-42.

14. Pendery, J.; Ferjani, S.; Rosenblatt, C.; Petschek, R. G., Spatially controllable surface chirality at the nanoscale. *Epl-Europhys Lett* **2011,** *96* (2).

15. Navikas, V.; Gavutis, M.; Rakickas, T.; Valiokas, R., Scanning Probe-Directed Assembly and Rapid Chemical Writing Using Nanoscopic Flow of Phospholipids. *ACS applied materials & interfaces* **2019,** *11* (31), 28449-28460.

16. Sulkanen, A. R.; Sung, J.; Robb, M. J.; Moore, J. S.; Sottos, N. R.; Liu, G.-y., Spatially Selective and Density-Controlled Activation of Interfacial Mechanophores. *Journal of the*

American Chemical Society **2019,** *141* (9), 4080-4085.

17. Xu, S.; Miller, S.; Laibinis, P. E.; Liu, G. Y., Fabrication of nanometer scale patterns within self-assembled monolayers by nanografting. *Langmuir : the ACS journal of surfaces and colloids* **1999,** *15* (21), 7244-7251.

18. Ulman, A., Formation and structure of self-assembled monolayers. *Chemical Reviews* **1996,** *96* (4), 1533-1554.

19. Xu, S.; Cruchon-Dupeyrat, S. J. N.; Garno, J. C.; Liu, G. Y.; Jennings, G. K.; Yong, T. H.; Laibinis, P. E., In situ studies of thiol self-assembly on gold from solution using atomic force microscopy. *Journal of Chemical Physics* **1998,** *108* (12), 5002-5012.

20. Strong, L.; Whitesides, G. M., Structures of Self-Assembled Monolayer Films of Organosulfur Compounds Adsorbed on Gold Single-Crystals - Electron-Diffraction Studies. *Langmuir : the ACS journal of surfaces and colloids* **1988,** *4* (3), 546-558.

21. Dubois, L. H.; Nuzzo, R. G., Synthesis, Structure, and Properties of Model Organic-Surfaces. *Annual Review of Physical Chemistry* **1992,** *43*, 437-463.

22. Liu, M.; Amro, N. A.; Liu, G.-y., Nanografting for Surface Physical Chemistry. *Annual Review of Physical Chemistry* **2008,** *59* (1), 367-386.

23. Love, J. C.; Estroff, L. A.; Kriebel, J. K.; Nuzzo, R. G.; Whitesides, G. M., Self-assembled monolayers of thiolates on metals as a form of nanotechnology. *Chemical Reviews* **2005,** *105* (4), 1103-1169.

24. Xia, Y. N.; Rogers, J. A.; Paul, K. E.; Whitesides, G. M., Unconventional methods for fabricating and patterning nanostructures. *Chemical Reviews* **1999,** *99* (7), 1823-1848.

25. Gates, B. D.; Xu, Q. B.; Stewart, M.; Ryan, D.; Willson, C. G.; Whitesides, G. M., New

approaches to nanofabrication: Molding, printing, and other techniques. *Chemical Reviews* **2005,** *105* (4), 1171-1196.

26. Wen, K.; Maoz, R.; Cohen, H.; Sagiv, J.; Gibaud, A.; Desert, A.; Ocko, B. M., Postassembly chemical modification of a highly ordered organosilane multilayer: New insights into the structure, bonding, and dynamics of self-assembling silane monolayers. *Acs Nano* **2008,** *2* (3), 579-599.

27. Rosa, L. G.; Liang, J., Atomic force microscope nanolithography: dip-pen, nanoshaving, nanografting, tapping mode, electrochemical and thermal nanolithography. *J Phys-Condens Mat* **2009,** *21* (48).

28. Bu, D. L.; Mullen, T. J.; Liu, G. Y., Regulation of Local Structure and Composition of Binary Disulfide and Thiol Self-Assembled Monolayers Using Nanografting. *Acs Nano* **2010,** *4* (11), 6863-6873.

29. Jung, H.; Kulkarni, R.; Collier, C. P., Dip-pen nanolithography of reactive alkoxysilanes on glass. *Journal of the American Chemical Society* **2003,** *125* (40), 12096-12097.

30. Li, J.; Nagamani, C.; Moore, J. S., Polymer Mechanochemistry: From Destructive to Productive. *Accounts Chem Res* **2015,** *48* (8), 2181-2190.

31. Li, J.; Shiraki, T.; Hu, B.; Wright, R. A. E.; Zhao, B.; Moore, J. S., Mechanophore Activation at Heterointerfaces. *Journal of the American Chemical Society* **2014,** *136* (45), 15925-15928.

32. Chen, T.; Yang, W. H.; Wang, D.; Wan, L. J., Globally homochiral assembly of two-dimensional molecular networks triggered by co-absorbers. *Nat Commun* **2013,** *4*, 1389.

33. De Cat, I.; Guo, Z.; George, S. J.; Meijer, E. W.; Schenning, A. P.; De Feyter, S., Induction of chirality in an achiral monolayer at the liquid/solid interface by a supramolecular chiral auxiliary. *J Am Chem Soc* **2012,** *134* (6), 3171-7.

34. Stepanow, S.; Lin, N.; Vidal, F.; Landa, A.; Ruben, M.; Barth, J. V.; Kern, K., Programming supramolecular assembly and chirality in two-dimensional dicarboxylate networks on a Cu(100) surface. *Nano Lett* **2005,** *5* (5), 901-4.

35. Chen, T.; Wang, D.; Wan, L.-J., Two-dimensional chiral molecular assembly on solid surfaces: Formation and regulation. *National Science Review* **2015,** *2*.

36. Vidal, F.; Delvigne, E.; Stepanow, S.; Lin, N.; Barth, J. V.; Kern, K., Chiral phase transition in two-dimensional supramolecular assemblies of prochiral molecules. *J Am Chem Soc* **2005,** *127* (28), 10101-6.

37. Ernst, K.-H., Molecular chirality at surfaces. *physica status solidi (b)* **2012,** *249* (11), 2057-2088.

38. Raval, R., Chiral expressions at metal surfaces. *Current Opinion in Solid State and Materials Science* **2003,** *7* (1), 67-74.

39. Vettiger, P.; Despont, M.; Drechsler, U.; Durig, U.; Haberle, W.; Lutwyche, M. I.; Rothuizen, H. E.; Stutz, R.; Widmer, R.; Binnig, G. K., The "Millipede"—More than thousand tips for future AFM storage. *IBM Journal of Research and Development* **2000,** *44* (3), 323-340.

40. Schriber, E. A.; Popple, D. C.; Yeung, M.; Brady, M. A.; Corlett, S. A.; Hohman, J. N., Mithrene Is a Self-Assembling Robustly Blue Luminescent Metal–Organic Chalcogenolate Assembly for 2D Optoelectronic Applications. *ACS Applied Nano Materials* **2018,** *1* (7), 3498-3508.

41. Trang, B.; Yeung, M.; Popple, D. C.; Schriber, E. A.; Brady, M. A.; Kuykendall, T. R.; Hohman, J. N., Tarnishing Silver Metal into Mithrene. *Journal of the American Chemical Society* **2018,** *140* (42), 13892-13903.

42. Liu, N.; Sun, G.; Zhu, J., Photo-induced self-cleaning functions on 2-anthraquinone carboxylic

acid treated cotton fabrics. *Journal of Materials Chemistry* **2011,** *21* (39), 15383-15390.

43. Zhuo, J., Photoactive chemicals for antimicrobial textiles. In *Antimicrobial Textiles*, Sun, G., Ed. Woodhead Publishing: 2016; pp 197-223.

44. Gao, A.; Zhang, H.; Sun, G.; Xie, K.; Hou, A., Light-induced antibacterial and UV-protective properties of polyamide 56 biomaterial modified with anthraquinone and benzophenone derivatives. *Materials & Design* **2017,** *130*.

45. Zhuo, J.; Sun, G., Antimicrobial functions on cellulose materials introduced by anthraquinone vat dyes. *ACS applied materials & interfaces* **2013,** *5* (21), 10830-5.

CHAPTER 6

Conclusions, on-Going Work and Future Perspectives

6.1 Conclusions

The activation of a surface bound mechanophore can be achieved via scanning probe microscopy.

We demonstrated the activation of a surface immobilized maleimide−anthracene mechanophore with a PGMA brush using AFM. Taking advantage of the accurate force control in AFM, the contact force between the probe apex and the substrate-bound mechanophore was tuned for either imaging or activation. The retro-[4 + 2] cycloaddition upon activation of the MA mechanophore was verified by the topographic changes revealed by in situ AFM imaging and fluorescence microscopy, where surface-bound anthracene exhibits a characteristic emission at 410−430 nm. This new means to activate mechanophores has the intrinsic advantages of (a) a wide range of force control and tunability; (b) high spatial precision, which enables nanolithography (we focused on utilizing AFM nanolithography); and (c) in situ activation and characterization. The high spatial resolution of AFM enabled nanolithography of complex structures with high spatial accuracy and selectivity. Unlike prior 2D nanolithography where the contrast is mostly binary, we demonstrate that multilevel contrast in the original design, including gradient features and hierarchical micro and nanostructures, could be faithfully translated via spatially controlled surface chemistry. Work is in progress to construct 3D nanostructures by combing this approach with subsequent surface reactions, which will enable 3D nanoprinting. Future applications include production of coatings and composite materials that require nanopatterning or texture control as well as nanodevices and sensors for measuring mechanical stress and damages in situ.

Organizational chiral features were fabricated by design using AFM-based nanolithography.

Using atomic force microscopy in conjunction with one's chosen surface reactions, our methodology enables production of various chiral structures by design with nanometer precision, from simple chiral spirals to arrays of chiral nanofeatures to hierarchical chiral structures. The size, geometry, and organizational chirality followed the designs with a high degree of spatial fidelity. The concept and methodology enabled researchers to carry out organizational chiral chemistry, with the intrinsic advantages of chiral structures by design. The individual chiral structures, their locations on surfaces, and total coverage by these organizational chiral structures can all be controlled. Being able to selectively produce a single chiral form offers the possibility to create enantioselectivity on the surface, which is critical for future enantioselective applications of these structures. By employing parallel processing techniques, the throughput of organizational chirality by design can be greatly increased, making large scale array feasible in a reasonable amount of time. The results open new and promising applications including organizational chiral sensors, 3D nanoprinting of chiral structures, enantiomeric separation, and enantiomeric heterogeneous catalysis.

We Created Features by Design Using Controlled Assembly of Small Molecules.

Assembly of molecules into micro- and nanoscale structures by design has largely relied on SA of molecules. This work introduces controlled assembly of molecules as a new means to address this challenge. The principle of this approach is based on delivery of ultrasmall volumes of solution on surfaces using combined AFM and microfluidic delivery. The solvent evaporates rapidly due to the minute volume, thus forcing the assembly of solute, whose overall size and dimension are dictated by the initial liquid geometry and size. Using prepatterned surfaces, this work revealed

that the initial liquid shape can be further tuned, and as such, we can control the final assembly of the solute, such as PEG-bisTz molecules. Varieties of structures of PEG-bisTz were produced from 0D to 3D, whose geometry and size could be controlled. Patterns can also be transferred through chemical reaction with C12-bisTCO. This work introduces the concept of controlled assembly of small molecules and paves the way to achieving 3D nanoprinting using materials in general. Work is in progress to produce functional 3D nanostructures by design. Beyond the new scientific concept of controlled assembly, the results shall impact technology development, including nanophotonics, nanoelectronics, nanocomposite materials, and tissue engineering.

6.2 On-Going Work and Future Perspectives

6.2.1 Atomic Force Microscopy and Tip Enhanced Raman Spectroscopy Investigation of Mithrene

To extended our concept of 3D printing to broader materials, we tested a organometallic material referred to as mithrene that is known to be responsive to mechanical force.[40] Hybrid materials, specifically crystalline metal-organic chalcogenolate assemblies (MOCHAs) have had an increase in recent years due to their unique properties.[1-5] One such material is mithrene, which was developed by Hohman et al.[6-8] Mithrene is composed of discreate layers of silver benzeneselenolate, $[AgSeC6H5]_{\infty}$, with the phenyl groups acting as electronically isolating layers that 'sandwich' a conductive silver selenolate layer within. Mithrene forms as a square, "stepped" crystalline structure, the layers running parallel to the (001) plane, with only weak intermolecular forces holding the layers together, similar to other '2D materials such as graphene and MoS_2. Prior characterization of this material showed that mithrene crystals have edge lengths 1-4 μm, and interlamellar spacing of 1.4 nm. Spectroscopic characterization revealed that mithrene exhibits a robust blue luminescence at 467 nm upon excitation with a 405 nm laser, irrespective of the crystal size

or morphology.[6] Though some of the properties of mithrene have already been uncovered, further study of the material is required, including high resolution imaging of its (001) plane, as well as mechanostability tests and localized spectroscopic investigations.

6.2.2 High Resolution Imaging of Mithrene.

High-resolution atomic force microscopy (AFM) of mithrene revealed the long-range order of the mithrene (001) surface. Based on the lateral force image shown in Figure 6.1 (collected with Dr. Shuo Wang's assistance), the unit cell constants were determined to be a=4.0 ± 0.8 Å, b=4.0 ± 1.1 Å and θ=67 ± 3°. From the X-ray diffraction data, the expected lattice constants and angle were a=b=3.758Å and θ=77.13°. arrangement of the phenyl groups within the (001) plane, which had previously only been hypothesized from crystallographic calculations. Analysis of the image revealed that the unit cell constants were a= 4.0 ± 0.8 Å, b= 3.0 ± 0.8 Å and θ=66.6 ± 2.6°, which is similar to the expected (001) surface of mithrene. Given how well the measured constants match the expected values, we can conclude that the surface imaged is an unreconstructed (001) surface. This is the first time packing the (001) surface has been quantitatively measured, and it gives valuable insight into the behavior of the material surface under ambient conditions, which is critical for potential applications of this novel material.

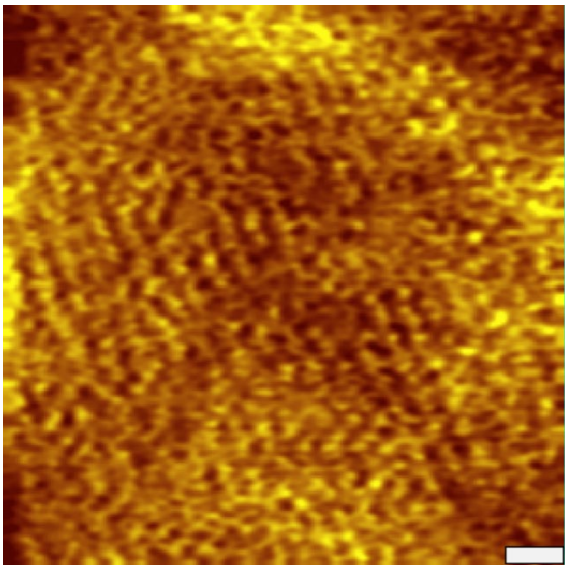

Figure 6.1. High resolution lateral AFM image of mithrene's (001) plane. The lateral scale bar of the AFM image is 1.0 nm.

6.2.3 High Force Shearing of Mithrene via AFM.

Force-dependent imaging of mithrene microcrystals in isopropyl alcohol revealed its mechanostability. Low force (17 nN) imaging of the individual crystals reveal the stepped cubic geometry in Figure 6.2A, similar to prior SEM investigations.[40-41] In contrast to SEM, the 3D information in the individual crystal flakes can be measured using AFM, revealing the crystal's height of 77.1 nm. Based on the expected step height of 1.4 nm, this crystal is composed of 55 layers. The friction coefficient between a silicon tip & mithrene is estimated to be 0.3 from the literature value of a similar system, molybdenum-disulfide.[11] This friction coefficient is used to estimate the shear force applied from the normal force applied, which are listed in Table 6.1. At shear forces of 5-51 nN (Figure 6.2B), the layered structure remained intact. Increasing the shear force to 153 nN (Figure 6.2C), layers of the crystal started to exfoliate. This behavior is analogous

to the layer-by-layer peeling of other 2D materials such as MoS_2 and graphite, whose layers are held together by van der Waals interactions, while the atoms within each layer are held together by covalent bonding. Further increasing of shear force to 255 nN (Figure 6.2D), a larger number of layers (40 out 55) were exfoliated. Based on previously published work, mithrene is stable up to 5 days at elevated temperatures (≤90°C), or up to 1 hour for temperatures as high as 180°C. Based on the high force AFM scans, mithrene is mechanically stable to at least 51 nN shear force, maintaining its multilayered structure due to van der Waals interactions between the phenyl layers. At shear forces of 153 nN and above, the van der Waals interactions between the phenyl layers is overcome, resulting in the exfoliation of the over half of the layers (40 out of 55) subjected to the high force scan.

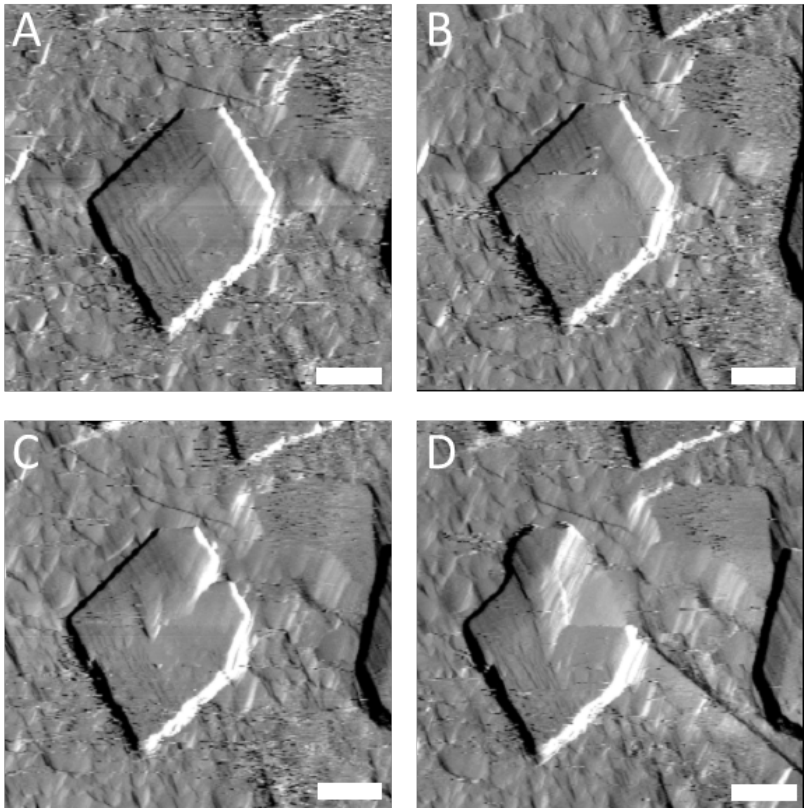

Figure 6.2. Deflection AFM images of mithrene crystals in isopropyl alcohol. (A) Low force (5.1

nN shearing) of a mithrene crystal before any high force scans. (B) After 51 nN shear force. (C) After 153 nN shear force. (D) After 255 nN shear force. Lateral scale bars are 500 nm.

Table 6.1. Normal and shear forces for the AFM deflection images in Figure 6.2.

Figure Index	A	B	C	D
Normal Force (nN)	17	170	510	850
Shear Force (nN)	5.1	51	153	255

6.2.4 TERS and Far Field Raman Spectroscopy of Mithrene.

Tip Enhanced Raman spectroscopy enables collection of spectroscopic information with nanoscale resolution. TERS is done by integrating a scanning probe microscope, an AFM in our case, with a confocal Raman spectrometer. Upon illumination with a laser, localized surface plasmons are excited near the apex of the tip, which leads to a substantial enhancement of the electromagnetic field, which in turn increases the Raman scattering of materials in the vicinity of the tip.[12] TERS generally provides an enhancement of 10^3-10^6, with a spatial resolution of 10-80 nm, enabling the collection of localized spectroscopic data, rather than average data of the bulk material. By combining point-by-point scanning of the AFM tip with simultaneous spectrum acquisition, near-field Raman mappings can be performed with lateral resolution down to ten nanometers or less.[9] Applying this technique to mithrene, we can get spectroscopic information for individual crystals, as well as nm sized regions within the crystals themselves. Additionally, the resulting TERS spectra can be used to evaluate the crystallinity of the sample. From TERS, several prominent peaks can be seen, as listed in Table 6.2. The normal mode assignments are

based on previously published assignments for a similar compound, diphenyl diselenide.[13] In comparison to the far field Raman spectroscopy under the same setting, we identified 9 new peaks on the TERS spectra (collected by Dr. Andrey Krayev), which are written in green in both Figure 6.3 as well as Table 6.2. The first new peak appeared at 465.533 cm^{-1}, which we assigned to out of plane bending, γ (CCC). Several new peaks were also discernable on at 622.760 cm^{-1}, 668.712 cm^{-1} and 695.137 cm^{-1}, which are assigned to β (CCC), β (CCC)/ν (CSe) and γ (CCC) respectively. The β vibrational modes are in-plane bending modes of the C-C-C bonds within the phenyl rings, while the stretching mode, ν, seen at 668. 712 cm^{-1} is the C-Se of the selenium bound phenyl rings. Another new peak (γ(CH)) is seen on TERS at 904.968 cm^{-1}, which is the out-of-plane bending of the C-H bonds of the phenyl rings. Two additional new peaks for β (CH) can be seen on TERS at 1161.070 cm^{-1} and 1161.070 cm^{-1}. And two final new peaks for ν (CC) were also seen on the TERS spectra at 1439.850 cm^{-1} and 1477.650 cm^{-1}. The relative intensities of 1026.500 cm^{-1} to 1003.750 cm^{-1} and 1067.200 cm^{-1} to 1003.750 $cm^{-1}$are comparable between far field and TERS, with both ratios being approximately ~0.89 for TERS and ~0.98 for far field. These peaks primarily correspond to bending modes of (CCC) or (CH), though the peak at 1067.222 cm^{-1} is also attributed to out of plane bending of C-Se (ν (CSe)).

Comparing the TERS spectra to the bulk far field Raman, there are several differences as well. The assignments for each of the peaks are labelled on their respective spectra. There is an enhancement in the CH signal, specifically a new peak for γ (CH) appeared at 904.968 cm^{-1} on the TERS spectra that does not appear on the far field bulk Raman. In the 1100-1200 cm^{-1} region, we see two small β (CH) peaks while far field sees a single β(CCC) peak. Additionally, the splitting seen at the 1577.090 cm^{-1} (ν (CC)) peak on bulk Raman spectra shows as a single peak on the

TERS spectra. The relative intensity of 1026.5 cm^{-1} to 1003.75 cm^{-1} (β (CCC)) increased from 0.49 (bulk far field) to 0.89 (TERS), as well as the relative intensity of 1067.200 cm^{-1} to 1003.75 cm^{-1} (β (CCC)) increased from 0.49 (bulk far field) to 0.89 (TERS).

The narrowness and lack of peak splitting in the spectra demonstrate the single crystallinity of the area measured and validates the quality of the sample prep. TERS enhancement is observed with a sample volume as small as 5-10 nm illumination is very strong, all major normal modes are observed, include CH bonds that are not observed in the far field Raman.

The relative intensity enhancement that we see can be attributed to our near field enhancement. Structurally, this is like because the Cse orientation is near to surface normal, so has stronger enhancement with TERS. Additionally, the sample is very stable under laser illumination, demonstrating its photostability.

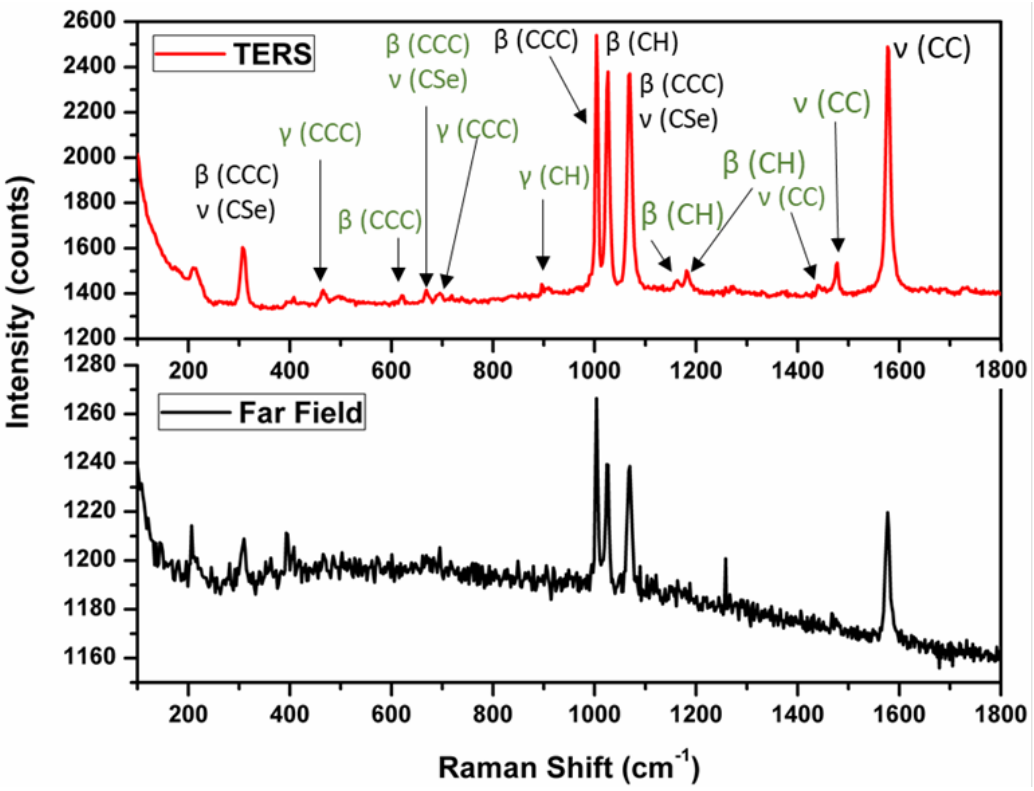

Figure 6.3. TERS and far field Raman spectra of gold coated mithrene crystals. The peak assignments for all major peaks are labelled, with the green text representing new peaks on the TERS spectra compared to far field.

Table 6.2. Raman peak assignments for TERS of mithrene.

Table 6.2	
Raman Shift (cm^{-1})	Normal Mode Assignment
306.876	β (CCC); ν (CSe)
465.533	γ (CCC)
622.760	β (CCC)
668.712	β (CCC); ν (CSe)
695.137	γ (CCC)
904.968	γ (CH)
1003.750	β (CCC)
1026.500	β (CH)
1067.200	β (CCC) ν (CSe)
1161.070	β (CH)
1180.990	β (CH)
1439.850	ν (CC)
1477.650	ν (CC)
1577.090	ν (CC)

6.2.5 Conclusions & Future Work

Mithrene is a new 2D material with promising applications. This work revealed more physiochemical properties of this material, which shall provide important guide to develop future

research and application efforts. Future work for this project includes doing force dependent Raman measurements of mithrene, to see if the spectra changes with force applied, and STM imaging of the (001) plane of mithrene using a conductive monolayer coating, either graphene or boron nitride, to provide even higher resolution imaging of the (001) plane.

6.2.6 Functionalization of Cellulose Nanocrystals with Anthraquinone

To extend our concept of 3D printing to broader materials, we tested an important green material, referred to as cellulose, whose nanocrystalline form was functionalized to imbue it with anti-microbial properties.[42-45] There has been a growing interest in antimicrobial materials recently due to an increasing rate of pathogenic microbial contamination. One means of addressing this growing issue is through self-cleaning surfaces, which could significantly reduce the possibility of contamination, especially in environments where high sterility is crucial, such as hospitals. Along this vein, materials functionalized with light reactive groups could help to combat microbial contamination. One promising candidate to functionalize materials with is anthraquinone (AQ), which produces reactive oxygen species (ROS) such as peroxides when exposed to UV light. [14, 15] Covalent linkage of this compound to fabrics allowed anthraquinone to retain its light reactive properties while immobilizing it on the surface, preventing it from leaching away.[16] Taking this modification one step further, anthraquinone was incorporated onto the surfaces of cellulose nanocrystals (CNCs). Cellulose nanocrystals can be derived from renewable and sustainable materials such as cotton, making them an appealing substrate for functionalization with anthraquinone.[17] When CNCs are initially produced through acid hydrolysis of cotton fibers in sulfuric acid, their surfaces contain a multitude of covalently bound sulfate ester groups. The presence of these groups makes the addition of the anthraquinone moiety more challenging, so

their removal is necessary for efficient functionalization of the CNCs with anthraquinone. No previous work on the functionalization of CNCs has been previously published, so we utilized a variety of techniques, including AFM to characterize the newly functionalized CNC and compare it to both the sulfated and desulfated forms of the CNCs.

6.2.7 AFM Characterization of Sulfated, Desulfated and AQ Functionalized CNCs

The individual cellulose nanocrystals were visualized via AFM imaging, as seen in Figure 6.4A-C Examples of the individual CNCs are indicated in the images by oval enclosures. The AFM topographic images reveal that the individual crystals of each functionalization exhibit a rod-like geometry. The diameter and length of each rod highlighted in Figure 6.4A-C are measured from the topographic images and summarized in Table 6.3 below. The diameters of CNCs, DS-CNCs and AQ-CNCs fall within the range of 2.5-3.5 nm. Since individual CNCs maintain very similar diameters upon treatments of desulfation followed by anthraquinone functionalization, we anticipate little complication in subsequent applications.

The AFM topographic images also reveal the presence of bundles of rods for each sample. Examples of these bundles are indicated by rectangular enclosures. In the two CNC bundles shown in Figure 6.4A, one is a cross of 131.5 and 110.5 nm rods, and the other is a short rod (77.4 nm) completely atop of a rod (173.8 nm), resulting in the bright contrast seen in the AFM topograph. In the two DS-CNC bundles shown in Figure 6.4B, the topmost bundle is composed of three rods: the bottom long rod (225.7 nm) supporting two short rods (51.7 and 70.5 nm, respectively),

completely atop, appearing as two brighter contrasts. The top left bundle is composed of three rods: two rods (219.1 and 169.1 nm) overlapped side-by-side, with the 3rd rod (167.6 nm) stacking perpendicularly atop, leading to a cross shape. In the two AQ-CNC bundles, the bundle in the upper right of Figure 6.4C consists of a 68.1 nm rod stacked atop of a 117.4 nm rod completely. The bundle in the lower left of Figure 6.4C consists of three rods: a 91.9 nm long rod attached to the surface, with a small 56.7 nm rod aligned next to the right end, and the third 134.5 nm rod stacked at an angle on top of the end of the rod beneath it. In contrast to the CNCs and DS-CNCs which exhibit branched bundles, the bundles in the AQ-CNC samples mostly consist of aligned rods, which may be advantageous for subsequent fiber production

For all three types of CNCs, large aggregates were occasionally seen. In Figure 6.4D, the AFM amplitude image clearly reveals the individual CNC rods within the "flake-shaped" aggregate (maximum lateral dimension of 6.6 μm wide), which are aligned in parallel with respect to each other. Simultaneously, the topographic image (not shown) reveals the height of the aggregate as 226.7 nm, which is equivalent to 86 layers of individual crystals. In Figure 6.4E, the AFM amplitude image shows the individual rods within the "haystack" aggregate of the DS-CNCs (with a maximum lateral dimension of 3.1 μm), adopting random orientations. The AFM topographic image (not shown) reveals the height of the aggregate is 67.8 nm, which is equivalent to 21 layers of individual crystals. In Figure 6.4F, the AFM amplitude image reveals the "interwoven" arrangement of the individual AQ-CNC rods within the "tadpole-shaped" aggregate (maximum lateral dimension of 2.8 μm). The AFM topographic image (not shown) shows the aggregate's height as 206.7 nm, which is equivalent to 75 layers of individual crystals. Even though the aggregates are a minority population, from this AFM investigation we recommend caution to

prevent them when processing AQ-CNCs, as the AQ-CNC aggregates would be more difficult to disperse due to the interwoven packing.

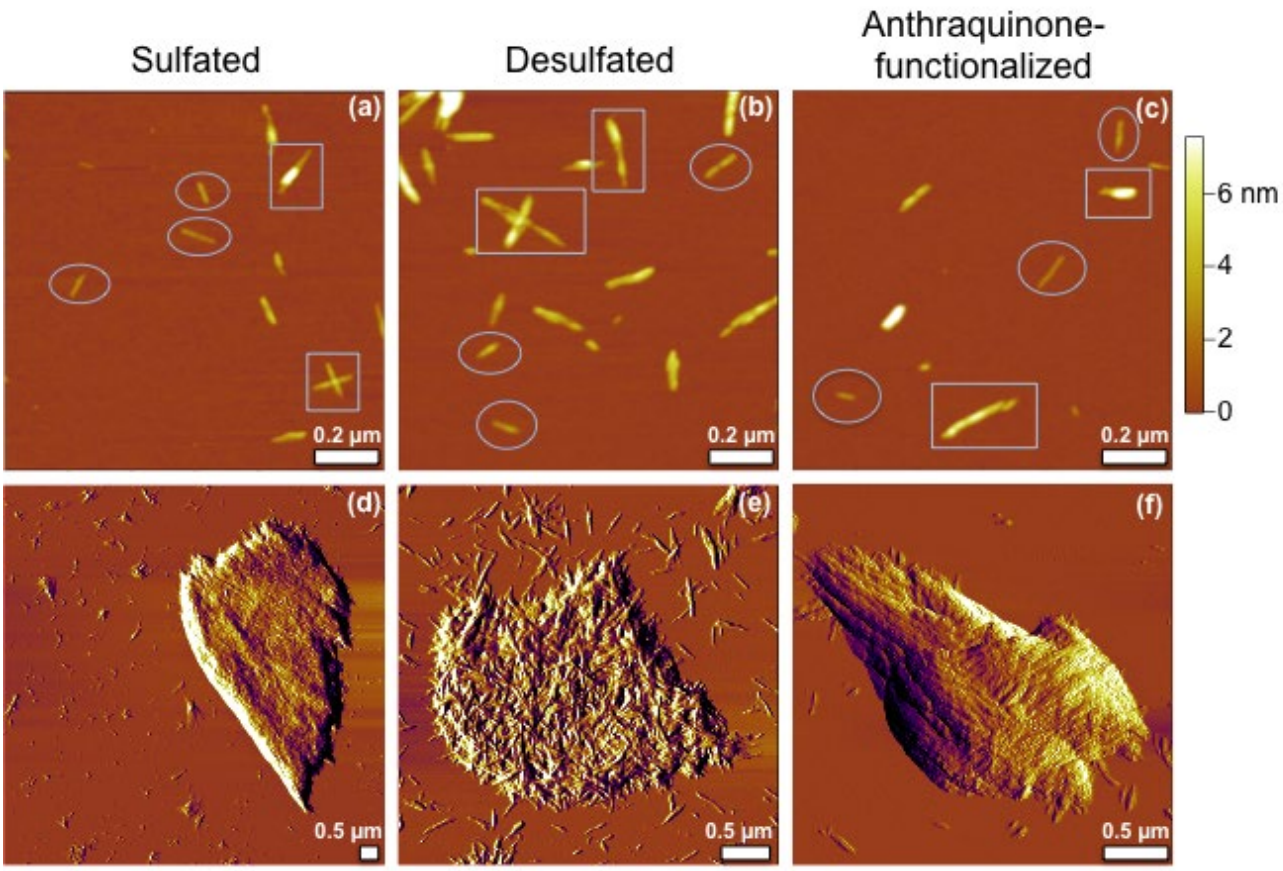

Figure 6.4. AFM topographic images (1.2 µm x 1.2 µm) of (A) CNCs, (B) DS-CNCs, and (C) AQ-CNCs. All images were acquired using tapping mode in ambient. Scale bars = 0.2 µm. AFM amplitude images of aggregates are shown for (D) CNCs, (E) DS-CNCs and (F) AQ-CNCs samples

Table 6.3. Dimensions of individual CNCs measured from Figure 6.4 images A-C.

Samples	Diameter (nm) / Length (nm)		
CNC	2.8/ 115.6	2.5/ 80.6	2.6/ 72.9

DS-CNC	3.0/ 89.7	3.5/ 73.4	3.1/ 118.6
AQ-CNC	3.0/ 99.1	2.8/ 61.6	2.5/ 132.1

6.2.8 Conclusions & Future Work for AQ-CNCs

Functionalization of CNCs with anthraquinone was successfully achieved, creating a promised nanomaterial with antimicrobial applications. This work revealed the morphological changes brought on by the incorporation of the anthraquinone moiety. Despite these changes, AFM revealed that the CNCs retain their structural integrity, an advantage for subsequent production of composite materials. Future work for this project includes the utilization of these AQ-CNCs as "nanoscale build blocks" for the production of 3D printed functionalized nanostructures on surfaces. The antimicrobial and self-cleaning properties of such structures could prove invaluable in combating contamination issues faced when producing 3D nanoscale structures.

6.2.9 References

1. Yan, H.; Hohman, J. N.; Li, F. H.; Jia, C.; Solis-Ibarra, D.; Wu, B.; Dahl, J. E. P.; Carlson, R. M. K.; Tkachenko, B. A.; Fokin, A. A.; Schreiner, P. R.; Vailionis, A.; Kim, T. R.; Devereaux, T. P.; Shen, Z.-X.; Melosh, N. A., Hybrid metal–organic chalcogenide nanowires with electrically conductive inorganic core through diamondoid-directed assembly. *Nature Materials* **2017,** *16* (3), 349-355.

2. Yan, H.; Yang, F.; Pan, D.; Lin, Y.; Hohman, J. N.; Solis-Ibarra, D.; Li, F. H.; Dahl, J. E. P.; Carlson, R. M. K.; Tkachenko, B. A.; Fokin, A. A.; Schreiner, P. R.; Galli, G.; Mao, W. L.; Shen, Z.-X.; Melosh, N. A., Sterically controlled mechanochemistry under hydrostatic pressure.

Nature **2018,** *554* (7693), 505-510.

3. Lavenn, C.; Guillou, N.; Monge, M.; Podbevšek, D.; Ledoux, G.; Fateeva, A.; Demessence, A., Shedding light on an ultra-bright photoluminescent lamellar gold thiolate coordination polymer [Au(p-SPhCO2Me)]n. *Chemical Communications* **2016,** *52* (58), 9063-9066.

4. Dance, I. G.; Fisher, K. J.; Banda, R. M. H.; Scudder, M. L., Layered structure of crystalline compounds silver thiolates (AgSR). *Inorganic Chemistry* **1991,** *30* (2), 183-187.

5. Cuthbert, H. L.; Wallbank, A. I.; Taylor, N. J.; Corrigan, J. F., Synthesis and Structural Characterization of [Cu20Se4(μ3-SePh)12(PPh3)6] and [Ag(SePh)]∞. *Zeitschrift für anorganische und allgemeine Chemie* **2002,** *628* (11), 2483-2488.

6. Schriber, E. A.; Popple, D. C.; Yeung, M.; Brady, M. A.; Corlett, S. A.; Hohman, J. N., Mithrene Is a Self-Assembling Robustly Blue Luminescent Metal–Organic Chalcogenolate Assembly for 2D Optoelectronic Applications. *ACS Applied Nano Materials* **2018,** *1* (7), 3498-3508.

7. Trang, B.; Yeung, M.; Popple, D. C.; Schriber, E. A.; Brady, M. A.; Kuykendall, T. R.; Hohman, J. N., Tarnishing Silver Metal into Mithrene. *Journal of the American Chemical Society* **2018,** *140* (42), 13892-13903.

8. Popple, D. C.; Schriber, E. A.; Yeung, M.; Hohman, J. N., Competing Roles of Crystallization and Degradation of a Metal–Organic Chalcogenolate Assembly under Biphasic Solvothermal Conditions. *Langmuir : the ACS journal of surfaces and colloids* **2018,** *34* (47), 14265-14273.

9. Krayev, A.; Bailey, C. S.; Jo, K.; Wang, S.; Singh, A.; Darlington, T.; Liu, G.-Y.; Gradecak, S.; Schuck, P. J.; Pop, E.; Jariwala, D., Dry Transfer of van der Waals Crystals to Noble Metal Surfaces To Enable Characterization of Buried Interfaces. *ACS applied materials & interfaces*

2019, *11* (41), 38218-38225.

10. Jariwala, D.; Krayev, A.; Wong, J.; Robinson, A. E.; Sherrott, M. C.; Wang, S.; Liu, G.-Y.; Terrones, M.; Atwater, H. A., Nanoscale doping heterogeneity in few-layer WSe2 exfoliated onto noble metals revealed by correlated SPM and TERS imaging. *2D Materials* **2018,** *5* (3), 035003.

11. Santos, L. V.; Trava-Airoldi, V. J.; Iha, K.; Corat, E. J.; Salvadori, M. C., Diamond-like-carbon and molybdenum disulfide nanotribology studies using atomic force measurements. *Diamond and Related Materials* **2001,** *10* (3), 1049-1052.

12. Shao, F.; Zenobi, R., Tip-enhanced Raman spectroscopy: principles, practice, and applications to nanospectroscopic imaging of 2D materials. *Analytical and Bioanalytical Chemistry* **2019,** *411* (1), 37-61.

13. Han, S.; Kim, K., Self-Assembled Monolayers of Organoselenium Compounds on Gold: Surface-Enhanced Raman Scattering Study. *Journal of colloid and interface science* **2001,** *240*, 492-497.

14. Liu, N.; Sun, G., Production of Reactive Oxygen Species by Photoactive Anthraquinone Compounds and Their Applications in Wastewater Treatment. *Industrial & Engineering Chemistry Research* **2011,** *50* (9), 5326-5333.

15. Zhuo, J.; Sun, G., Antimicrobial functions on cellulose materials introduced by anthraquinone vat dyes. *ACS applied materials & interfaces* **2013,** *5* (21), 10830-5.

16. Liu, N.; Sun, G.; Zhu, J., Photo-induced self-cleaning functions on 2-anthraquinone carboxylic acid treated cotton fabrics. *Journal of Materials Chemistry* **2011,** *21* (39), 15383-15390.

17. Rajinipriya, M.; Nagalakshmaiah, M.; Robert, M.; Elkoun, S., Importance of Agricultural and Industrial Waste in the Field of Nanocellulose and Recent Industrial Developments of Wood Based

Nanocellulose: A Review. *ACS Sustainable Chemistry & Engineering* **2018,** *6* (3), 2807-2828.